

Hypergraph Representations of Single-Cell RNA Sequencing Data for Improved Cell Clustering

Wan He*,¹ Daniel I. Bolnick,² Samuel V. Scarpino,^{3,4,5,1,6,7} and Tina Eliassi-Rad^{1,5,6,7}

¹*Network Science Institute, Northeastern University, Boston, MA, USA*

²*Department of Ecology and Evolutionary Biology,
University of Connecticut Storrs CT, USA*

³*Institute for Experiential AI, Northeastern University, Boston, MA, USA*

⁴*Bouve College of Health Sciences, Northeastern University, Boston, MA, USA*

⁵*Khoury College of Computer Sciences, Northeastern University, Boston, MA, USA*

⁶*Vermont Complex Systems Institute, University of Vermont, Burlington, VT, USA*

⁷*Santa Fe Institute, Santa Fe, NM, USA*

Abstract

Motivation: Single-cell RNA sequencing (scRNA-seq) data analysis is often performed using network projections that produce co-expression networks. These network-based algorithms are attractive because regulatory interactions are fundamentally network-based and there are many tools available for downstream analysis. However, most network-based approaches have two major limitations. First, they are typically unipartite and therefore fail to capture higher-order information. Second, scRNA-seq data are often sparse, so most algorithms for constructing unipartite network projections are inefficient and may overestimate co-expression relationships, or may under-utilize the sparsity when clustering (e.g., with cosine distance). To address these limitations, we propose representing scRNA-seq expression data as hypergraphs, which are generalized graphs where a hyperedge can connect more than two nodes. In this context, hypergraph nodes represent cells, and hyperedges represent genes. Each hyperedge connects all cells in which its corresponding gene is actively expressed, indicating the expression of that gene across different cells. The resulting hypergraph can capture higher-order information and appropriately handle varying levels of data sparsity. This representation enables clustering algorithms to leverage higher-order relationships for improved cell-type differentiation.

Results: To distinguish cell types using hypergraph representations of scRNA-seq data,

we introduce two novel clustering algorithms: (1) Dual-Importance Preference Hypergraph Walk (DIPH) and (2) Co-expression and Memory-Integrated Dual-Importance Preference Hypergraph Walk (CoMem-DIPH). DIPH is a new hypergraph-based random walk algorithm that computes cell embeddings by considering the relative importance of genes to cells and cells to genes, incorporating a preference exponent to facilitate clustering. CoMem-DIPH integrates two unipartite projections, the gene co-expression and cell co-expression networks, along with the cell-gene expression hypergraph derived from single-cell abundance count data into the random walk model. The advantage of CoMem-DIPH is that it accounts for both local information from single-cell gene expression and global information from pairwise similarity in the two co-expression networks. We benchmark the performance of our algorithms against established and state-of-the-art deep learning approaches using both real-world and simulated scRNA-seq data. Real-world datasets include cells from the human pancreas, mouse pancreas, human brain, and mouse brain tissues. We also use a ground-truth labeled cell-type annotation dataset based on human lung adenocarcinoma cell lines. Quantitative evaluation shows that CoMem-DIPH consistently outperforms established algorithms and state-of-the-art deep learning algorithms for cell-type clustering. Our proposed algorithms show the greatest improvement on scRNA-seq data with weak modularity. Moreover, CoMem-DIPH successfully annotates clusters with biologically relevant cell types. Our results highlight the utility of hypergraph representations in the analysis of scRNA-seq data.

Availability and Implementation: Our methods are implemented in Python and are available at <https://github.com/wanhe13/CoMem-DIPH>.

I. INTRODUCTION

Network analysis has become a popular tool for studying complex systems in biology, reflecting the combinatorial interactions of biomolecules. Its applications include functional analysis [1–4] and prediction of interactions in protein-protein interaction (PPI) networks [5–7], identification of regulators and analysis of pathways in gene regulatory networks [8–10], disease modeling, prediction, and intervention in epidemiology [11–13], and identification of cell types in co-expression networks [14–17].

However, traditional methods represent biological systems using unipartite networks, which capture relationships only between a single type of entity. Such representations are often not the most natural or information-preserving choice, since many complex systems involve interactions between multiple types of entities. Most often, a unipartite network projection is chosen such that the system could be analyzed with the abundant network analysis methods developed based on unipartite networks [14, 18]. However, this focus on unipartite networks restricts our attention to biological interactions just between pairs of genes, proteins, or other kinds of nodes.¹ In reality, biological processes often entail multiway interactions that cannot be represented by unipartite networks. For instance, three-gene epistatic interactions vastly outnumber pairwise epistasis in experimental analyses of yeast genetic networks [19]. In protein-protein interaction (PPI) networks, unipartite representations capture relationships between proteins but fail to capture the biological functions associated with groups of proteins. Similarly, unipartite projections of gene regulatory networks connect genes based on regulatory relationships but do not capture relationships among different entities such as transcription factors or their binding sites. Therefore, network analysis methods are needed to more accurately capture the higher-order interactions that are apparently ubiquitous in biological systems.

Single-cell RNA sequencing (scRNA-seq) has enabled the profiling of gene expression at the individual cell level [20–23], whereas conventional bulk tissue RNA sequencing measures expression at the tissue level, averaging gene expression over an ensemble of cells. Cell type identification, as one of the most important downstream tasks in single-cell RNA-seq (scRNA-seq) data analysis [24], has applications in biology and medicine, including tracing the trajectories of different cell lineages in the development of cell differentiation studies [25], tissue heterogeneity analysis for cancer research [26–28], immune cell profiling for therapy development [29–32], and biomarker discovery for diagnosis.

However, cell type identification often relies on conventional transcriptomic data analysis pipelines such as WGCNA [14], Scanpy [17] and Seurat [15, 16]. These packages embed the cell-gene interactions to a unipartite graph structure such as the co-expression network or the K-nearest neighbor (KNN) graph, which draws edges between the cell pairs based on their similarity, followed by unipartite graph partitioning algorithms to detect closely related cell clusters for cell type identification in the scRNA-seq data. These unipartite projections of the scRNA-seq expression data have two limitations: Firstly, cell and gene co-expression networks capture only pairwise

¹ We use the terms node and vertex interchangeably.

expression similarity among cells or genes. As a result, higher-order information, such as the expression level of a specific gene in a specific cell or the coordinated expression of multiple genes within the same cell, is lost. Secondly, scRNA-seq data are sparse, with non-zero entries often accounting for less than 10% of the total [33, 34], compared to 60-90% in bulk-tissue data. Despite this sparsity, constructing a unipartite co-expression network produces in a fully-connected network, which is an inefficient representation of the originally sparse transcriptomic data. Furthermore, the high sparsity of scRNA-seq data (both dropouts and biological zeros) results in inflated correlations, leading to spurious connections and obscure meaningful biological signals, as will be discussed further in III C. In addition, determining whether zero inflation in scRNA-seq data is due to technical dropouts or true biological absence is a challenging task [33, 35, 36].

Given the issues with unipartite projections, it is crucial to explore alternative network representations that can accurately reflect the scRNA-seq data and the underlying biological reality of higher-order interactions among genes. Hypergraphs [37–39] offer a nice solution by directly representing multiway relationships in scRNA-seq data, without requiring further data projection. Existing work on hypergraph representations has demonstrated the improved performance they can achieve in modeling complex biological systems by incorporating higher-order interactions. For example, Liu et al. [40] developed a hypergraph-based neural network to predict synergistic drug combinations for cancer treatment. Wang et al. [41] integrated multi-omics data with hypergraph convolutional neural networks to classify patients with diseases such as breast cancer and Alzheimer’s. Gaudelet et al. [42] used hypergraphs to model interactions across different levels of protein organization (such as protein-protein interactions, complexes, and pathways) to better capture the complexity of biological systems and predict biological functions. Ma and Ma [43] developed a hypergraph-based logistic matrix factorization method that predicts possible metabolite–disease interactions and uncovers novel disease-related metabolites. These successes highlight the potential of hypergraphs to model multiway relationships inherent in biological systems, motivating their application to scRNA-seq analysis.

II. METHODS

We conceptualize scRNA-seq data as a hypergraph \mathcal{H} and design two hypergraph random walk algorithms that capture cell-cell relationships by sampling cell-to-gene and gene-to-cell interactions in the hypergraph. This hypergraph representation of scRNA-seq data does not require addi-

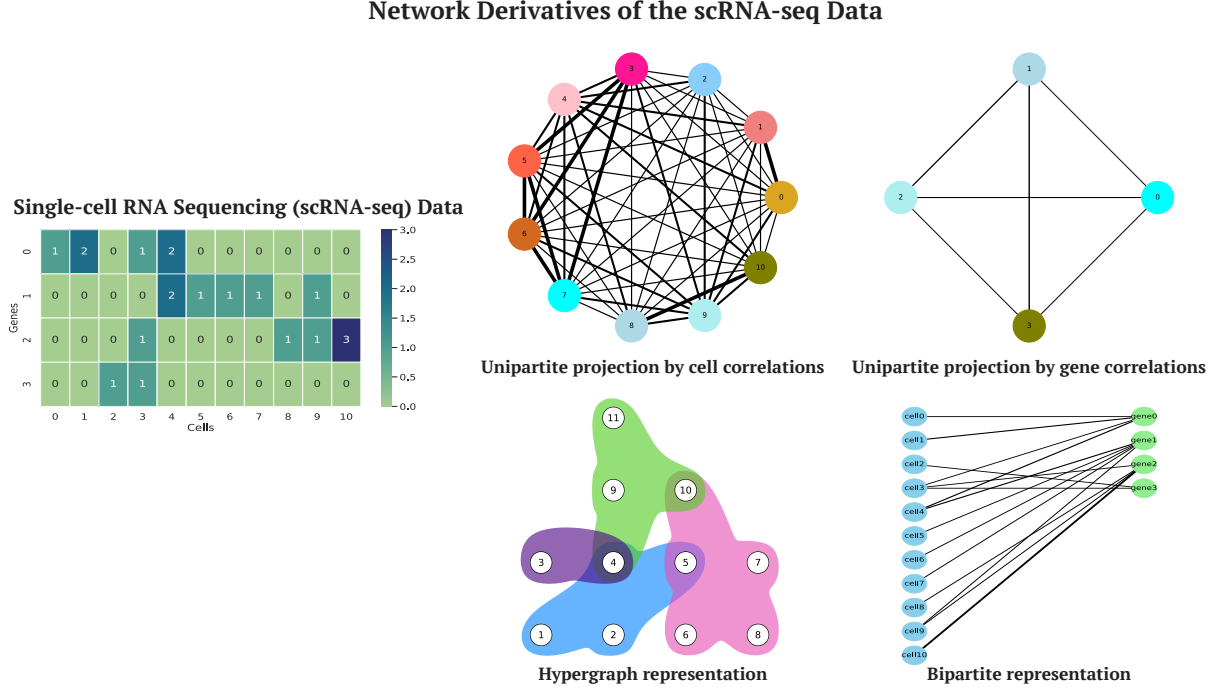


FIG. 1: Network Representations of scRNA-seq Data. Expression data can be represented by various networks, including unipartite network projections such as cell and gene co-expression networks. In a cell co-expression network, nodes are cells and edge weights represent similarity in cell-pair expression. In gene co-expression networks, nodes represent genes. Hypergraph and bipartite network representations preserve the exact expression level of a gene in a cell. In the hypergraph representation, nodes represent cells and hyperedges represent genes. In the bipartite representation, one set of nodes represents cells and the other set represents genes.

tional data transformation, does not cause information loss, or increase computational cost.

A. Hypergraph representation

scRNA-seq data can be conceptualized as a hypergraph $\mathcal{H} = (V, E)$, where:

- V represents the set of nodes corresponding to the cells profiled in the experiment.
- E denotes the set of hyperedges representing genes, with each hyperedge $e \in E$ connecting to all cells $\in V$ in which the gene e is actively expressed. The weight of connection of a hyperedge (gene) to each node (cell) is determined by the gene's expression level in that cell.

Thus, each hyperedge captures the expression profile of a gene across all cells, preventing any loss of information. The incidence matrix $\mathbf{I}_{\mathcal{H}}$ of the hypergraph \mathcal{H} is constructed such that $\mathbf{I}_{\mathcal{H}}(v, e)$ is given by the expression level, i.e. abundance counts, of gene e in cell v .

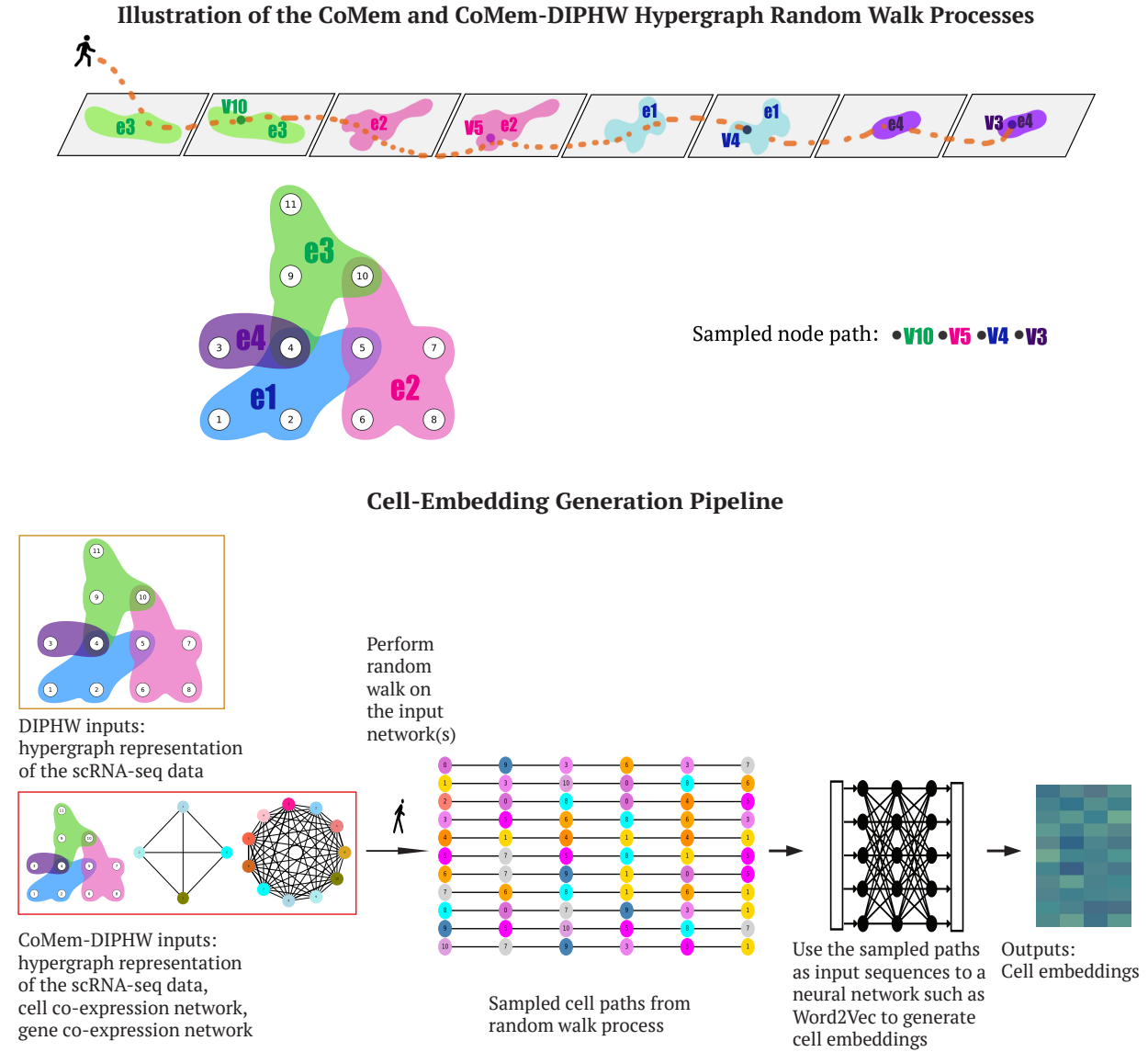


FIG. 2: Hypergraph Clustering Algorithm Illustration. In the hypergraph representation of scRNA-seq data, nodes represent cells and edges represent genes. The expression level of a gene in a cell is captured by the weight of a node in an edge. Random walks are performed on the hypergraph by alternately considering the probability of the walker choosing a node given an edge and choosing an edge given the current node. For DIPHW, the input is the hypergraph representation of the scRNA-seq data. For CoMem-DIPHW, the input includes the hypergraph, cell co-expression network, and gene co-expression network, which serve as node and edge similarity matrices to incorporate memory during the walk. A small neural network (word2vec) is applied to the sampled node paths from the hypergraph random walk process to compute cell embeddings. Finally, cell clustering is performed by applying K-means to the resulting cell embeddings.

B. Method 1: Dual-Importance Preference (DIP) Hypergraph Walk (DIPHW)

Building on this hypergraph representation, we introduce a novel hypergraph random walk approach for cell embedding computation, the *Dual-Importance Preference (DIP) Hypergraph Walk (DIPHW)*, which accounts for both the relative importance of edges to nodes and nodes to edges,

Notation	Description
\mathcal{H}	Hypergraph
$\mathbf{I}_{\mathcal{H}}$	Incidence matrix of the hypergraph \mathcal{H}
V	Set of nodes (cells)
E	Set of hyperedges (genes) in the hypergraph
G_V	Cell co-expression network (node similarity matrix)
G_E	Gene co-expression network (edge similarity matrix)
$\Gamma_e(v)$	Weight of node v in hyperedge e (i.e., expression of gene e in cell v)
$P(V = v E = e)$	Probability of selecting node v given hyperedge e
$P(E = e V = v)$	Probability of selecting hyperedge e given node v
$P(E_{t+1} = e' E_t = e, V_t = v)$	Probability of transitioning to hyperedge e' at time $t + 1$, given current hyperedge e and node v at time t
$P(V_{t+1} = w E_{t+1} = e, V_t = v)$	Probability of selecting node w at time $t + 1$, given hyperedge e at time $t + 1$ and previous node v
$P(V_{t+1} = w V_t = v)$	Unipartite node-to-node transition probability

TABLE I: Notation Table for Our Hypergraph Random Walk Representation.

or the importance of genes relative to cells and cells to genes, along with a preference exponent for faster clustering. In a hypergraph random walk process, the walker alternates between transitioning from a hyperedge to a node and from a node to a hyperedge, following the node-to-edge transition probabilities $P_{E|V}(e, v)$ and edge-to-node transition probabilities $P_{V|E}(v, e)$. In the hypergraph random walk with edge-dependent vertex weight (EDVW) by Chitra and Raphael (2019) [44], the edge-to-node transition probability is edge-dependent, but the node-to-edge transition probability does not consider the importance of the edge to the node. As a natural extension to EDVW, we define the node-to-edge transition probability to be vertex-dependent in DIPHW and use a preference exponent to accelerate the clustering process. The modified random walk process is as follows:

1. Node-to-Hyperedge Transition Probability

The probability of selecting hyperedge e_{t+1} given that the walker is currently at vertex v_t is defined as:

$$P_{E|V}(v_t \rightarrow e_{t+1}) = \frac{\omega(e_{t+1})\gamma_{e_{t+1}}(v_t)}{\sum_{e' \in E(v_t)} \omega(e')\gamma_{e'}(v_t)}$$

In scRNA-seq cell clustering, this represents the probability of selecting a gene based on its expression level relative to other genes in the same cell.

2. Hyperedge-to-Node Transition Probability

Upon the walker's arrival at hyperedge e_{t+1} , the probability of moving to vertex $v_{t+1} \in e_{t+1}$ is given by:

$$P_{V|E}(e_{t+1} \rightarrow v_{t+1}) = \frac{\gamma_{e_{t+1}}^\alpha(v_{t+1})}{\sum_{v' \in e_{t+1}} \gamma_{e_{t+1}}^\alpha(v')}$$

In scRNA-seq cell clustering, the transition from a gene to a cell is based on the relative expression level of a gene in a cell, amplified by a preference exponent to improve clustering convergence.

3. Node-to-Node Transition Probability

The unipartite node-to-node transition probability of DIPHW is calculated by summing the products of the node-to-edge and edge-to-node transition probabilities across all hyperedges. This probability is used to sample random walk node paths, which are then input into a neural network to compute cell embeddings.

$$P(v_t \rightarrow v_{t+1}) = \sum_{e \in E} P_{E|V}(e|v_t) P_{V|E}(v_{t+1}|e).$$

Substituting the expressions for $P_{E|V}(e_{t+1}|v_t)$ and $P_{V|E}(v_{t+1}|e_{t+1})$, we get:

$$P(v_t \rightarrow v_{t+1}) = \sum_{e_{t+1} \in E} \frac{\omega(e_{t+1})\gamma_{e_{t+1}}(v_t)}{\sum_{e' \in E} \omega(e')\gamma_{e'}(v_t)} \frac{\gamma_{e_{t+1}}^\alpha(v_{t+1})}{\sum_{v' \in e_{t+1}} \gamma_{e_{t+1}}^\alpha(v')}$$

The expression of node-to-node transition probability could be simplified by removing reference to any particular time points as,

$$P(u \rightarrow v) = \sum_{e \in E(u)} \frac{\omega(e)\gamma_e(u)}{\sum_{e' \in E} \omega(e')\gamma_{e'}(u)} \frac{\gamma_e^\alpha(v)}{\sum_{u' \in e} \gamma_e^\alpha(u')}$$

4. Node-to-Node Transition Probability in Vectorized Format

The $|V| \times |V|$ node-to-node transition probability matrix $P_{V|V}$ could be written in the matrix form as

$$P = D_{E|V}^{-1} W_{E|V} D_{V|E}^{-1} W_{V|E}$$

The matrix formulation eliminates explicit iteration and reduces computation time. Here, $W_{E|V} = \mathbf{I}_{\mathcal{H}}^T W_E$ is the $|V| \times |E|$ node-to-edge transition weight matrix, where column e of $W_{E|V}$ contains the vertex weights in hyperedge e multiplied by the weight of hyperedge e . Similarly, $W_{V|E}$ represents the edge-to-node transition weight matrix before normalization with dimensions $|E| \times |V|$, given by $W_{V|E} = \mathbf{I}_{\mathcal{H}}^\alpha$, $w_{ve} = [\mathbf{I}_{\mathcal{H}}(e, v)]^\alpha$. Finally, $D_{E|V}$ and $D_{V|E}$ are diagonal matrices that normalize vertex-to-edge and edge-to-vertex transitions to ensure the probability distribution sums to 1.

C. Method 2: co-expression and Memory-Integrated Dual-Importance Preference Hypergraph Walk (CoMem-DIPHW)

CoMem-DIPHW is an extension of DIPHW. It incorporates co-expression networks and single-cell transcriptomic profiles. The memory mechanism of CoMem-DIPHW leverages cell and gene co-expression networks to account for previously visited nodes and edges during transitions to capture both local expression relationships and global co-expression patterns.

1. Hypergraph Representation of the scRNA-seq data

We note that a matrix can be directly interpreted as the incidence matrix of a hypergraph to represent the relationship between two variables, without additional computation.

2. The Node and Edge Similarity Networks: Cell and Gene co-expression Networks and their construction

Using scRNA-seq data, we construct two co-expression networks: the cell co-expression network (G_V) and the gene co-expression network (G_E). In the cell co-expression network, cells are nodes, and edges represent correlation coefficients between cell pairs, indicating the similarity of their expression profiles. Similarly, in the gene co-expression network, genes are nodes, and edges represent correlation coefficients between gene pairs. We use Spearman's rank coefficient to measure pairwise similarity of expression profiles, as it captures non-linearity better

than Pearson's correlation. These unipartite networks serve as node and edge similarity matrices, embedding global-level information that summarizes associations between cell and gene pairs.

3. *Memory-Integrated Random Walk*

CoMem-DIPHW incorporates a memory component by considering the similarity between consecutively visited nodes and edges. This memory mechanism adjusts the transition probabilities so that the node-to-edge transition probability depends on the previously visited edge, and the edge-to-node transition probability depends on the previously visited node. Node-node and edge-edge dependencies are incorporated through the node and edge similarity networks, which are two correlation networks derived from transcriptomic expression data. The memory mechanism constrains the hypergraph walker to focus on cell-gene interactions among similar nodes (cells) and edges (genes), thus better revealing modularity within the data.

While the co-expression networks provide global perspectives through unipartite projections, the specific expression levels of genes in individual cells (local information) are preserved in the hypergraph structure. CoMem-DIPHW integrates global and local information for more accurate cell type identification.

4. *Formulation*

The random walk process in CoMem-DIPHW is formulated as follows. Let G_V be the vertex similarity matrix, where $G_V(v, w)$ quantifies the similarity between nodes v and w . Similarly, let G_E be the edge similarity matrix, where each element $G_E(e, f)$ represents the similarity between edge e and f .

Method 2.0: CoMem

In CoMem, we calculate the unipartite node-to-node transition probability of the hypergraph random walker. To do this, we first calculate the following four probabilities.

1. The probability of selecting vertex v in edge e is:

$$P_{V|E}(e \rightarrow v) = \frac{\Gamma_e(v)}{\sum_{u \in e} \Gamma_e(u)}$$

2. The probability of selecting edge e given vertex v is:

$$P_{E|V}(v \rightarrow e) = \frac{\Gamma_e(v)}{\sum_{e \in E} \Gamma_e(v)}$$

3. The probability of transitioning from node v in edge e_1 to edge e_2 , considering edge similarity, is given by:

$$P_{E_{t+1}|V, E_t}(e_2|v, e_1) = \frac{G_E(e_1, e_2)P(e_2|v)}{\sum_{e' \in E} G_E(e_1, e')P(e'|v)}$$

4. Similarly, the probability of selecting node w from edge e after transitioning from node v , incorporating node similarity and the node-edge connection, is formulated as:

$$P_{V_{t+1}|E, V_t}(w|e, v) = \frac{G_V(v, w)P(w|e)}{\sum_{w' \in e} G_V(v, w')P(w'|e)}$$

Finally, the unipartite node-to-node transition probability of the hypergraph random walk process is:

$$\begin{aligned} & P_{V_t \rightarrow V_{t+1}(v_1, v_2)} \\ & \propto \sum_{e_1, e_2 \in E} P_{V|E}(v_1|e_1)P_{E_2|V, E_1}(e_2|v_1, e_1)P_{V_{t+1}|E, V_t}(v_2|e_2, v_1) \end{aligned}$$

To encourage exploration and ensure non-lazy walks, we modify the node and edge similarity graphs such that the diagonal elements are set to zero. This ensures that during the random walk, the random walker does not remain at the same node or edge in consecutive steps.

Method 2.1: CoMem based on DIPHW

For CoMem-DIPHW, we integrate DIPHW into the CoMem walk framework from section II C. Specifically, the vertex selection probability $P_{V|E}(e \rightarrow v)$ and the edge selection probability $P_{E|V}(v \rightarrow e)$ are both defined as in DIPHW (section II B), while all other probability distributions remain as specified in section II C.

D. Cell Embedding and Clustering

We perform random walks using the defined hypergraph node-to-edge and edge-to-node transition probabilities to sample sequences of visited cells. These sampled cell paths, which capture the geometry of the hypergraph representing the scRNA-seq data, are then used as input to

word2vec [45] to learn low-dimensional vector representations of cells. Cells with similar expression profiles frequently co-occur in the sampled random walk paths and are closer in the embedded space. Finally, K-means clustering is applied to cell embeddings to obtain cluster assignments.

E. scRNA-seq Data Simulation

In our study, we develop an algorithm to simulate data that mimics the characteristics of scRNA-seq expression data (see Algorithm 1). In addition to the underlying assumption of within-cell-type homogeneous expression that governs most cell clustering methods, we incorporate between-cell-type crosstalk [46–50] by integrating configurable intermodular covariance, density, and signal strength into the simulation model. The algorithm generates a sparse matrix representing the simulated scRNA-seq expression data, with numerous user-configurable parameters, including number of modules, module density, shape, background signal strength, modular signal strength, intermodular signal strength, intermodular covariance, and noise level (see Table S4). This method is implemented as a function in our codebase and is available for use by other researchers [51].

Our simulation model is highly flexible to accommodate various types of scRNA-seq data. For example, the model can simulate both sequenced datasets with high density (up to 50%) and sequenced datasets with low density (as low as 1%) [52]. The proportion of non-housekeeping genes can be adjusted by changing the number of differentially expressed genes (DEGs) in each module. In addition, the variance in module sizes and the number of co-expressed genes in each cell type can be configured by setting different variances for the Poisson distribution used in the embedded module simulation. The modules embedded in the simulated data can be configured with higher density and average signal strength to model the expression profiles of biomarker genes that are highly expressed in certain cell types. This enables us to mimic the sparsity and modularity of real scRNA-seq data, where a small number of genes are highly expressed in specific cell types. Alternatively, the embedding modules can be user-specified without using the embedded module simulation.

Algorithm 1 Simulation Algorithm for scRNA-seq Data

- 1: **Input:** Number of genes E , number of cells V , number of cell types K ; average genes per cell type \bar{g} and average cells per cell type \bar{c} ; average expression levels for within-cell-type λ_{ct} , cross-cell-type λ_{cross} , and background λ_{bg} ; densities within-cell-type ρ_{ct} , cross-cell-type ρ_{cross} , and background ρ_{bg} ; and crosstalk probability p_{cross} .
- 2: **Output:** Sparse expression matrix $\mathbf{X} \in \mathbb{R}^{E \times V}$ with ground-truth labels.
- 3: Initialize $\mathbf{X} \leftarrow \mathbf{0}_{E \times V}$.
- 4: Sample cell type sizes: $g_k \sim \text{Poisson}(\bar{g})$, $c_k \sim \text{Poisson}(\bar{c})$ for $k = 1, \dots, K$.
- 5: *Phase 1: Within-Cell-Type Signal*
- 6: **for** each cell type $k = 1, \dots, K$ **do**
- 7: For each gene $e \in E_k$ and cell $v \in V_k$: with probability ρ_{ct} , set $\mathbf{X}[e, v] \leftarrow \text{Poisson}(\lambda_{ct})$.
- 8: **end for**
- 9: *Phase 2: Background Noise*
- 10: Randomly fill ρ_{bg} fraction of remaining zero entries with $\text{Poisson}(\lambda_{bg})$ values.
- 11: *Phase 3: Cross-Cell-Type Crosstalk*
- 12: **for** each cell type pair (k, l) where $k \neq l$ **do**
- 13: With probability p_{cross} : randomly fill ρ_{cross} fraction of $\mathbf{X}[E_k, V_l]$ with $\text{Poisson}(\lambda_{cross})$ values.
- 14: **end for**
- 15: **return** \mathbf{X} , ground-truth labels.

III. EXPERIMENTS AND RESULTS

A. Baseline and Competing Methods

To evaluate the performance of DIPHW and CoMem-DIPHW, we compared them with 13 cell-clustering methods from various categories, including community detection, embedding-based methods, and recent deep learning methods that cluster scRNA-seq data. Table II summarizes these methods. For a fair comparison under consistent conditions, we focus on core clustering algorithms rather than specific implementations in packages such as Seurat [15], Scanpy [17], and WGCNA [14]. This approach allows us to evaluate the clustering capabilities of each method independently of any additional preprocessing or optimization steps. The hyperparameters used

for each experiment are detailed in Table S4 in the supplementary materials.

Method	Type	Input	Packages
Greedy Modularity [53]	Community detection	Cell co-expression network	igraph [54]
Louvain [55]	Community detection	Cell co-expression network	Seurat [15], Scanpy [17], WGCNA [14]
Infomap [56]	Community detection	Cell co-expression network	igraph [54]
Leiden [57]	Community detection	Cell co-expression network	igraph [54]
PCA [58]	Linear embedding	Gene \times cell matrix	Seurat [15], Scanpy [17], SC3 [59], Cell Ranger [22]
t-SNE [60]	Manifold embedding	Gene \times cell matrix	Seurat [15], Scanpy [17]
UMAP [61]	Manifold embedding	Gene \times cell matrix	Seurat [15], Scanpy [17]
Node2Vec [62]	Graph embedding	Cell co-expression network	Multiple implementations available [63, 64]
graph-sc [65]	Deep graph embedding	Cell co-expression network	GitHub [66]
tsImpute [67]	Imputation	Gene \times cell matrix	GitHub [68]
CAKE [69]	Deep contrastive clustering	Gene \times cell matrix	GitHub [70]
scASDC [71]	Deep clustering	Gene \times cell matrix	GitHub [72]
EDVW [44] + word2vec [73]	Hypergraph embedding	Gene \times cell matrix	Implemented based on [44]; GitHub [51]
DIPHW + word2vec [73]	Hypergraph embedding	Gene \times cell matrix	Our proposed method; GitHub [51]
CoMem + word2vec [73]	Hypergraph embedding	Gene \times cell matrix, plus gene and cell co-expression networks	Our proposed method; GitHub [51]

TABLE II: List of Clustering Methods Evaluated in Our Study. K-means was used to cluster the output of all embedding-based methods that do not include a clustering algorithm. Since tsImpute is an imputation method, we evaluated its impact on clustering performance by applying PCA followed by K-means to its imputed data.

B. Data and Preprocessing

We use simulated and publicly available scRNA-seq datasets for our study. The simulated data is generated using our simulation algorithm described in Section II E, with pseudocode in Algorithm 1 and code at [51].

For both simulated and real scRNA-seq data, preprocessing includes Counts Per Million normalization [74] to account for differences in sequencing depth, log transformation to reduce skewness, and removal of genes and cells with zero total expression. For real scRNA-seq datasets, we additionally retain the top n highly variable genes using Scanpy’s implementation of the Seurat [15] method. The values of n used for each dataset are provided in Table S4.

We use six publicly available scRNA-seq datasets: (1) human brain [75], (2) human pancreas [76], (3) mouse brain [77], (4) mouse pancreas [78], and (5) scMixology benchmark with 3

classes and (6) scMixology benchmark with 5 classes. scMixology benchmark which is a curated benchmark dataset with ground-truth cell line labels [79]. Table II provides a summary of these datasets.

Datasets	# of Cells	# of Genes	Sparsity	Results in
scMixology Benchmark (3-class) [79]	902	16,468	45.02%	Table IV
scMixology Benchmark (5-class) [79]	3,918	11,786	63.01%	Table IV
Human Pancreas [76]	3,072	18,348	78.74%	Section III F
Human Brain [75]	735	18,929	80.11%	Section S6
Mouse Brain [77]	3,006	19,973	81.21%	Section S7
Mouse Pancreas [78]	1,065	14,881	87.79%	Section S7

TABLE III: List of Publicly Available Datasets Used in Our Study. Sparsity measures the percentage of zero entries in a cell \times gene matrix.

C. Sparsity-Induced Inflated Correlation in scRNA-seq Co-expression Networks

The zero inflation problem in scRNA-seq data analysis refers to the excessive number of zero counts (or "dropouts") observed in the data. These zeros may arise from technical limitations in detecting low-abundance transcripts (false negatives) or from the true absence of transcripts (true negatives) [33, 35, 36]. Integrating individual cell expression profiles into a unified scRNA-seq dataset requires constructing a matrix that includes every gene detected in any cell, which introduces zero entries wherever genes are not expressed in those cells. Because cells typically express different sets of genes, this process creates significant sparsity in the merged dataset. In co-expression network construction, edge weights are inflated due to these artificially introduced common zeros, as the common zeros are interpreted as evidence of expression homogeneity. This issue is especially pronounced at the single-cell level compared to bulk tissue RNA-seq data, since the proportion of expressed genes per cell is much smaller, resulting in greater data sparsity.

In Fig. 3, we examine how induced sparsity affects correlation coefficients and the interpretation of gene and cell connections in co-expression networks. To simulate this effect, we generate gene expression data with a fixed base size and introduce varying proportions of zeros to represent different sparsity levels. Our results indicate that as induced sparsity increases, correlation coefficients between expression profiles become artificially inflated, leading to an overestimation of

similarity between cell expression profiles. These findings highlight the importance of addressing zero inflation in scRNA-seq data analysis and the need for accurate representation of underlying biological relationships.

Table S1 (in the Supplementary Section S1) shows that ignoring shared zeros using cosine similarity results in poorer clustering performance, as these inactive genes still have biological significance.

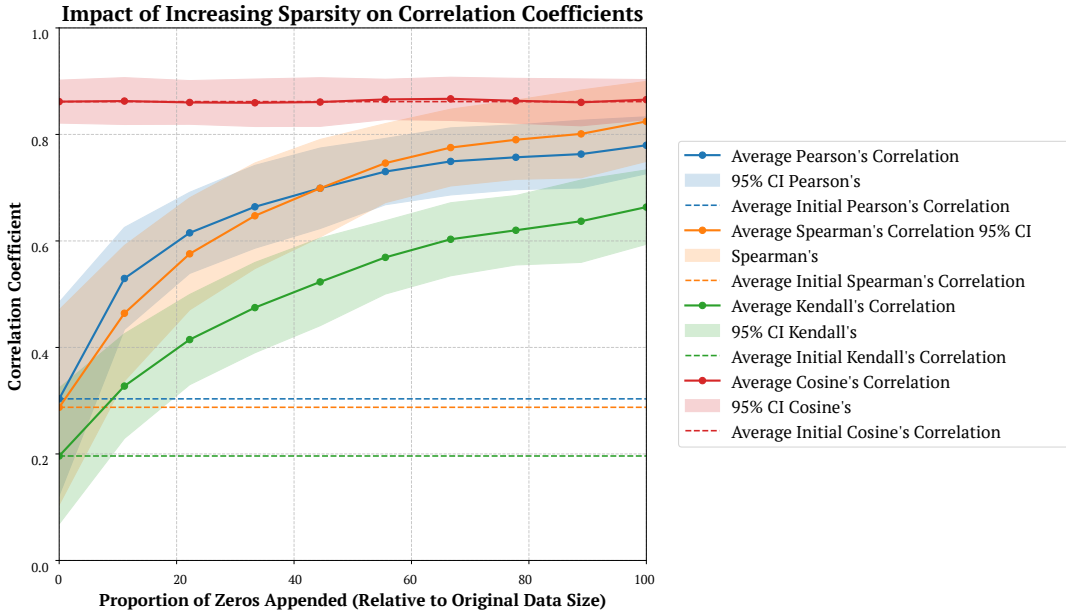


FIG. 3: Impact of Increased Sparsity on Correlation Coefficients. This figure shows the relationship between the proportion of zeros added to the expression profile (representing increased sparsity) and the resulting correlation coefficients. This process was repeated 100 times. Shaded areas indicate the 95% confidence intervals around the average correlation values. The dashed lines represent the average initial correlation without added sparsity. Induced sparsity in scRNA-seq data can inflate correlations in co-expression networks, highlighting the need for alternative scRNA-seq data representations.

D. Results on the Simulated Data

To evaluate performance of the clustering methods on datasets with known ground-truth, we employ five widely used measures to compute coherence between the identified clusters and the ground-truth clusters: Adjusted Rand Index (ARI), Normalized Mutual Information (NMI), Adjusted Mutual Information (AMI), Clustering Accuracy (ACC), and F1 Score. All evaluation measures are invariant to permutations, with a score of 0 representing random labeling and a score of 1 indicating identical clusters. K-means is used to cluster the output of all embedding-based methods that do not directly assign cluster membership.

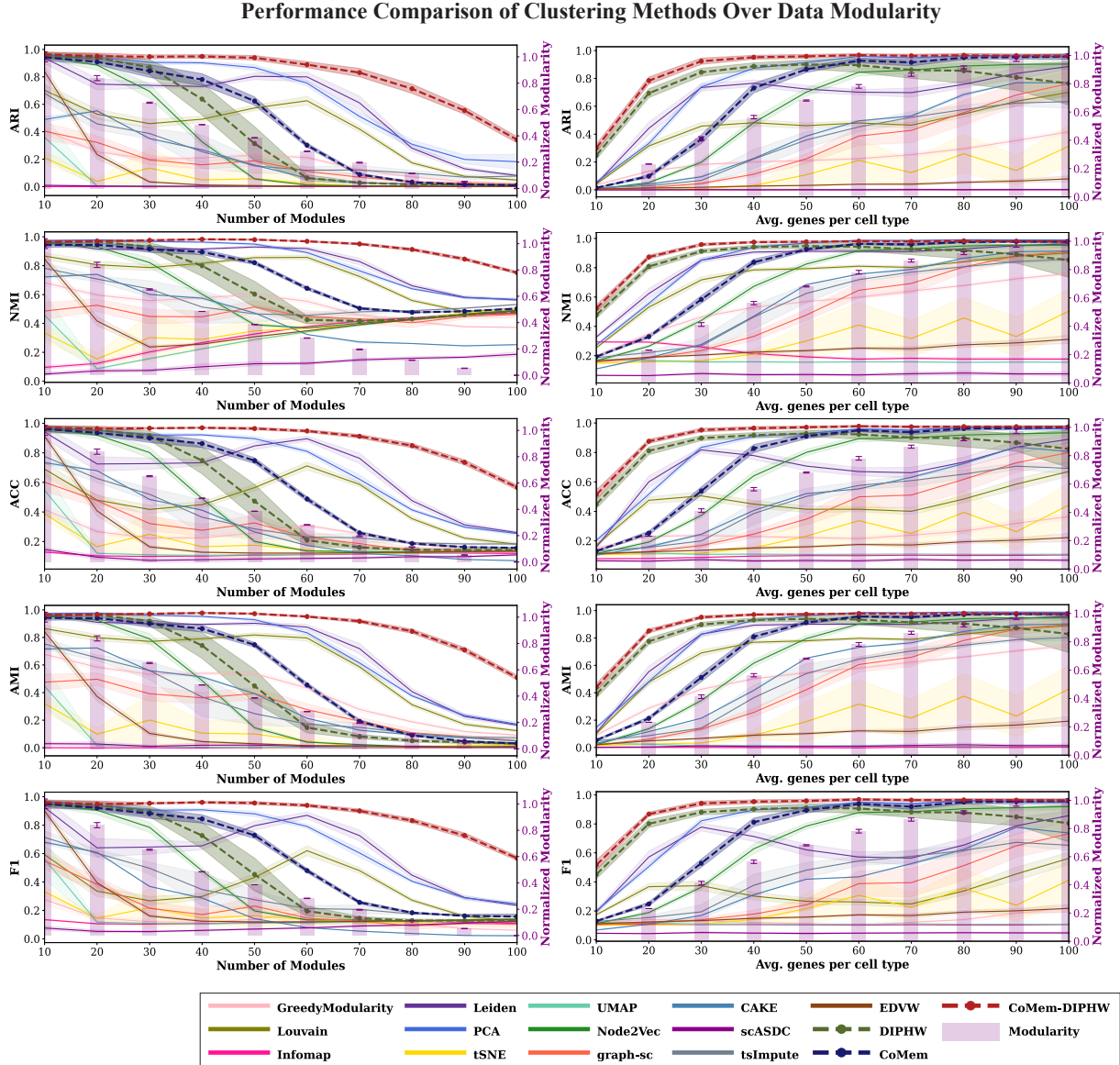


FIG. 4: Comparing Performances of Clustering Methods on Simulated scRNA-seq Data Across Modularity. The performance of clustering methods is measured by ARI, NMI, ACC, AMI, and F1 across different levels of data modularity. The x-axis represents parameters determining data modularity, including the average number of co-expressed genes per cell type and the number of embedded modules. Our proposed methods, DIPHW, CoMem, and CoMem-DIPHW, are highlighted with dashed lines. CoMem-DIPHW, in particular, maintains strong performance and is least affected by decreases in modularity, performing significantly better even under conditions of extremely weak modularity. This behavior is observed consistently across all evaluation measures. Experiments are repeated 10 times for each parameter setting, and the 95% confidence intervals (CIs) are shown. The bar plots represent Barber's bipartite modularity, normalized so that the most modular graphs have modularity = 1. K-means is used to cluster the output of all embedding-based methods that do not include an inherent clustering mechanism.

We evaluate the performance of clustering methods under varying data modularity conditions. Modularity is controlled by two key parameters: the average number of co-expressed genes per cell type and the number of embedded cell modules. The number of modules corresponds to the

number of cell types in the simulated scRNA-seq data. Weak modularity refers to a small number of co-expressed genes per module or a large number of embedded modules, which makes data structures more difficult to detect. The modularity bar plots in Fig. 4 and the heatmap visualization in Fig. S11 show that the simulated scRNA-seq data exhibit stronger modularity when the average number of co-expressed genes per cell type is higher or when the number of modules is smaller. We implemented Barber’s bipartite modularity [80], as shown in the bar plots in Fig. 4, to quantify the modularity of the underlying data for clustering and to analyze the association between modularity and clustering performance. Clustering performance generally improves as data modularity increases. Our proposed methods, DIPH, CoMem, and CoMem-DIPH, demonstrate strong and highly competitive performance across varying modularity. Specifically, CoMem-DIPH consistently remains competitive with the best-performing methods evaluated, with its advantage particularly pronounced under weak data modularity conditions. For clarity, we present the most contrasting cases from our analysis: (i) an average of 10 and 100 co-expressed genes per module in Fig. 5 and (ii) 10 and 100 embedded modules in Fig. 6.

In Figures 5 and 6, we compare the performance of our proposed hypergraph-based clustering methods (highlighted in red and yellow) with five embedding-based approaches, four community detection algorithms, and four state-of-the-art scRNA-seq clustering methods. K-means is used to cluster the output of all embedding-based methods that do not directly assign cluster membership. In weak modularity regimes (average number of co-expressed genes per module = 10 or number of modules = 100), CoMem-DIPH and DIPH show a clear performance advantage. For example, when the average number of co-expressed genes is 10, CoMem-DIPH achieves an ARI of 0.30 and DIPH achieves an ARI of 0.25, compared to 0.05 for the best baseline method (PCA), representing a performance improvement of nearly 450%. Under strong modularity conditions (average number of genes per module = 100 or number of modules = 10), multiple methods (PCA, CoMem-DIPH, CoMem, and Node2Vec) performed well, achieving average ARI scores above 0.9.

Additional results from intermediate parameter settings (average number of co-expressed genes per module: 20, 30, 40, 70, 80, 90; number of embedded modules: 20, 30, 40, 70, 80, 90), as measured by NMI, ACC, AMI, and F1, support the same observation. Across the 16 parameter settings under different modularity conditions, CoMem-DIPH ranks first in all 16 settings by ACC and F1, 15 by ARI, and 10 each by NMI and AMI. DIPH and CoMem also perform strongly. Either DIPH or CoMem rank among the top three methods in at least 10 of 16 settings

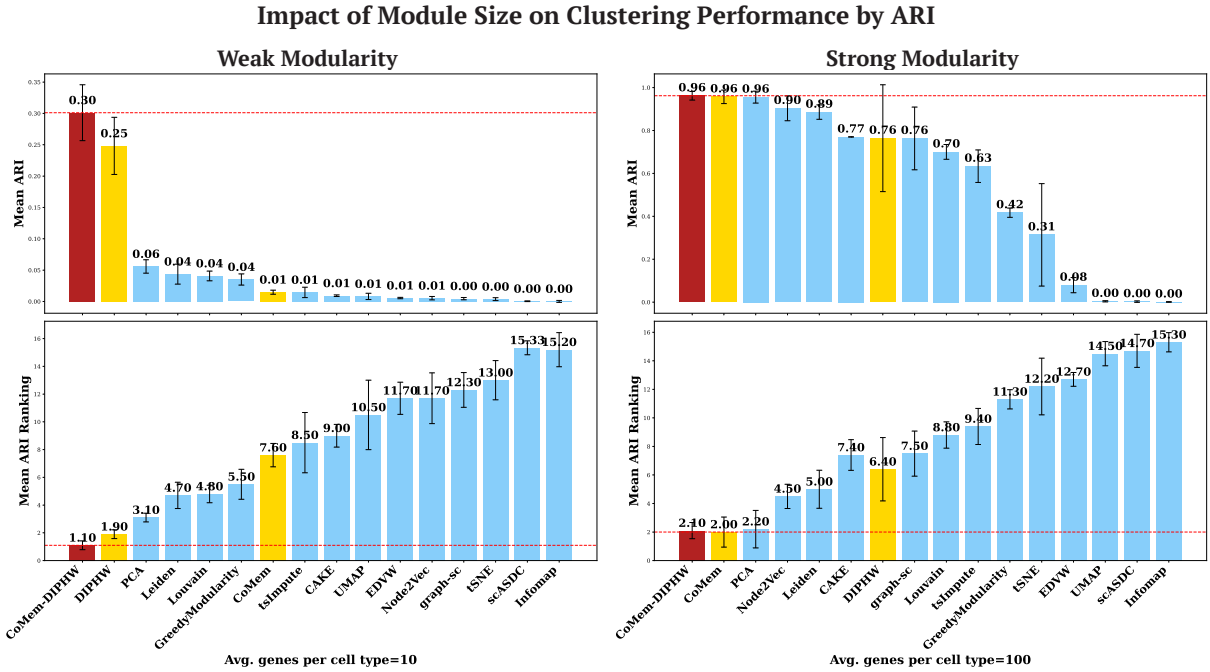


FIG. 5: Impact of Module Size on Clustering Performance by ARI. The bar plots show the mean ARI (top) and average ranking (bottom) for each method, ordered by their average ARI. Each experiment was repeated 10 times per parameter setting, with error bars representing the 95% confidence interval. Red dashed lines indicate the highest ARI values or best ARI rankings. Our proposed hypergraph-based methods, highlighted in red and yellow, show significant advantages when data modularity is weak, that is, when the average number of co-expressed genes per cell type module is low (10 genes per module). Under strong modularity conditions, where the average number of genes per cell type module is high (100 genes per module), many methods (e.g., PCA, CoMem-DIPHWH, CoMem, and Node2Vec) perform well and achieve average ARI scores above 0.9. These observations are consistent across NMI, ACC, AMI, and F1, as shown in Supplementary Section S5. K-means is used to cluster the output of all embedding-based methods that do not directly assign cluster membership.

across all evaluation measures. Our hypergraph-based methods show significant advantages in weak modularity regimes, where data structures are harder to detect. Under comparatively strong modularity conditions, several methods (PCA, CoMem-DIPHWH, CoMem, Node2Vec, DIPHWH, and Leiden) perform well, with average NMI scores above 0.9. Notably, PCA slightly outperforms CoMem-DIPHWH by ARI, NMI, and AMI under strong modularity, with differences in scores ranging from 0.01 to 0.02. These additional results are in Supplementary Section S5.

E. Results on the scMixology Benchmark Datasets

A major challenge in scRNA-seq analysis is the lack of reliable ground truth for cell type annotation, which complicates the evaluation of clustering algorithms. In most scRNA-seq datasets, cell type labels are assigned using a combination of clustering results, differential expression (DE)

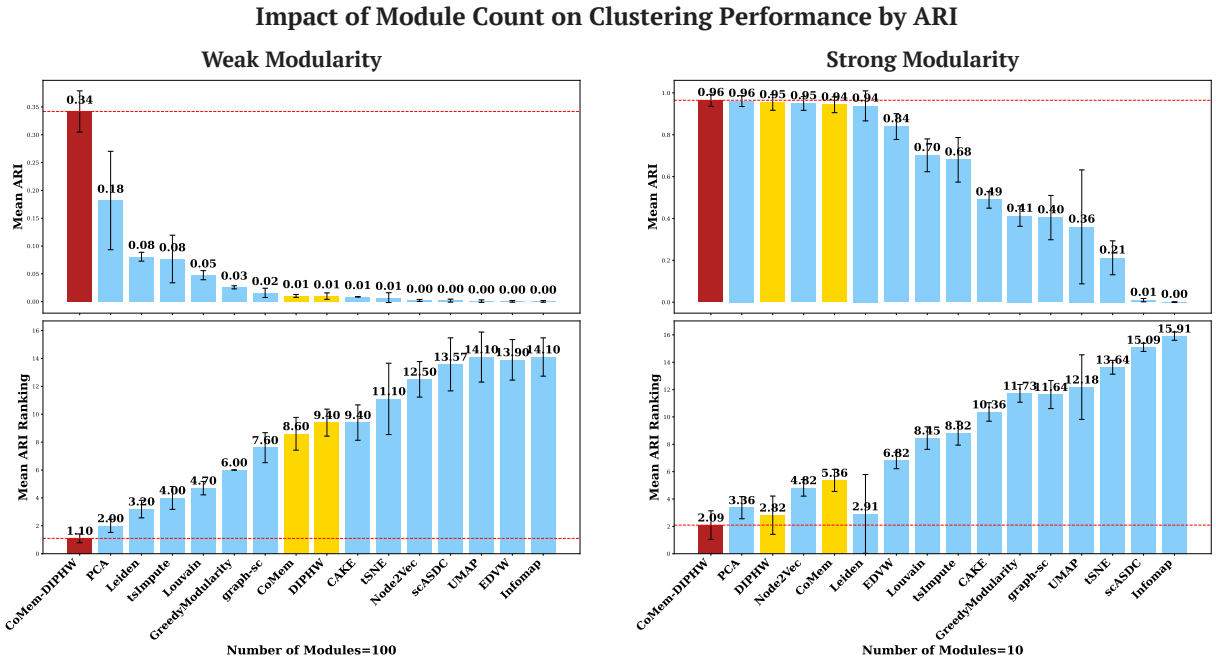


FIG. 6: Impact of Module Count on Clustering Performance by ARI. The bar plots show the mean ARI (top) and average ranking (bottom) of each method, ordered by their average ARI. Our proposed hypergraph-based methods, highlighted in red and yellow, demonstrate significant advantages in weak modularity regimes, where the number of embedded modules (representing the number of cell types) in the simulated data is high (100 modules). Each experiment is repeated 10 times per parameter setting, with error bars representing the 95% confidence interval. Red dashed lines indicate the highest ARI values or best ARI rankings. These observations are consistent across NMI, ACC, AMI, and F1, as shown in Supplementary Section S5. K-means is used to cluster the output of all embedding-based methods that do not directly assign cluster membership.

analysis, and canonical marker genes. First, cells are grouped into clusters based on transcriptomic similarity using clustering algorithms such as K-means. Next, DE analysis identifies genes that are differentially expressed across clusters. Finally, these clusters are annotated based on known canonical marker genes associated with specific cell types. Because this annotation process relies on clustering results, using these labels to evaluate clustering performance introduces circular logic and bias toward the method originally used for annotation. To address this issue, we use the mixture control benchmarking dataset scMixology [79], where ground truth is established based on cell line identity.

We evaluate the performance of our proposed method, CoMem-DIPH, using two benchmarking datasets from scMixology [79]. These datasets provide ground truth labels for cell type annotation based on human lung adenocarcinoma cell lines. As shown in Table IV, tsImpute achieved the highest scores across all five evaluation measures (ARI, NMI, AMI, ACC, and F1) on the 3-class dataset, with CoMem-DIPH, Louvain, and Leiden tied for second. On the 5-class dataset,

CoMem-DIPHW achieved the best performance across all evaluation measures, followed by tsImpute and graph-sc. This result is consistent with the pattern observed in our simulation analysis (see Section III D), where CoMem-DIPHW maintains strong performance under low modularity conditions.

Traditional Embedding and Community Detection Methods									
Dataset / Evaluation Measures	GreedyModularity	Louvain	Infomap	Leiden	PCA	t-SNE	Node2Vec	UMAP	
<i>scMixology 3 class</i>									
ARI	0.584 ± 0.000	<u>0.993 ± 0.000</u>	0.233 ± 0.000	<u>0.993 ± 0.000</u>	0.990 ± 0.000	0.990 ± 0.000	0.991 ± 0.004	0.990 ± 0.000	
NMI	0.719 ± 0.000	<u>0.986 ± 0.000</u>	0.384 ± 0.000	<u>0.986 ± 0.000</u>	0.980 ± 0.000	0.981 ± 0.000	0.983 ± 0.008	0.981 ± 0.000	
ACC	0.693 ± 0.000	<u>0.998 ± 0.000</u>	0.337 ± 0.000	<u>0.998 ± 0.000</u>	0.996 ± 0.000	0.997 ± 0.000	0.997 ± 0.001	0.997 ± 0.000	
AMI	0.719 ± 0.000	<u>0.986 ± 0.000</u>	0.234 ± 0.000	<u>0.986 ± 0.000</u>	0.980 ± 0.000	0.981 ± 0.000	0.983 ± 0.008	0.981 ± 0.000	
F1	0.587 ± 0.000	<u>0.998 ± 0.000</u>	0.459 ± 0.000	<u>0.998 ± 0.000</u>	0.997 ± 0.000	0.997 ± 0.000	0.997 ± 0.001	0.997 ± 0.000	
<i>scMixology 5 class</i>									
ARI	0.665 ± 0.000	0.675 ± 0.000	0.300 ± 0.0008	0.675 ± 0.000	0.987 ± 0.000	0.986 ± 0.000	0.945 ± 0.007	0.984 ± 0.000	
NMI	0.785 ± 0.000	0.795 ± 0.000	0.436 ± 0.000	0.792 ± 0.000	0.975 ± 0.000	0.974 ± 0.000	0.915 ± 0.009	0.971 ± 0.000	
ACC	0.733 ± 0.000	0.736 ± 0.000	0.415 ± 0.002	0.736 ± 0.000	0.994 ± 0.000	0.994 ± 0.000	0.962 ± 0.006	0.993 ± 0.000	
AMI	0.785 ± 0.000	0.795 ± 0.000	0.274 ± 0.000	0.792 ± 0.000	0.975 ± 0.000	0.974 ± 0.000	0.915 ± 0.009	0.971 ± 0.000	
F1	0.656 ± 0.000	0.658 ± 0.000	0.525 ± 0.003	0.657 ± 0.000	0.994 ± 0.000	0.994 ± 0.000	0.962 ± 0.006	0.993 ± 0.000	
Advanced ScRNA-seq and Hypergraph-Based Methods									
Dataset / Evaluation Measure	EDVW	graph-sc	tsImpute	CAKE	scASDC	DIPH	CoMem	CoMem-DIPH	
<i>scMixology 3 class</i>									
ARI	0.596 ± 0.045	0.702 ± 0.265	0.997 ± 0.000	0.832 ± 0.020	0.423 ± 0.434	0.990 ± 0.005	0.991 ± 0.002	<u>0.993 ± 0.000</u>	
NMI	0.614 ± 0.027	0.765 ± 0.188	0.993 ± 0.000	0.861 ± 0.021	0.450 ± 0.440	0.980 ± 0.010	0.983 ± 0.003	<u>0.986 ± 0.000</u>	
ACC	0.800 ± 0.056	0.861 ± 0.128	0.999 ± 0.000	0.996 ± 0.001	0.644 ± 0.296	0.997 ± 0.002	0.997 ± 0.001	<u>0.998 ± 0.000</u>	
AMI	0.613 ± 0.027	0.765 ± 0.189	0.993 ± 0.000	0.861 ± 0.021	0.448 ± 0.442	0.980 ± 0.010	0.983 ± 0.003	<u>0.986 ± 0.000</u>	
F1	0.799 ± 0.056	0.851 ± 0.138	0.999 ± 0.000	0.996 ± 0.001	0.548 ± 0.381	0.997 ± 0.002	0.997 ± 0.001	<u>0.998 ± 0.000</u>	
<i>scMixology 5 class</i>									
ARI	0.657 ± 0.022	0.988 ± 0.002	<u>0.989 ± 0.000</u>	0.733 ± 0.075	0.392 ± 0.360	0.944 ± 0.003	0.988 ± 0.001	0.990 ± 0.002	
NMI	0.742 ± 0.020	0.978 ± 0.002	<u>0.980 ± 0.000</u>	0.844 ± 0.022	0.458 ± 0.416	0.909 ± 0.004	0.977 ± 0.003	0.980 ± 0.003	
ACC	0.699 ± 0.016	0.995 ± 0.001	<u>0.995 ± 0.000</u>	0.857 ± 0.019	0.555 ± 0.216	0.963 ± 0.002	0.995 ± 0.001	0.996 ± 0.001	
AMI	0.742 ± 0.020	0.978 ± 0.002	<u>0.980 ± 0.000</u>	0.843 ± 0.022	0.457 ± 0.417	0.909 ± 0.004	0.977 ± 0.003	0.980 ± 0.003	
F1	0.711 ± 0.014	<u>0.995 ± 0.001</u>	0.995 ± 0.000	0.858 ± 0.018	0.344 ± 0.225	0.963 ± 0.002	0.995 ± 0.001	0.996 ± 0.001	

TABLE IV: Performance of Clustering Methods on the scMixology Benchmark Datasets [79] across Five Evaluation Measures (ARI, NMI, ACC, AMI, and F1). The scMixology benchmark datasets include a 3-class and a 5-class dataset. Results for each are shown in the top and bottom sections, respectively. Best values are in bold, and second best are underlined. Results are reported as mean ± standard deviation over five independent runs. On the 3-class dataset, tsImpute achieved the highest scores across all evaluation measures, with CoMem-DIPH, Louvain, and Leiden tied for second. On the more challenging 5-class dataset, CoMem-DIPH achieved the best performance across all evaluation measures, outperforming tsImpute, which ranked second.

F. Results on the Human Pancreas Dataset

For datasets without ground-truth annotations (specifically, human pancreas, mouse pancreas, human brain, and mouse brain), we qualitatively evaluate clustering performance using differential expression (DE) analysis. We present detailed DE analysis results for the human pancreas dataset using CoMem-DIPH, PCA, graph-sc, tsImpute, CAKE, and scASDC in this section and provide results for the human brain, mouse brain, and mouse pancreas in the Supplementary Sections S6 and S7.

We report the top 10 differentially expressed genes (DEGs) from each human pancreas cell cluster identified by CoMem-DIPH (Fig. 7a), PCA (Fig. 8a), graph-sc (Fig. 9a), tsImpute (Fig. 10a), CAKE (Fig. 11a), and scASDC (Fig. 12a). To evaluate cluster purity, we examine the expression of these DEGs across clusters (Fig. 7b, Fig. 8b, Fig. 9b, Fig. 10b, Fig. 11b, Fig. 12b). An effective clustering method should yield DEGs that uniquely characterize each cluster while showing minimal expression in other clusters.

Violin plots show that the DEGs identified by CoMem-DIPH exhibit more cluster-specific expression patterns than those derived from PCA, which tend to show higher expression in multiple clusters. For example, the average expression of the DEGs from PCA Cluster 1 is higher in Clusters 2, 5, and 6. Similarly, the DEGs from Cluster 7 show higher average expression in Cluster 6. Among the comparison methods, CAKE and scASDC produced highly distinctive DEGs, with scASDC yielding clusters that showed the strongest intra-cluster cohesion and inter-cluster separability. Graph-sc and PCA show less cluster-specific profiles, with DEGs frequently expressed across multiple clusters.

To assess the biological relevance of the clusters, we cross-reference the cluster-specific DEGs (see Fig. 7a) with markers from the PanglaoDB cell type marker database (version 27 March 2020)[81]. Cell-type assignment is based on the overlap between the DEGs of each cluster and the cell type-specific markers in the PanglaoDB marker database, with a match score calculated as the proportion of matched markers (Table 7c). CoMem-DIPH (Fig. 7c) successfully annotates all nine clusters with biologically relevant pancreatic cell types. CAKE produces similarly meaningful annotations, while graph-sc has several clusters with no annotation or biologically implausible labels.

To further validate the clustering results, we examine the expression of canonical pancreatic marker genes [76], including GCG (alpha cells), INS (beta cells), SST (delta cells), PPY (PP

cells), PRSS1 (acinar cells), KRT19 (ductal cells), COL1A1 (mesenchymal cells), and ESAM (endothelial cells) in the embeddings (Fig. 7d, Fig. 8d, Fig. 9d, Fig. 10d, Fig. 11d, Fig. 12d). Each marker is distinctly expressed in the embedding generated by CoMem-DIPH, as shown in Fig. 7d, confirming that CoMem-DIPH embeddings effectively distinguish different cell types. CAKE and scASDC also produce well-separated embeddings. In contrast, PCA embeddings show poor separation. The results from CoMem-DIPH align well with the cell-type annotation by the PanglaoDB database. The only discrepancy is in Cluster 4. Matching the DEGs with PanglaoDB cell type markers suggests Pancreatic stellate cells (PSCs) or Granulosa cells, while the COL1A1 and ESAM expression plots indicate mesenchymal or endothelial cells. However, this apparent discrepancy can be explained by the fact that PSCs can differentiate into cells with endothelial-like properties [82], and granulosa cells can exhibit mesenchymal-like behaviors [83].

In contrast, PCA clustering results (Fig. 8) showed limited cluster separation. While some PCA clusters could be annotated consistently using both PanglaoDB markers and canonical markers, significant overlap remained among clusters. For example, PCA Cluster 8, identified as beta cells by both the PanglaoDB markers and the canonical marker INS, is not well separated from Cluster 5 (potentially delta cells, marked by SST expression). Similarly, Cluster 7, identified as ductal cells by both the PanglaoDB markers and the canonical marker KRT19, is closely embedded with endothelial cells (ESAM). These results highlight CoMem-DIPH's improved ability to distinguish pancreatic cell types compared to PCA.

In addition to the human pancreas results presented here, we also analyze mouse pancreas, human brain, and mouse brain datasets. For these datasets, we include visualizations in the supplementary material in Figures S12b through S29b that show the average expression of the top DEGs across clusters identified by different methods. These results show our proposed algorithm's ability in effectively distinguishing cell clusters by their expression profiles. The supplementary material (Figures S12a through S29a) also contain tables listing the top DEGs for clusters identified by CoMem-DIPH, PCA, graph-sc, tsImpute, CAKE, and scASDC in each dataset for reference.

To complement the qualitative biological validation presented above, we further assess clustering performance using quantitative cluster quality measures, including the Silhouette score, Calinski-Harabasz index, Davies-Bouldin index, and Coefficient of Variation. These evaluations are conducted in two settings: (1) directly in the learned embedding space and (2) by evaluating the same cluster assignments on the preprocessed expression data used as input to the embedding algorithms. We refer the reader to Supplementary Tables S2 and S3. Evaluation in the embed-

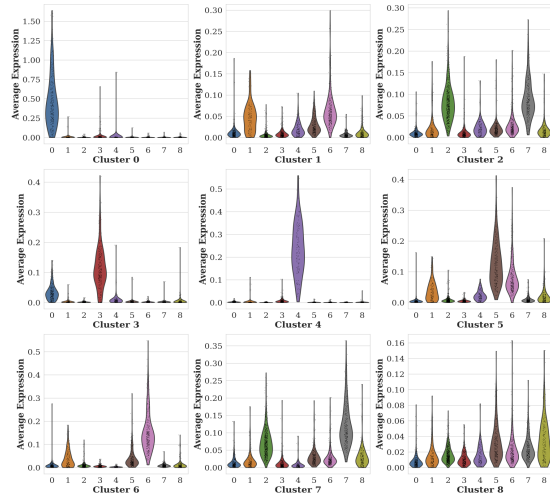
(a) Top 10 DE Genes for Each Cluster Identified by CoMem-DIPHWR in the Human Pancreas Data

Cluster	Cluster 1	Cluster 2	Cluster 3	Cluster 4
CPA2	ADCYAP1	GLS	LITAF	LAMA4
PRSS1	GEM	FAP	KRT19	NID1
CPA1	TGFBR3	ENPP2	ANXA4	SPARC
CPB1	SRXN1	KCTD12	LAD1	IGFBP4
GSTA1	NPTX2	TMEM176B	ONECUT2	EMP1
PLA2G1B	HADII	RGS4	ANXA2	COL4A1
GSTA2	UCHL1	CRYBA2	SERPING1	SERPINH1
PNLIP	HSPA1B	MAFB	SLC4A4	HTRA1
PRSS3P2	SYT13	LOXL4	CFTR	PXDN
CTRB1	CDKN1A	NA20	CLDN1	COL4A2

(c) Top Cell Type Matches for Each Cluster Identified by CoMem-DIPHWR Based on PanglaoDB Markers

Cluster	Match Type	Annotation	Score
0	Primary	Acinar cells	0.1875
	Secondary	Foveolar cells	0.0952
1	Primary	Beta cells	0.0784
	Secondary	Alpha cells	0.1277
3	Primary	Ductal cells	0.1163
	Secondary	Ionocytes	0.0909
4	Primary	Pancreatic stellate cells	0.0690
	Secondary	Granulos cells	0.0625
5	Primary	Delta cells	0.1765
	Secondary	Parathyroid chief cells	0.1250
6	Primary	Beta cells	0.1373
	Secondary	Delta cells	0.0882
7	Primary	Alpha cells	0.0851
	Secondary	Retinal progenitor cells	0.0769
8	Primary	Gamma (PP) cells	0.1034
	Secondary	Retinal progenitor cells	0.0769

(b) Average Expression of Top 10 DE Genes from Each Cluster Found by CoMem-DIPHWR



(d) Expression of Marker Genes in CoMem-DIPHWR Embeddings

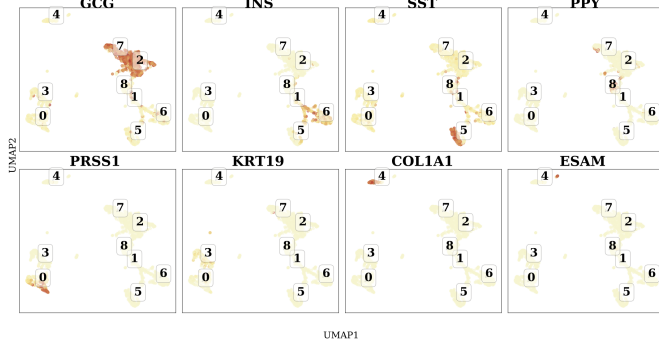


FIG. 7: Clustering Performance of CoMem-DIPHWR on the Human Pancreas Dataset and Cell Type Annotation Using Differentially Expressed Genes (DEGs) and Canonical Markers. (a) Top 10 DEGs per cluster identified by CoMem-DIPHWR. For example, Cluster 0 (acinar cells) includes genes associated with digestive enzyme production, a primary function of pancreatic acinar cells, including CPA1, CPA2 [84], PLA2G1B [85], CTRB1 [86], and PRSS1 [87]. Clusters 2 and 7 (alpha cells) include markers GLS, CRYBA2, FAP, LOXL4, MAFB, and RGS4 (cluster 2), and LOXL4, PAX6, RGS4, and CRYBA2 (cluster 7). Cluster 3 (ductal cells) includes SLC4A4, ANXA4, KRT19, CFTR, CLDN1, and ONECUT2. Cluster 4, likely mesenchymal or endothelial cells, aligns with 9 of the top 10 DEGs found by CoMem-DIPHWR, including COL4A2, COL4A1, SPARC, EMP1, IGFBP4, HTRA1, PXDN, LAMA4, and NID1. Cluster 5 (delta cells) includes GAD2, PCSK1, LEPR, and CASR, while Cluster 6 (beta cells) includes MAFA, ERO1LB, PDX1, IAPP, SYT13, HADH, and ADCYAP1. Cell type assignments are based on canonical marker expression patterns shown in (d). (b) Across-cluster average expression of cluster-specific DEGs. Violin plots show the distribution of average expression levels of these DEGs across all clusters. Strong clustering performance is indicated by high within-cluster expression of DEGs and low expression in other clusters. (c) Cell type annotation using the PanglaoDB marker database. Cell types are determined by the overlap between each cluster's DEGs and PanglaoDB cell type-specific markers, with match scores computed based on the proportion of matched markers. (d) Expression of human pancreatic canonical markers in CoMem-DIPHWR embeddings. UMAP visualizations show CoMem-DIPHWR cell embeddings, with cluster IDs assigned by K-means clustering. Each subplot displays the expression of a canonical marker gene for a specific human pancreatic cell type. The cell-type-specific markers considered include GCG (alpha cells), INS (beta cells), SST (delta cells), PPY (PP cells), PRSS1 (acinar cells), KRT19 (ductal cells), COL1A1 (mesenchymal cells), and ESAM (endothelial cells). Color intensity represents gene expression levels, with red hues indicating higher expression. Clusters showing high expression of cell-type-specific canonical markers are assigned to the corresponding cell types. Overall, clustering quality is demonstrated by (b) high within-cluster DEG expression, (c) consistency between PanglaoDB-based annotation and clustering, and (d) distinct separation of cell types.

(a) Top 10 DE Genes for Each Cluster Identified by PCA in the Human Pancreas Data

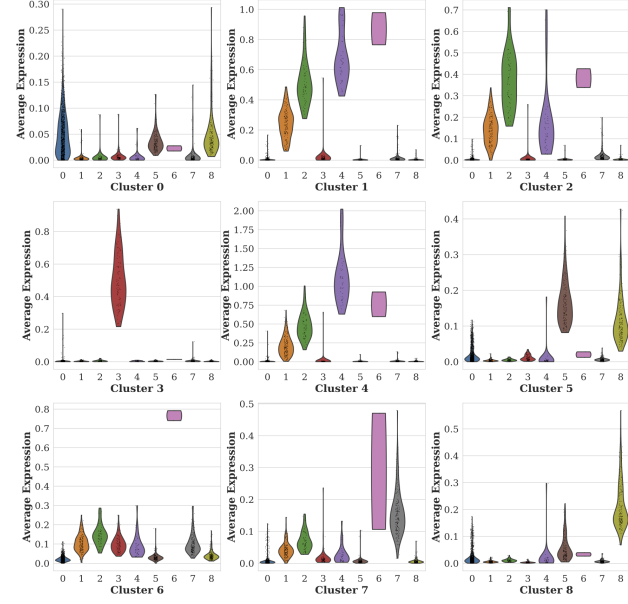
Cluster 0	Cluster 1	Cluster 2	Cluster 3	Cluster 4
ENPP2	MUC1	TC2N	COL5A1	CEL
CRYBA2	GSTA1	LYZ	NID1	CTRC
PCSK1N	MGST1	AOX1	COL5A2	CPA1
RGS4	CPA2	ALDOB	COL1A1	CELA8A
KCTD12	CPA1	GSTA1	COL6A3	PRSS3P2
LOXL4	BCAT1	AKR1C3	COL6A2	PRSS1
TMEM176B	PRSS3P2	GSTA2	COL3A1	CPB1
NEUROD1	GSTA2	ANPEP	CDH11	CLPS
PAX6	PRSS1	CYB5A	COL1A2	PLA2G1B
FABP5	PLA2G1B	ALB	COL6A1	GP2

Cluster 5	Cluster 6	Cluster 7	Cluster 8
GAD2	RPS4X	SLC4A4	NPTX2
LEPR	NCOA7	CFTR	PDX1
HADH	TMEM123	CTSH	MAFA
RBP4	NFIB	CLDN1	PFKFB2
UCHL1	YWHAZ	SELL1L3	EROLB
SYT13	RPL27	ANXA4	HADH
SORL1	MYH9	KRT19	IAPP
SNAP25	MYL12B	ATP1A1	ABCC8
CASR	MYO6	LITAF	SYT13
PCSK1	MYL12A	SERPING1	SORL1

(c) Top Cell Type Matches for Each Cluster Identified by PCA Based on PanglaoDB Markers

Cluster	Match Type	Annotation	Score
0	Primary	Alpha cells	0.1064
	Secondary	Enteroendocrine cells	0.0833
1	Primary	Acinar cells	0.1458
	Secondary	Foveolar cells	0.1429
2	Primary	Acinar cells	0.1250
	Secondary	Gastric chief cells	0.1000
3	Primary	Pancreatic stellate cells	0.2069
	Secondary	Myofibroblasts	0.1111
4	Primary	Acinar cells	0.1667
	Secondary	Foveolar cells	0.0952
5	Primary	Parathyroid chief cells	0.1250
	Secondary	Delta cells	0.1176
6	Primary	No annotation	-
7	Primary	Ductal cells	0.1395
	Secondary	Ionocytes	0.0909
8	Primary	Beta cells	0.1176
	Secondary	Delta cells	0.0882

(b) Average Expression of Top 10 DE Genes from Each Cluster Found by PCA



(d) Expression of Marker Genes in PCA Embeddings

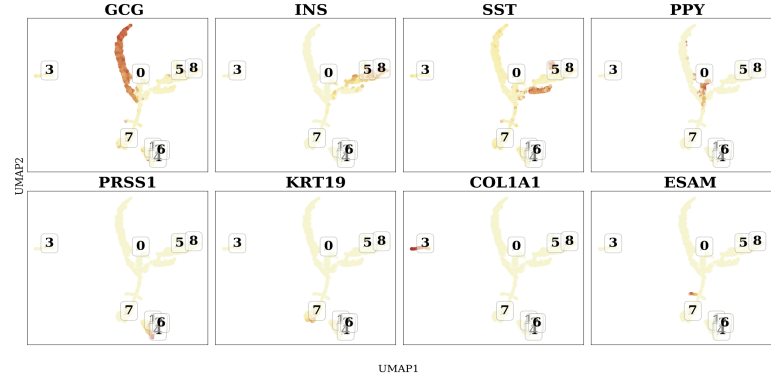


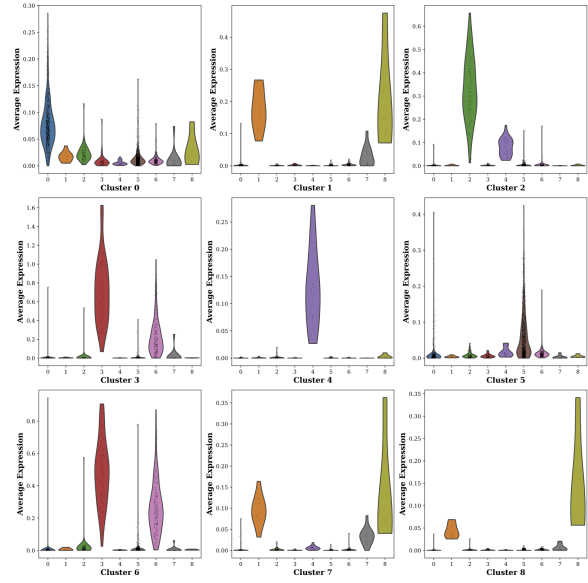
FIG. 8: Clustering Performance of PCA on the Human Pancreas Dataset and Cell Type Annotation Using Differentially Expressed Genes (DEGs) and Canonical Markers. (a) Top 10 DEGs per cluster identified by PCA. (b) Average expression of cluster-specific DEGs across clusters. Strong clustering performance is indicated by high expression of cluster-specific DEGs within their respective clusters and low expression in other clusters. (c) Cell type annotation using the PanglaoDB marker database. (d) Expression of human pancreatic canonical markers in PCA embeddings. UMAP visualizations show PCA cell embeddings, with cluster IDs assigned by K-means clustering. Overall, the clustering of cell types is limited compared to CoMem-DIPHW clustering, as shown by the overlapping beta cells, delta cells, and PP cells in (d) and the absence of distinct high expression patterns of the DEGs in (b).

ding space captures the geometric separability and cohesion of clusters, whereas evaluation on the preprocessed data assesses whether the resulting cluster assignments capture meaningful structure in the input gene expression data. As demonstrated by differential expression and cell-type annotation analyzes in the human pancreas data set, strong embedding-space cohesion and separation alone do not necessarily guarantee biological interpretability.

(a) Top 10 DE Genes for Each Cluster Identified by graph-sc in the Human Pancreas Data

Cluster 0	Cluster 1	Cluster 2	Cluster 3	Cluster 4
GC	CD53	SPARC	PNLIPRP1	PLVAP
CRYBA2	TYROBP	COL4A1	CELA3A	FILT1
KCTD12	SDS	FN1	CTRB1	KDR
TMEM176B	C1QB	COL4A2	CTRC	SOX18
RGS4	IFI30	COL5A1	CELA3B	EXOC3L2
LOXL4	MS4A7	COL6A2	CEL	CALCR
FAP	ITGB2	COL5A2	PNLIP	ELTD1
NAA20	LAPTM5	NID1	PNLIPRP2	CD93
ENPP2	C1QC	COL5A3	PLA2G1B	ESAM
PLCE1	CTSS	COL12A1	CPB1	ACVRL1
<hr/>				
Cluster 5	Cluster 6	Cluster 7	Cluster 8	
SCD5	GSTA2	TYROBP	ITGB7	
SORL1	GSTA1	LCP1	HLA-DQA1	
CASR	AKR1C3	SRGN	CTSS	
SYNE2	BCAT1	RGS1	FGL2	
HADH	MGST1	LAPTM5	MPEG1	
PDX1	PRSS3P2	CD53	ADORA3	
PRSS23	CPB1	FCER1G	LILRB2	
PCSK1	MUC1	ARHGDI	ACP5	
SYT13	CAP2	EV12B	FYB	
RPB4	PNLIP	ALOX5AP	LIPA	

(b) Average Expression of Top 10 DE Genes from Each Cluster Found by graph-sc



(c) Top Cell Type Matches for Each Cluster Identified by graph-sc Based on PanglaoDB Markers

Cluster	Match Type	Annotation	Score
0	Primary	Alpha cells	0.1277
	Secondary	Glutaminergic neurons	0.1000
1	Primary	No annotation	-
2	Primary	Pancreatic stellate cells	0.1379
3	Primary	Acinar cells	0.1875
4	Secondary	Peri-islet Schwann cells	0.0625
	Primary	No annotation	-
5	Primary	Parathyroid chief cells	0.1250
	Secondary	Delta cells	0.1176
6	Primary	Acinar cells	0.1458
	Secondary	Foveolar cells	0.0952
7	Primary	No annotation	-
8	Primary	No annotation	-

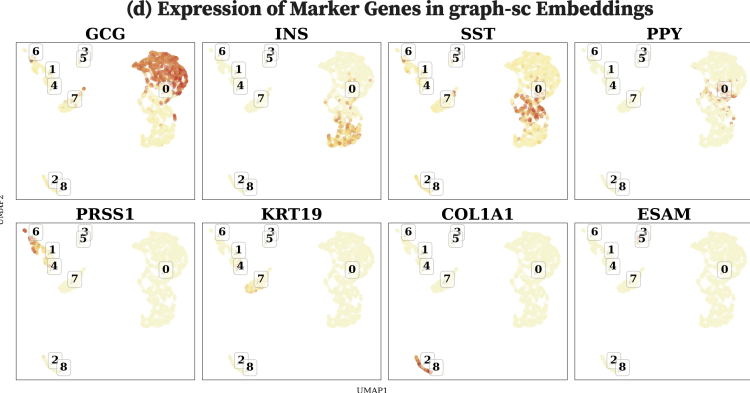


FIG. 9: Clustering Performance of graph-sc on the Human Pancreas Dataset and Cell Type Annotation Using Differentially Expressed Genes (DEGs) and Canonical Markers. (a) Top 10 DEGs per cluster identified by graph-sc. (b) Across expression of cluster-specific DEGs across clusters. Strong clustering performance is indicated by high expression of cluster-specific DEGs within their respective clusters and low expression in other clusters. Graph-sc clusters generally show moderate specificity with substantial cross-cluster overlap. (c) Cell type annotation using the PanglaoDB marker database. Four clusters (1, 4, 7, and 8) yield no annotation, indicating that their DEGs did not match known cell type markers. (d) Expression of human pancreatic canonical markers in graph-sc embeddings. UMAP visualizations show graph-sc cell embeddings, with cluster IDs assigned by K-means clustering. Overall, cell cluster separation is limited.

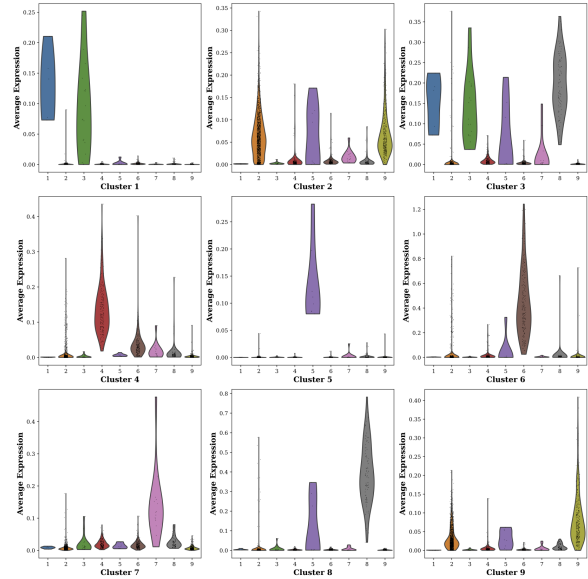
IV. CONCLUSION

In this study, we develop and analyze two hypergraph-based clustering algorithms, DIPH and CoMem-DIPH, to improve cell clustering performance on scRNA-seq data. First, the Dual-Importance Preference (DIP) Hypergraph Walk (DIPH) extends the edge-dependent vertex weight (EDVW) hypergraph random walk [44] and consistently outperforms it in our experiments.

(a) Top 10 DE Genes for Each Cluster Identified by TsImpute in the Human Pancreas Data

Cluster 1	Cluster 2	Cluster 3	Cluster 4	Cluster 5
PASK	PPP1R1A	THBS1	CFTR	CENPF
ELTD1	MAFB	EMP1	KRT19	TOP2A
PODXL	ENPP2	ITGA5	CLDN1	MKI67
CD93	KIAA1244	COL4A2	DEFB1	ASPM
EXOC3L2	CRYBA2	SPARC	SERPING1	NUSAP1
SOX18	PTPRN	COL4A1	ANXA3	CKS2
FLT1	RGS4	PPAP2B	SLC4A4	PRC1
ESAM	NEUROD1	PXDN	ONECUT2	HMMR
PLVAP	TMEM176B	ESAM	LITAF	CDK1
ACVR1L	PAX6	FLT1	ANXA4	SKA2
Cluster 6	Cluster 7	Cluster 8	Cluster 9	
PRSS3P2	CTSD	COL6A2	GAD2	
GSTA2	PMP22	COL6A1	PCSK1	
CPA2	TGFBI	COL5A1	UCHL1	
GSTA1	CTSS	COL1A2	ABCC8	
CPA1	WIFP1	COL5A2	SORL1	
IL32	HLA-DRA	LOXL2	SYT13	
PLA2G1B	FYB	PDGFRB	SCG3	
PNLIP	HCK	NID1	CASR	
BCAT1	RGS1	COL1A1	SNAP25	
ANPEP	SRGN	CDH11	PAM	

(b) Average Expression of Top 10 DE Genes from Each Cluster Found by TsImpute



(c) Top Cell Type Matches for Each Cluster Identified by TsImpute Based on PanglaoDB Markers

Cluster	Match Type	Annotation	Score
1	Primary	Parietal cells	0.0714
2	Primary	Alpha cells	0.1064
	Secondary	Retinal progenitor cells	0.0769
3	Primary	Salivary mucous cells	0.1429
	Secondary	Pancreatic stellate cells	0.0690
4	Primary	Ductal cells	0.1395
	Secondary	Cholangiocytes	0.0952
5	Primary	Gamma delta T cells	0.0758
6	Primary	Acinar cells	0.1458
	Secondary	Decidual cells	0.1000
7	Primary	No annotation	-
8	Primary	Pulmonary vascular smooth muscle cells	0.5000
	Secondary	Pancreatic stellate cells	0.1724
9	Primary	Parathyroid chief cells	0.1250
	Secondary	GABAergic neurons	0.0667

(d) Expression of Marker Genes in TsImpute Embeddings

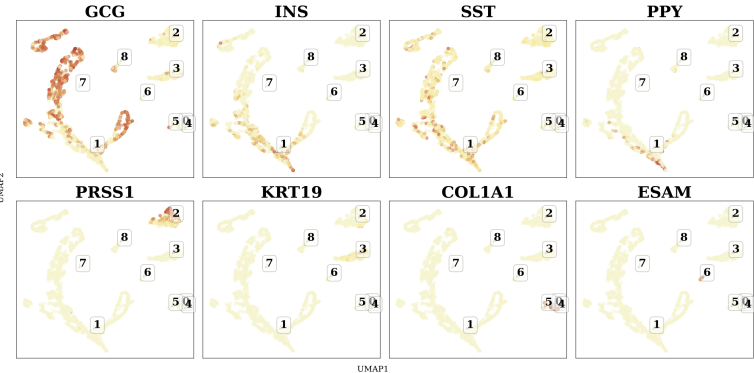


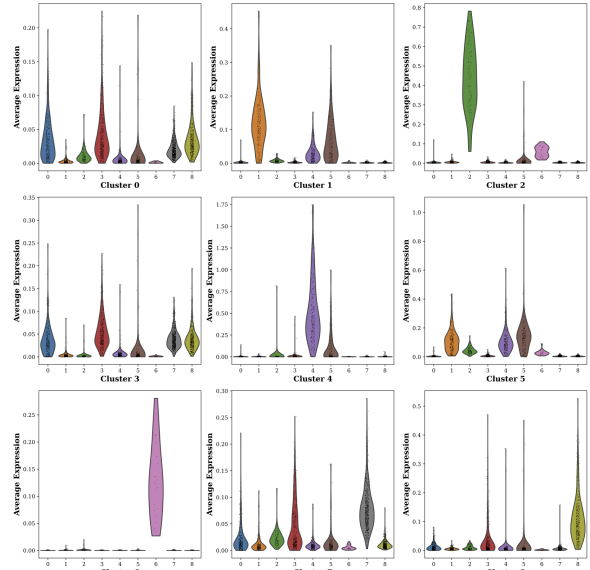
FIG. 10: Clustering Performance of tsImpute on the Human Pancreas Dataset and Cell Type Annotation Using Differentially Expressed Genes (DEGs) and Canonical Markers. (a) Top 10 DEGs per cluster identified by tsImpute combined with PCA embeddings and K-means. (b) Average expression of cluster-specific DEGs across clusters. Strong clustering performance is indicated by high expression of cluster-specific DEGs within their respective clusters and low expression in other clusters. tsImpute DEGs show high specificity in Clusters 2, 4, 5, 6, 7, 8, and 9. (c) Cell type annotation using the PanglaoDB marker database. Several annotations are biologically implausible for pancreas tissue, including parietal cells (Cluster 1), salivary mucous cells (Cluster 3), gamma delta T cells (Cluster 5), and pulmonary vascular smooth muscle cells (Cluster 8). These unexpected annotations suggest that the imputation process may introduce artifacts that confound cell type identification. (d) Expression of human pancreatic canonical markers in tsImpute combined with PCA embeddings. UMAP visualizations show tsImpute plus PCA cell embeddings, with cluster IDs assigned by K-means clustering. tsImpute improves cluster separation compared to PCA without imputation.

The key idea of DIPHW is its symmetrized treatment of importance, considering both the relative importance of edges to nodes and nodes to edges, or the importance of genes relative to cells and cells to genes, along with a preference exponent for faster clustering. Second, the CoMem and CoMem-DIPHW clustering methods incorporate a memory mechanism that considers both

(a) Top 10 DE Genes for Each Cluster Identified by CAKE in the Human Pancreas Data

Cluster 0	Cluster 1	Cluster 2	Cluster 3	Cluster 4
ABCC9	SERPING1	COL6A1	SCG3	PLA2G1B
PRG4	SLC4A4	COL1A1	SNAP25	CPB1
GAD2	CFTR	COL5A2	SEC11C	CTRBL1
KIAA1377	LITAF	COL6A2	PAM	CPA2
AQP3	ANXA4	MRC2	KIAA1244	PNLIP
PEG10	KRT19	NID1	GAD2	PRSS3P2
PCSK1	CTSH	COL12A1	AQP3	GSTA2
PAX6	ONECUT2	SPARC	PEG10	CPA1
ABCC8	TSPN8	COL4A1	NEUROD1	CTRC
NEUROD1	LAD1	TIMP1	PRG4	KLK1
Cluster 5				
TACSTD2	PLVAP	GC	INS	
KRT7	FLT1	LOXL4	HADH	
S100A11	KDR	CRYBA2	NPTX2	
SOX4	SOX18	RGS4	SYT13	
BACE2	EXOC3L2	TMEM176B	MAFA	
CLDN1	CALCR	KCTD12	SORL1	
CD44	ELTD1	FAP	PDX1	
TMSB10	CD93	NAA20	UCHL1	
SEL1L3	ESAM	ENPP2	SCD5	
SPTBN1	ACVR1	PLCE1	TGFB3	

(b) Average Expression of Top 10 DE Genes from Each Cluster Found by CAKE



(c) Top Cell Type Matches for Each Cluster Identified by CAKE Based on PanglaoDB Markers

Cluster	Match Type	Annotation	Score
0	Primary	Gamma (PP) cells	0.1034
	Secondary	Delta cells	0.0882
1	Primary	Ductal cells	0.1395
	Secondary	Ionocytes	0.0909
2	Primary	Pancreatic stellate cells	0.2069
	Secondary	Hepatic stellate cells	0.0652
3	Primary	Gamma (PP) cells	0.0690
	Secondary	GABAergic neurons	0.0667
4	Primary	Acinar cells	0.1875
5	Primary	Ductal cells	0.0698
	Secondary	Goblet cells	0.0571
6	Primary	No annotation	-
7	Primary	Alpha cells	0.1277
	Secondary	Glutaminergic neurons	0.1000
8	Primary	Beta cells	0.1373
	Secondary	Delta cells	0.0882

(d) Expression of Marker Genes in CAKE Embeddings

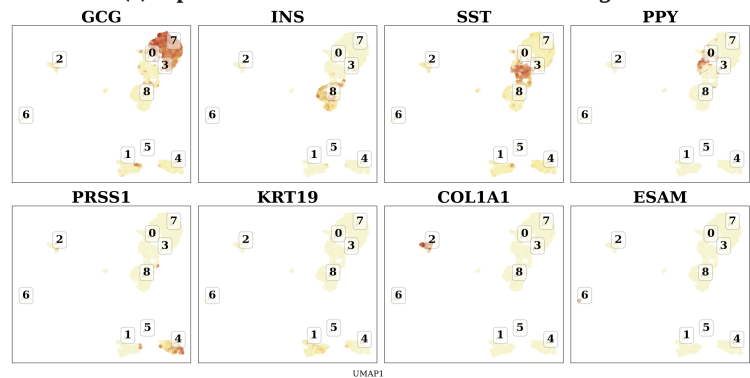


FIG. 11: Clustering Performance of CAKE on the Human Pancreas Dataset and Cell Type Annotation Using Differentially Expressed Genes (DEGs) and Canonical Markers. (a) Top 10 DEGs per cluster identified by CAKE. (b) Average expression of cluster-specific DEGs across clusters. Strong clustering performance is indicated by high expression of cluster-specific DEGs within their respective clusters and low expression in other clusters. CAKE DEGs show good cluster specificity. (c) Cell type annotation using the PanglaoDB marker database. Most CAKE clusters correspond to biologically relevant cell types: gamma/PP cells (Clusters 0 and 3), ductal cells (Clusters 1 and 5), pancreatic stellate cells (Cluster 2), acinar cells (Cluster 4), alpha cells (Cluster 7), and beta cells (Cluster 8). (d) Expression of human pancreatic canonical markers in CAKE embeddings. UMAP visualizations show CAKE cell embeddings, with cluster IDs assigned by K-means clustering. Marker genes show distinct concentration in the well-separated CAKE embeddings: GCG in Cluster 7, INS in Cluster 8, SST in Clusters 0 and 3, PRSS1 in Cluster 4, and KRT19 in Cluster 1.

the abundance counts data (conceptualized as hypergraphs) and the two co-expression networks to integrate local and global information when computing embeddings for clustering. Third, we identify and demonstrate through experiments (see Fig. 3) the issue of inflated signals in co-expression networks caused by the sparsity of scRNA-seq data, which further motivates the use of hypergraph representations. Fourth, we compare our proposed methods with 13 cell-clustering methods

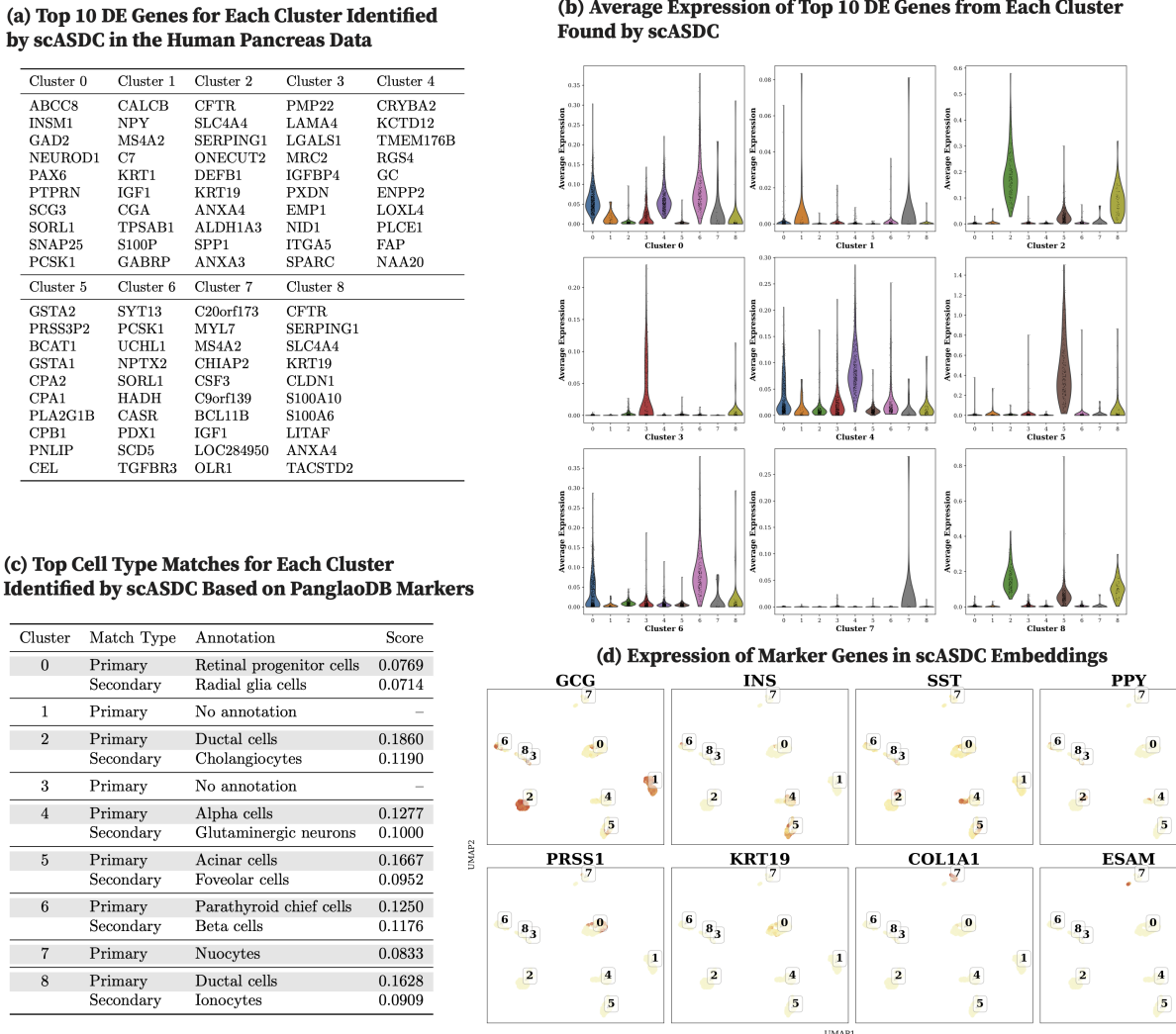


FIG. 12: Clustering Performance of scASDC on the Human Pancreas Dataset and Cell Type Annotation Using Differentially Expressed Genes (DEGs) and Canonical Markers. (a) Top 10 DEGs per cluster identified by scASDC. (b) Average expression of cluster-specific DEGs across clusters. Strong clustering performance is indicated by high expression of cluster-specific DEGs within their respective clusters and low expression in other clusters. scASDC DEGs show good cluster specificity. (c) Cell type annotation using the PanglaoDB marker database. While most clusters are matched to relevant pancreatic cell types, some are annotated with unexpected cell types, including retinal progenitor cells (Cluster 0) and nuocytes (Cluster 7). Clusters 1 and 3 received no annotation. (d) Expression of human pancreatic canonical markers in scASDC embeddings. scASDC embeddings show the best internal cohesion and separability. The marker genes show distinct concentration in the well-separated scASDC embeddings. However, the cell type annotations suggest that the embeddings may not necessarily correspond to biologically meaningful clusters.

from various categories, including community detection, embedding-based methods, and recent deep learning methods used in clustering scRNA-seq data. Our evaluation covers a broad range of modularity conditions in the data, where CoMem-DIPH and DIPH consistently show superior performance, particularly in weak modularity regimes. When clusters are harder to detect, other methods experience a much more pronounced decline in performance compared to CoMem-

DIPHW. Fifth, we test our proposed methods on four real scRNA-seq datasets and two benchmark datasets. In these experiments, CoMem-DIPHW consistently demonstrates superior performance in differentiating and classifying distinct cell types compared to the other methods. Sixth, we design a versatile simulation algorithm for scRNA-seq data that is highly customizable through many user-specified parameters. This algorithm models a wide range of expression scenarios and modular structures. Notably, it incorporates intermodular co-expressions, which mimic cell-type cross-talk observed in real biological systems.

A. Future Work

We plan to optimize the implementation of CoMem-DIPHW to reduce its memory complexity, enabling it to scale to larger datasets. We will also explore alternative methods for incorporating the memory mechanism into the hypergraph random walk. Currently, CoMem uses a simple product approach; moving beyond this could reveal more effective clustering strategies. Although our current evaluation focuses on the biological relevance of clusters through cell-type annotation using PanglaoDB markers, future application-focused studies could include Gene Ontology enrichment analysis to characterize the functions of identified clusters.

With the increasing availability of data and studies in spatial transcriptomics [88–91], extending the CoMem-DIPHW formulation for spatial transcriptomics analysis is a promising direction. While the current CoMem-DIPHW formulation focuses on cell clustering based on expression profile similarity, it could be extended to incorporate spatial proximity by replacing the cell expression similarity matrix G_V with functions that characterize joint cell similarity based on both expression profiles and spatial information.

[1] D. Szklarczyk, A. Franceschini, S. Wyder, K. Forslund, D. Heller, J. Huerta-Cepas, M. Simonovic, A. Roth, A. Santos, K. P. Tsafou, et al., *Nucleic acids research* **43**, D447 (2015).

[2] D. V. Veres, D. M. Gyurkó, B. Thaler, K. Z. Szalay, D. Fazekas, T. Korcsmáros, and P. Csermely, *Nucleic acids research* **43**, D485 (2015).

[3] A. Vazquez, A. Flammini, A. Maritan, and A. Vespignani, *Nature biotechnology* **21**, 697 (2003).

[4] M. Ashtiani, A. Salehzadeh-Yazdi, Z. Razaghi-Moghadam, H. Hennig, O. Wolkenhauer, M. Mirzaie, and M. Jafari, *BMC systems biology* **12**, 1 (2018).

- [5] I. A. Kovács, K. Luck, K. Spirohn, Y. Wang, C. Pollis, S. Schlabach, W. Bian, D.-K. Kim, N. Kishore, T. Hao, et al., *Nature communications* **10**, 1240 (2019).
- [6] C. Lei and J. Ruan, *Bioinformatics* **29**, 355 (2013).
- [7] Y. Murakami, L. P. Tripathi, P. Prathipati, and K. Mizuguchi, *Current opinion in structural biology* **44**, 134 (2017).
- [8] D. J. Coleman, P. Keane, R. Luque-Martin, P. S. Chin, H. Blair, L. Ames, S. G. Kellaway, J. Griffin, E. Holmes, S. Potluri, et al., *Cell reports* **42** (2023).
- [9] G. Muzio, L. O’Bray, and K. Borgwardt, *Briefings in bioinformatics* **22**, 1515 (2021).
- [10] S. Zickenrott, V. Angarica, B. Upadhyaya, and A. Del Sol, *Cell death & disease* **7**, e2040 (2016).
- [11] M. U. Kraemer, C.-H. Yang, B. Gutierrez, C.-H. Wu, B. Klein, D. M. Pigott, O. C.-. D. W. Group†, L. Du Plessis, N. R. Faria, R. Li, et al., *Science* **368**, 493 (2020).
- [12] M. Chinazzi, J. T. Davis, M. Ajelli, C. Gioannini, M. Litvinova, S. Merler, A. Pastore y Piontti, K. Mu, L. Rossi, K. Sun, et al., *Science* **368**, 395 (2020).
- [13] J. T. Davis, M. Chinazzi, N. Perra, K. Mu, A. Pastore y Piontti, M. Ajelli, N. E. Dean, C. Gioannini, M. Litvinova, S. Merler, et al., *Nature* **600**, 127 (2021).
- [14] P. Langfelder and S. Horvath, *BMC bioinformatics* **9**, 1 (2008).
- [15] R. Satija, J. A. Farrell, D. Gennert, A. F. Schier, and A. Regev, *Nature biotechnology* **33**, 495 (2015).
- [16] A. Butler, P. Hoffman, P. Smibert, E. Papalex, and R. Satija, *Nature biotechnology* **36**, 411 (2018).
- [17] F. A. Wolf, P. Angerer, and F. J. Theis, *Genome biology* **19**, 15 (2018).
- [18] E.-A. Horvát and K. A. Zweig, in *2012 IEEE/ACM International Conference on Advances in Social Networks Analysis and Mining* (IEEE, 2012), pp. 599–606.
- [19] E. Kuzmin, B. VanderSluis, W. Wang, G. Tan, R. Deshpande, Y. Chen, M. Usaj, A. Balint, M. Mattiazzi Usaj, J. Van Leeuwen, et al., *Science* **360**, eaao1729 (2018).
- [20] I. Yanai and T. Hashimshony, *Single Cell Methods: Sequencing and Proteomics* pp. 45–56 (2019).
- [21] E. Z. Macosko, A. Basu, R. Satija, J. Nemesh, K. Shekhar, M. Goldman, I. Tirosh, A. R. Bialas, N. Kamitaki, E. M. Martersteck, et al., *Cell* **161**, 1202 (2015).
- [22] G. X. Zheng, J. M. Terry, P. Belgrader, P. Ryvkin, Z. W. Bent, R. Wilson, S. B. Ziraldo, T. D. Wheeler, G. P. McDermott, J. Zhu, et al., *Nature communications* **8**, 14049 (2017).
- [23] S. Picelli, O. R. Faridani, Å. K. Björklund, G. Winberg, S. Sagasser, and R. Sandberg, *Nature protocols* **9**, 171 (2014).
- [24] B. Hwang, J. H. Lee, and D. Bang, *Experimental & molecular medicine* **50**, 1 (2018).

- [25] J. C. Marioni and D. Arendt, *Annual review of cell and developmental biology* **33**, 537 (2017).
- [26] H. Y. Wong, Q. Sheng, A. B. Hesterberg, S. Croessmann, B. L. Rios, K. Giri, J. Jackson, A. X. Miranda, E. Watkins, K. R. Schaffer, et al., *Nature Communications* **13**, 6036 (2022).
- [27] M. Lavoron, M. Petit, E. Weber-Delacroix, A. J. Combes, A. R. Arkal, S. Barthélémy, T. Courau, D. A. Hume, C. Combadière, M. F. Krummel, et al., *Cell Reports* **39** (2022).
- [28] M. Karaayvaz, S. Cristea, S. M. Gillespie, A. P. Patel, R. Mylvaganam, C. C. Luo, M. C. Specht, B. E. Bernstein, F. Michor, and L. W. Ellisen, *Nature communications* **9**, 3588 (2018).
- [29] E. Landhuis, *Nature* **557**, 595 (2018).
- [30] Y. A. Lyons, S. Y. Wu, W. W. Overwijk, K. A. Baggerly, and A. K. Sood, *NPJ precision oncology* **1**, 26 (2017).
- [31] J. Ermann, D. A. Rao, N. C. Teslovich, M. B. Brenner, and S. Raychaudhuri, *Nature Reviews Rheumatology* **11**, 541 (2015).
- [32] W. Chung, H. H. Eum, H.-O. Lee, K.-M. Lee, H.-B. Lee, K.-T. Kim, H. S. Ryu, S. Kim, J. E. Lee, Y. H. Park, et al., *Nature communications* **8**, 15081 (2017).
- [33] R. Jiang, T. Sun, D. Song, and J. J. Li, *Genome biology* **23**, 31 (2022).
- [34] M. Huang, J. Wang, E. Torre, H. Dueck, S. Shaffer, R. Bonasio, J. I. Murray, A. Raj, M. Li, and N. R. Zhang, *Nature methods* **15**, 539 (2018).
- [35] P. Qiu, *Embracing the dropouts in single-cell rna-seq analysis. nat. commun.* **11**, 1169 (2020).
- [36] T. H. Kim, X. Zhou, and M. Chen, *Genome biology* **21**, 196 (2020).
- [37] G. Bianconi, *Higher-order networks* (Cambridge University Press, 2021).
- [38] F. Battiston, G. Cencetti, I. Iacopini, V. Latora, M. Lucas, A. Patania, J.-G. Young, and G. Petri, *Physics reports* **874**, 1 (2020).
- [39] F. Battiston, E. Amico, A. Barrat, G. Bianconi, G. Ferraz de Arruda, B. Franceschiello, I. Iacopini, S. Kéfi, V. Latora, Y. Moreno, et al., *Nature Physics* **17**, 1093 (2021).
- [40] X. Liu, C. Song, S. Liu, M. Li, X. Zhou, and W. Zhang, *Bioinformatics* **38**, 4782 (2022).
- [41] H. Wang, K. Lin, Q. Zhang, J. Shi, X. Song, J. Wu, C. Zhao, and K. He, *Bioinformatics* **40**, btae159 (2024).
- [42] T. Gaudelot, N. Malod-Dognin, and N. Pržulj, *Bioinformatics* **34**, i944 (2018).
- [43] Y. Ma and Y. Ma, *Bioinformatics* **38**, 435 (2022).
- [44] U. Chitra and B. J. Raphael, in *Proceedings of the 36th International Conference on Machine Learning, ICML 2019, 9-15 June 2019, Long Beach, California, USA*, edited by K. Chaudhuri and

R. Salakhutdinov (PMLR, Long Beach, California, USA, 2019), vol. 97 of *Proceedings of Machine Learning Research*, pp. 1172–1181.

[45] T. Mikolov, I. Sutskever, K. Chen, G. S. Corrado, and J. Dean, Advances in neural information processing systems **26** (2013).

[46] E. Armingol, A. Officer, O. Harismendy, and N. E. Lewis, Nature Reviews Genetics **22**, 71 (2021).

[47] C. Zhang, Y. Hu, and L. Gao, Scientific Reports **13**, 15746 (2023).

[48] J. A. Zepp and E. E. Morrisey, Nature reviews Molecular cell biology **20**, 551 (2019).

[49] D. Bayik and J. D. Lathia, Nature Reviews Cancer **21**, 526 (2021).

[50] A. Lehuen, J. Diana, P. Zaccone, and A. Cooke, Nature Reviews Immunology **10**, 501 (2010).

[51] W. He, *CoMem-DIPH: Coexpression and memory-integrated dual-importance preference hypergraph walk*, <https://github.com/wanhe13/CoMem-DIPH> (2025).

[52] T. S. Andrews, V. Y. Kiselev, D. McCarthy, and M. Hemberg, Nature protocols **16**, 1 (2021).

[53] M. E. Newman, Physical Review E—Statistical, Nonlinear, and Soft Matter Physics **69**, 066133 (2004).

[54] G. Csardi and T. Nepusz, Available at igraph.org/. Accessed November **30**, 2015 (2006).

[55] V. D. Blondel, J.-L. Guillaume, R. Lambiotte, and E. Lefebvre, Journal of statistical mechanics: theory and experiment **2008**, P10008 (2008).

[56] M. Rosvall and C. T. Bergstrom, Proceedings of the national academy of sciences **105**, 1118 (2008).

[57] V. A. Traag, L. Waltman, and N. J. Van Eck, Scientific reports **9**, 1 (2019).

[58] K. Pearson, The London, Edinburgh, and Dublin Philosophical Magazine and Journal of Science **2**, 559 (1901).

[59] V. Y. Kiselev, K. Kirschner, M. T. Schaub, T. Andrews, A. Yiu, T. Chandra, K. N. Natarajan, W. Reik, M. Barahona, A. R. Green, et al., Nature methods **14**, 483 (2017).

[60] L. Van der Maaten and G. Hinton, Journal of machine learning research **9** (2008).

[61] L. McInnes, J. Healy, and J. Melville, arXiv preprint arXiv:1802.03426 (2018).

[62] A. Grover and J. Leskovec, in *Proceedings of the 22nd ACM SIGKDD international conference on Knowledge discovery and data mining* (2016), pp. 855–864.

[63] A. Grover and J. Leskovec, *node2vec: Reference implementation*, <https://github.com/aditya-grover/node2vec> (2016).

[64] SNAP Group, Stanford University, *node2vec implementation in snap*, <https://github.com/snap-stanford/snap/tree/master/examples/node2vec> (2017).

- [65] M. Ciortan and M. Defrance, *Bioinformatics* **38**, 1037 (2022).
- [66] M. Ciortan and M. Defrance, *graph-sc: Gnn-based embedding for clustering scrna-seq data*, <https://github.com/ciortanmadalina/graph-sc> (2022).
- [67] W. Zheng, W. Min, and S. Wang, *Bioinformatics* **39**, btad731 (2023).
- [68] W. Zheng, W. Min, and S. Wang, *Tsimpute: Two-step imputation for single-cell rna-seq data*, <https://github.com/ZhengWeihuaYNU/tsImpute> (2023).
- [69] J. Liu, W. Zeng, S. Kan, M. Li, and R. Zheng, *Briefings in Bioinformatics* **25**, bbad475 (2024).
- [70] J. Liu, W. Zeng, S. Kan, M. Li, and R. Zheng, *Cake: a flexible self-supervised framework for enhancing cell visualization, clustering and rare cell identification*, <https://github.com/CSUBioGroup/CAKE> (2024).
- [71] W. Min, Z. Wang, F. Zhu, T. Xu, G. Wu, and S. Wang, in *2024 IEEE International Conference on Bioinformatics and Biomedicine (BIBM)* (IEEE, 2024), pp. 1092–1097.
- [72] W. Min, Z. Wang, F. Zhu, T. Xu, G. Wu, and S. Wang, *scasdc: Attention enhanced structural deep clustering for single-cell rna-seq data*, <https://github.com/wenwenmin/scASDC> (2024).
- [73] T. Mikolov, arXiv preprint arXiv:1301.3781 (2013).
- [74] C. A. Vallejos, D. Risso, A. Scialdone, S. Dudoit, and J. C. Marioni, *Nature methods* **14**, 565 (2017).
- [75] J. G. Camp, F. Badsha, M. Florio, S. Kanton, T. Gerber, M. Wilsch-Bräuninger, E. Lewitus, A. Sykes, W. Hevers, M. Lancaster, et al., *Proceedings of the National Academy of Sciences* **112**, 15672 (2015).
- [76] M. J. Muraro, G. Dharmadhikari, D. Grün, N. Groen, T. Dielen, E. Jansen, L. Van Gurp, M. A. Engelse, F. Carlotti, E. J. De Koning, et al., *Cell systems* **3**, 385 (2016).
- [77] A. Zeisel, A. B. Muñoz-Manchado, S. Codeluppi, P. Lönnerberg, G. La Manno, A. Juréus, S. Marques, H. Munguba, L. He, C. Betsholtz, et al., *Science* **347**, 1138 (2015).
- [78] M. Baron, A. Veres, S. L. Wolock, A. L. Faust, R. Gaujoux, A. Vetere, J. H. Ryu, B. K. Wagner, S. S. Shen-Orr, A. M. Klein, et al., *Cell systems* **3**, 346 (2016).
- [79] L. Tian, X. Dong, S. Freytag, K.-A. Lê Cao, S. Su, A. JalalAbadi, D. Amann-Zalcenstein, T. S. Weber, A. Seidi, J. S. Jabbari, et al., *Nature methods* **16**, 479 (2019).
- [80] M. J. Barber, *Physical Review E—Statistical, Nonlinear, and Soft Matter Physics* **76**, 066102 (2007).
- [81] O. Franzén, L.-M. Gan, and J. L. Björkegren, *Database* **2019**, baz046 (2019).
- [82] L. Cheng, M. Xie, W. Qiao, Y. Song, Y. Zhang, Y. Geng, W. Xu, L. Wang, Z. Wang, K. Huang, et al., *Communications Biology* **4**, 1039 (2021).
- [83] M. Jozkowiak, G. Hutchings, M. Jankowski, K. Kulcenty, P. Mozdziak, B. Kempisty, R. Z. Spaczyn-

ski, and H. Piotrowska-Kempisty, *Cells* **9**, 1418 (2020).

[84] K. Tamura, J. Yu, T. Hata, M. Suenaga, K. Shindo, T. Abe, A. MacGregor-Das, M. Borges, C. L. Wolfgang, M. J. Weiss, et al., *Proceedings of the National Academy of Sciences* **115**, 4767 (2018).

[85] D. Y. Hui, *Biochimica et Biophysica Acta (BBA)-Molecular and Cell Biology of Lipids* **1864**, 784 (2019).

[86] A. V. Pinho, I. Roodman, M. Reichert, N. De Medts, L. Bouwens, A. K. Rustgi, and F. X. Real, *Gut* **60**, 958 (2011).

[87] E. Masson, J.-M. Chen, M.-P. Audrézet, D. N. Cooper, and C. Férec, *PloS one* **8**, e73522 (2013).

[88] X. Li, F. Zhu, and W. Min, *Briefings in Bioinformatics* **25**, bbae571 (2024).

[89] A. Rao, D. Barkley, G. S. França, and I. Yanai, *Nature* **596**, 211 (2021).

[90] S. K. Longo, M. G. Guo, A. L. Ji, and P. A. Khavari, *Nature Reviews Genetics* **22**, 627 (2021).

[91] V. Kleshchevnikov, A. Shmatko, E. Dann, A. Aivazidis, H. W. King, T. Li, R. Elmentait, A. Lomakin, V. Kedlian, A. Gayoso, et al., *Nature biotechnology* **40**, 661 (2022).

SUPPLEMENTARY MATERIALS

S1. Evaluating the Impact of Correlation Methods on Network-Based Clustering Performance

There are two primary strategies for handling shared zeros in cell expression profiles of scRNA-seq data during correlation computation. The first strategy, exemplified by cosine similarity, is to ignore the shared zeros. In this approach, inactive expression (zeros) does not contribute to the similarity between cells. However, our experiments indicate that this strategy leads to significantly worse clustering performance. The absence of expression in the same genes between cell pairs provides information about cellular similarity and should not be disregarded.

We evaluate how co-expression networks generated by different correlation computation methods affect the performance of various network-based clustering methods. See Table S1. Our results show that cosine similarity often produces the worst clustering results among Pearson, Spearman, and Kendall Tau.

Method	ARI				NMI			
	Pearson	Cosine	Spearman	Kendall	Pearson	Cosine	Spearman	Kendall
GreedyModularity	0.205	0.135	0.194	0.197	0.534	0.429	0.496	0.502
Louvain	0.493	0.322	0.445	0.473	0.784	0.666	0.768	0.781
Infomap	0.000	0.000	0.000	0.000	0.000	0.000	0.000	0.000
Leiden	-0.001	-0.001	-0.000	-0.000	0.062	0.040	0.082	0.073
Multilevel	0.032	0.034	0.034	0.035	0.305	0.289	0.325	0.319
Eigenvector	0.002	0.000	0.003	0.005	0.097	0.060	0.082	0.091

TABLE S1: Impact of Correlation Methods on Network-Based Clustering Performance. The table shows how different correlation measures (specifically, Pearson, Spearman, Kendall Tau, and cosine similarity) affect the performance of various network-based clustering methods. The correlation computation method that results in the worst clustering performance is marked in bold. Cosine similarity, which ignores shared zeros in cell expression profiles, often produces the worst clustering performance. These results indicate that while correlation computation methods that treat zeros the same as non-zero signals may inflate correlations, ignoring these zeros, as in cosine similarity, can lead to poorer performance.

The main implication of this experiment is that both strategies have limitations when handling sparse scRNA-seq data. Cosine similarity’s omission of shared zeros results in the poorest performance. In contrast, methods that treat all shared zeros in expression profiles as indicators of cell homogeneity (such as Pearson, Spearman, and Kendall Tau) overlook the fact that many shared

zeros arise simply from the high dimensionality of scRNA-seq data. When sequencing results from multiple cells are combined, many zero entries appear because different cells often express different sets of genes. Our results indicate that alternative approaches, such as hypergraph-based methods, offer a better solution by avoiding the need for unipartite network projections and the complexity of handling zeros in correlation calculations.

S2. Computational and Memory Complexities of DIPHW and CoMem-DIPHW

a. DIPHW. The computational cost of each element $P(u \rightarrow v)$ in the $|V| \times |V|$ node-to-node transition probability matrix is $O(|E|)$ when the intermediate matrices for the node-to-edge and edge-to-node transition probabilities $P_{E|V}(e|u)$ and $P_{V|E}(v|e)$ are precomputed. The construction of the entire $|V| \times |V|$ node-to-node transition probability matrix involves computing these probabilities for all node pairs, resulting in an overall time complexity of $O(|V|^2 \cdot |E|)$.

For efficient computation, the $|V| \times |V|$ node-to-node transition probability matrix $P_{V|V}$ in matrix form is given by:

$$P_{V|V} = D_{E|V}^{-1} W_{E|V} D_{V|E}^{-1} W_{V|E}$$

The theoretical complexity remains $O(|E|^2 \cdot |V| + |E| \cdot |V|^2)$. However, the matrix representation utilizes parallel computation and is significantly faster, making it more suitable for large datasets.

DIPHW's memory complexity is $O(|E| \cdot |V|)$ for the node-to-edge and edge-to-node transition probability matrices.

b. CoMem-DIPHW. The computational complexity of CoMem-DIPHW is $O(|E|^2 \cdot |V|^2)$. For each pair of nodes, the memory-incorporated transition traverses all possible edges that could have reached the first node and all possible edges that could then connect the first node with the second node.

CoMem-DIPHW's memory complexity is $O(|E|^2 \cdot |V| + |E| \cdot |V|^2)$ for the memory-incorporated node-to-edge and edge-to-node transition probability matrices.

S3. Bipartite representation

We choose the hypergraph conceptualization over the bipartite representation for consistency, as the DIPHW algorithm we introduce is an extension of the edge-dependent vertex weight hypergraph random walk (EDVW) [44]. DIPHW extends the EDVW hypergraph random walk by

incorporating a vertex-dependent edge selection probability and a preference exponent to accelerate clustering.

A bipartite conceptualization could also be applied to our proposed methods by interpreting the incidence matrix $\mathbf{I}_{\mathcal{H}}$ of the hypergraph \mathcal{H} as a bipartite graph. In this representation, the two sets of nodes are the set of cells V and the set of genes E . Each gene is connected to all cells in which it is actively expressed, with weights corresponding to the expression level. This alternative representation enables the use of bipartite graph algorithms. For example, we use Barber's bipartite modularity [80] to assess how the clustering performance of different algorithms varies with the modularity of the underlying scRNA-seq dataset.

S4. Quantitative Evaluation of Clustering Quality on Tissue Datasets

The quantitative evaluations in Tables S2 and S3 offer complementary perspectives on clustering performance for tissue scRNA-seq datasets. The evaluation in the learned embedding space (Table S2) reflects the geometric separability and compactness of the clusters produced by each method, while the evaluation of the preprocessed expression data (Table S3) assesses whether the same cluster assignments capture the structure of the preprocessed gene expression data used as input to the embedding methods. In the embedding space, graph-sc and scASDC achieve strong geometric separation and cohesion across datasets. However, they show reduced clustering performance when evaluated on the preprocessed data. This aligns with the results in Fig. 12, where scASDC produces embeddings with strong cluster separation and cohesion, but some identified DEGs correspond to biologically implausible cell types. In particular, PCA performs best in the preprocessed data evaluation. This is consistent with the findings of Ciortan et al. [65], where PCA outperformed many state-of-the-art methods, including graph-sc, when evaluated by the Silhouette score and the Calinski-Harabasz index on real and simulated datasets.

S5. Additional Results for Clustering Performance Across Modularity Levels

Figures S1 and S2 show additional results on the impact of module size and module count on ARI clustering performance. Figures S3 and S4 show the impact of module size and module count on NMI clustering performance. Figures S5 and S6 show the impact of module size and module count on ACC clustering performance. Figures S7 and S8 show the impact of module size and

Method	Human Brain				Human Pancreas				Mouse Brain				Mouse Pancreas			
	SC	CH	DB	CV	SC	CH	DB	CV	SC	CH	DB	CV	SC	CH	DB	CV
scASDC	0.421 244.710 <u>0.975</u> 2.373	0.763 <u>705.099</u> 0.844 0.560	0.549 <u>0.821</u>	0.816 <u>5230.004</u> 0.640 1.845	0.874 <u>2843.512</u> 0.462 <u>0.563</u>											
graph-sc	<u>0.352</u> 705.099 0.844 0.560	<u>0.529</u> 4164.981 <u>0.584</u> 0.816	0.418 2431.617 0.982 0.905	0.394 <u>976.784</u> <u>0.768</u> 0.495												
CoMem_DIPH	0.285 224.443 1.207 1.287	0.384 1048.921 1.119 1.058	0.396 1222.851 0.936 1.403	0.274 313.957 1.183 1.677												
CoMem	0.265 199.820 1.285 1.922	0.474 1447.208 0.852 3.575	0.455 1432.727 0.817 <u>1.086</u>	0.291 287.810 1.179 4.768												
tsImpute	<u>0.263</u> <u>703.410</u> 1.163 8.200	0.457 715.814 0.789 5.051	0.409 867.564 1.095 8.499	<u>0.424</u> 666.677 0.902 10.673												
PCA	0.258 236.768 1.412 6.802	0.294 542.832 1.270 89.515	0.229 512.127 1.652 83.396	0.107 120.386 1.804 125.705												
CAKE	0.156 164.736 1.679 2.849	0.417 3999.076 0.794 1.944	<u>0.461</u> 12194.111 <u>0.800</u> 2.684	0.237 373.750 1.391 1.825												
node2vec	0.133 172.629 2.118 2.307	0.409 1405.125 1.034 1.359	0.332 1108.268 1.188 27.464	0.198 265.955 1.467 1.014												
DIPH	0.122 110.724 2.138 <u>0.903</u>	0.204 480.360 1.328 1.060	0.127 264.797 2.444 5.145	0.055 35.369 3.380 3.147												
EDVW	0.109 97.634 2.315 1.720	0.152 402.944 2.039 6.156	0.126 246.265 2.616 5.840	0.060 40.552 3.482 5.804												

TABLE S2: Clustering Quality Evaluated in the Learned Embedding Space on Tissue scRNA-seq Datasets. Clustering performance is assessed using the Silhouette score (SC), Calinski–Harabasz index (CH), Davies–Bouldin index (DB), and Coefficient of Variation (CV) on the learned embeddings produced by each method. Higher values indicate better performance for the Silhouette score and Calinski–Harabasz index, while lower values indicate better performance for the Davies–Bouldin index and Coefficient of Variation. This evaluation reflects the geometric separability and cohesion of clusters in the embedding space. The best values within each dataset/evaluation measure column are highlighted in bold, and the second-best values are underlined.

Method	Human Brain				Human Pancreas				Mouse Brain				Mouse Pancreas			
	SC	CH	DB	CV	SC	CH	DB	CV	SC	CH	DB	CV	SC	CH	DB	CV
CoMem	0.027 17.529 <u>4.654</u> 3.951	0.071 230.969 2.048 4.559	0.041 173.331 <u>2.838</u> 7.603	-0.002 37.954 4.182 5.064												
CoMem_DIPH	<u>0.027</u> <u>17.529</u> 4.575 <u>3.951</u>	0.021 235.958 2.364 4.834	0.018 169.640 3.363 7.795	0.002 <u>40.049</u> 3.891 5.008												
PCA	0.025 19.080 4.991 4.012	0.276 <u>395.673</u> 1.461 <u>4.012</u>	0.087 <u>183.428</u> 2.829 6.995	<u>0.016</u> 46.001 3.051 4.699												
tsImpute	0.009 12.901 7.122 3.958	<u>0.114</u> 171.384 2.715 3.734	-0.005 67.857 6.082 <u>6.721</u>	-0.025 22.239 6.907 5.127												
graph-sc	0.008 10.692 6.286 4.043	0.042 201.025 2.218 4.137	0.047 127.852 5.446 6.905	0.052 28.514 <u>3.696</u> <u>4.749</u>												
node2vec	0.007 15.731 8.386 4.010	0.060 <u>259.873</u> <u>2.019</u> 4.609	0.040 <u>174.822</u> 3.240 7.726	-0.001 37.939 4.459 5.027												
DIPH	0.006 14.937 7.794 4.018	0.015 195.839 3.152 4.328	0.012 153.568 4.081 7.782	-0.006 36.516 5.353 5.115												
EDVW	0.002 13.243 8.843 4.042	-0.075 177.732 7.734 4.956	0.034 172.331 3.403 7.805	-0.001 39.774 4.790 4.991												
scASDC	-0.009 7.670 7.899 3.947	-0.128 139.358 3.605 4.655	<u>0.070</u> 166.681 3.032 7.177	-0.027 26.217 6.188 5.148												
CAKE	-0.012 7.713 8.723 4.002	-0.025 184.071 3.063 4.444	0.068 75.122 6.077 5.624	0.006 33.657 6.005 5.042												

TABLE S3: Clustering Quality Evaluated on Preprocessed Expression Data for Tissue scRNA-seq Datasets. Using the same cluster assignments as in Supplementary Table S2, we evaluate cluster quality on the preprocessed gene expression data used as input to each embedding method. We measure cluster quality using the Silhouette score (SC), Calinski–Harabasz index (CH), Davies–Bouldin index (DB), and Coefficient of Variation (CV). Higher values indicate better performance for SC and CH, while lower values indicate better performance for DB and CV. This evaluation assesses whether the cluster assignments by each method capture meaningful structure in the input gene expression data. The best values within each dataset/evaluation measure column are highlighted in bold, and the second-best values are underlined.

module count on AMI clustering performance. Figures S9 and S10 show the impact of module size and module count on F1 clustering performance. Finally, Fig. S11 shows a visualization of modularity in our imulated scRNA-seq Data.

Impact of Module Size on Clustering Performance by ARI

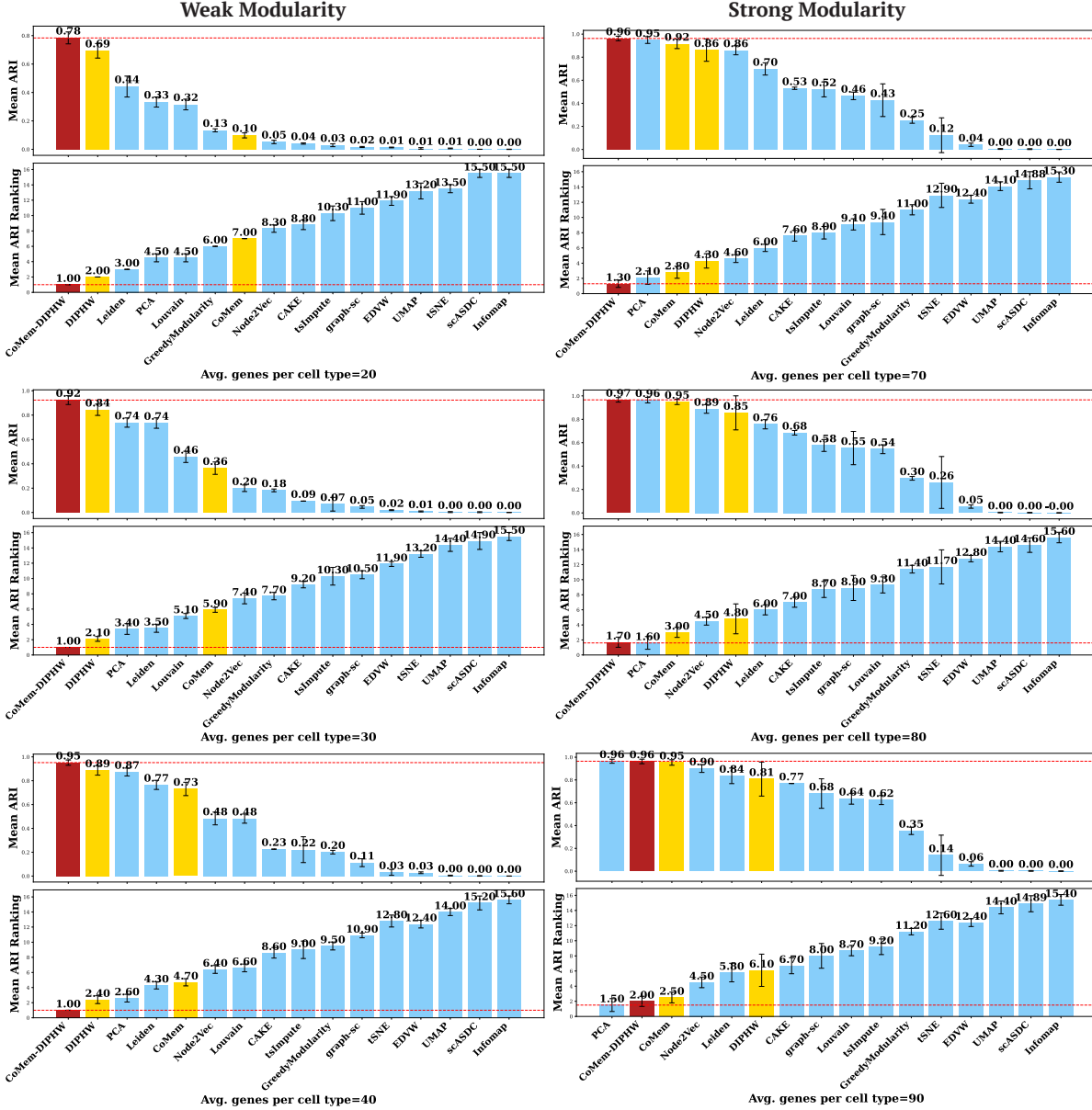


FIG. S1: Clustering Performance Comparison by ARI Across Varying Module Sizes. Simulated scRNA-seq data were used for this evaluation. Here, we present the complementary results across intermediate parameter settings, which show consistent patterns: our proposed methods (highlighted in red and yellow) consistently ranked first by ARI in all scenarios, with a stronger advantage when data modularity is weak, i.e., when the average number of co-expressed genes per module is small. Each experiment was repeated 10 times per parameter setting, with error bars representing the 95% confidence interval. Red dashed lines indicate the highest ARI values or best ARI rankings. K-means was used to cluster the output of all embedding-based methods that do not directly assign cluster membership.

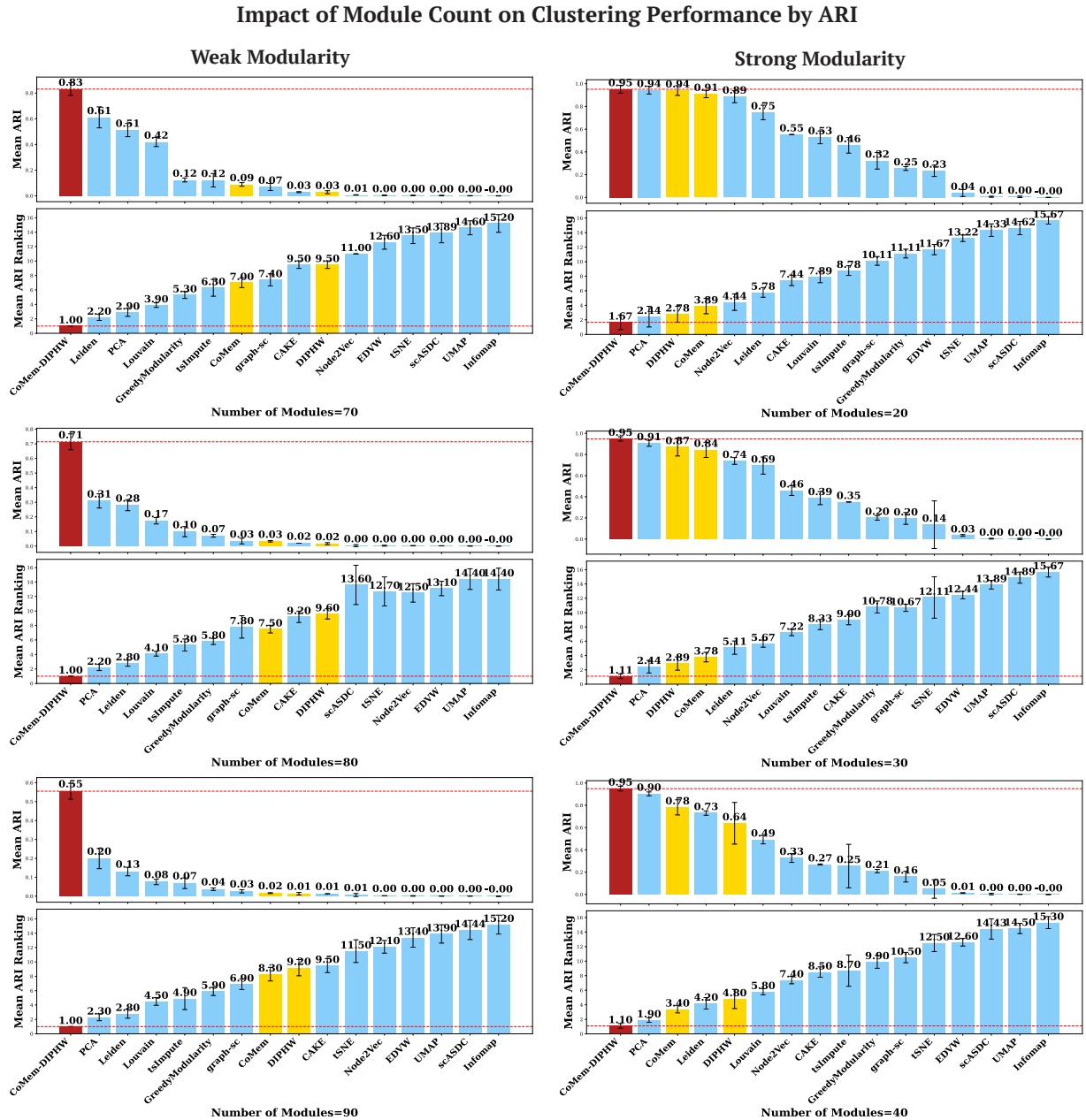


FIG. S2: Clustering Performance Comparison by ARI Across Varying Module Counts. Simulated scRNA-seq data were used for this evaluation. Here, we present the complementary results across intermediate parameter settings, which show consistent patterns: our proposed methods (highlighted in red and yellow) consistently ranked first by ARI in all scenarios, with a stronger advantage when data modularity is weak, i.e., when the number of embedded modules in the simulated scRNA-seq data is greater. Each experiment was repeated 10 times per parameter setting, with error bars representing the 95% confidence interval. Red dashed lines indicate the highest ARI values or best ARI rankings. K-means was used to cluster the output of all embedding-based methods that do not directly assign cluster membership.

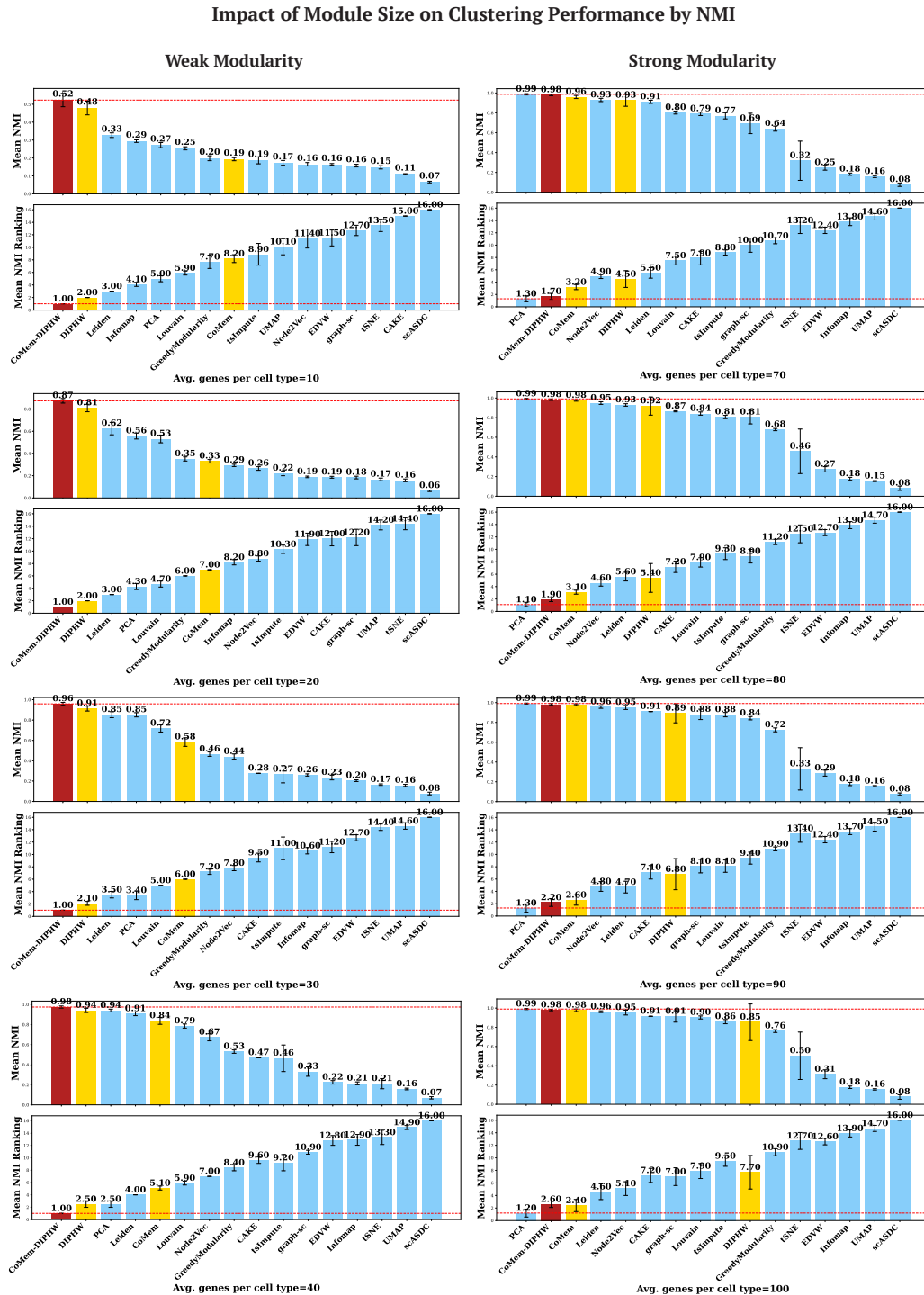


FIG. S3: Clustering Performance Comparison by NMI Across Varying Module Sizes. Simulated scRNA-seq data were used for this evaluation. The NMI results support the same conclusion: when modularity is weak (i.e., when the average number of co-expressed genes per module is small), the advantage of our proposed methods (highlighted in red and yellow) is more pronounced. Each experiment was repeated 10 times per parameter setting, with error bars representing the 95% confidence interval. Red dashed lines indicate the highest NMI values or best NMI rankings. K-means was used to cluster the output of all embedding-based methods that do not directly assign cluster membership.

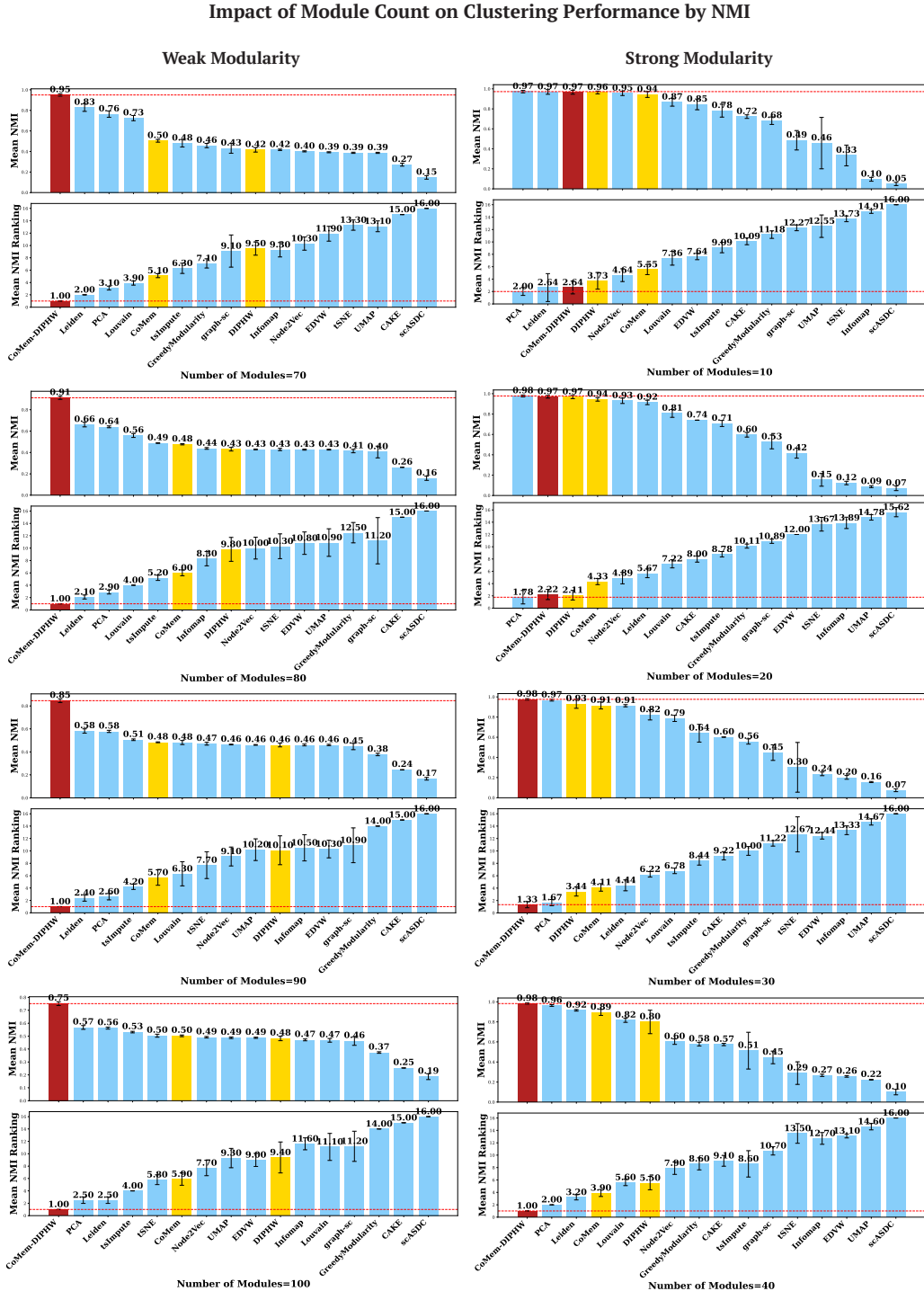


FIG. S4: Clustering Performance Comparison by NMI Across Varying Module Counts. Simulated scRNA-seq data were used for this evaluation. The results by NMI support the same conclusion: when modularity is weak (i.e., when the number of modules is greater), the advantage of our proposed methods (highlighted in red and yellow) is more pronounced. Each experiment was repeated 10 times per parameter setting, with error bars representing the 95% confidence interval. Red dashed lines indicate the highest NMI values or best NMI rankings. K-means was used to cluster the output of all embedding-based methods that do not directly assign cluster membership.

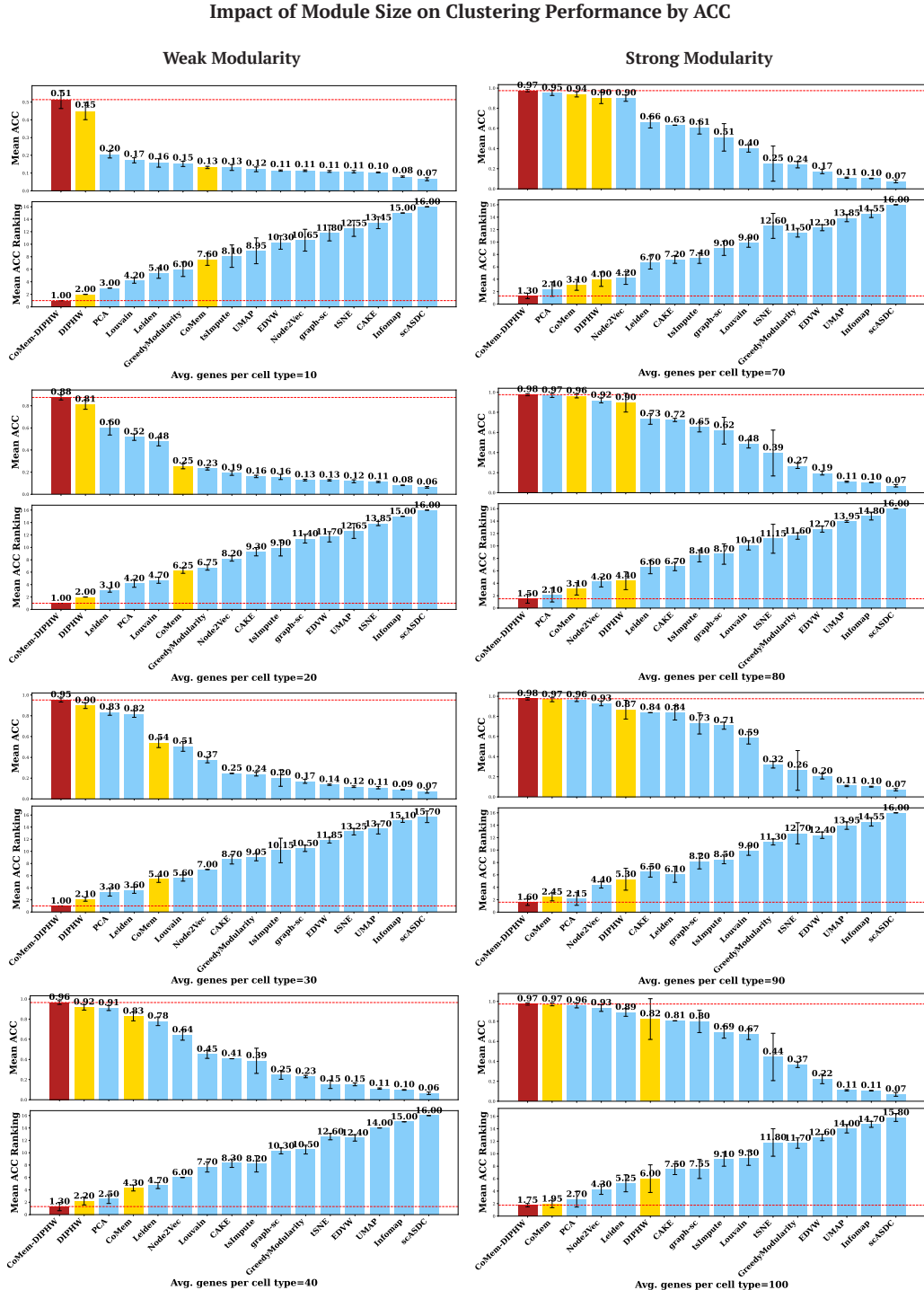


FIG. S5: Clustering Performance Comparison by ACC Across Varying Module Sizes. Simulated scRNA-seq data were used for this evaluation. The ACC results support the same conclusion: when modularity is weak (i.e., when the average number of co-expressed genes per module is small), the advantage of our proposed methods (highlighted in red and yellow) is more pronounced. Each experiment was repeated 10 times per parameter setting, with error bars representing the 95% confidence interval. Red dashed lines indicate the highest ACC values or best ACC rankings. K-means was used to cluster the output of all embedding-based methods that do not directly assign cluster membership.

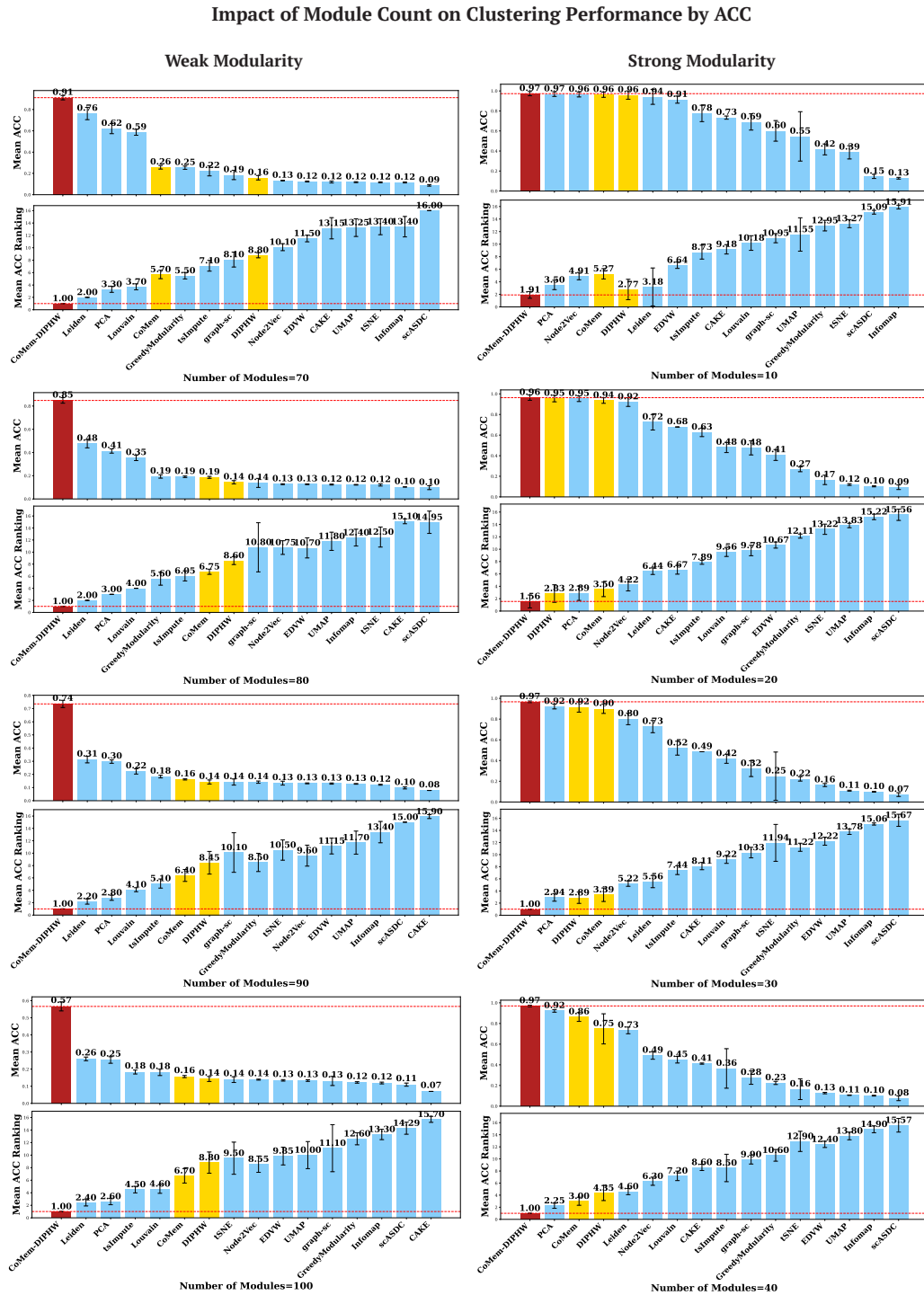


FIG. S6: Clustering Performance Comparison by ACC Across Varying Module Counts. Simulated scRNA-seq data were used for this evaluation. The results by ACC support the same conclusion: when modularity is weak (i.e., when the number of modules is greater), the advantage of our proposed methods (highlighted in red and yellow) is more pronounced. Each experiment was repeated 10 times per parameter setting, with error bars representing the 95% confidence interval. Red dashed lines indicate the highest ACC values or best ACC rankings. K-means was used to cluster the output of all embedding-based methods that do not directly assign cluster membership.

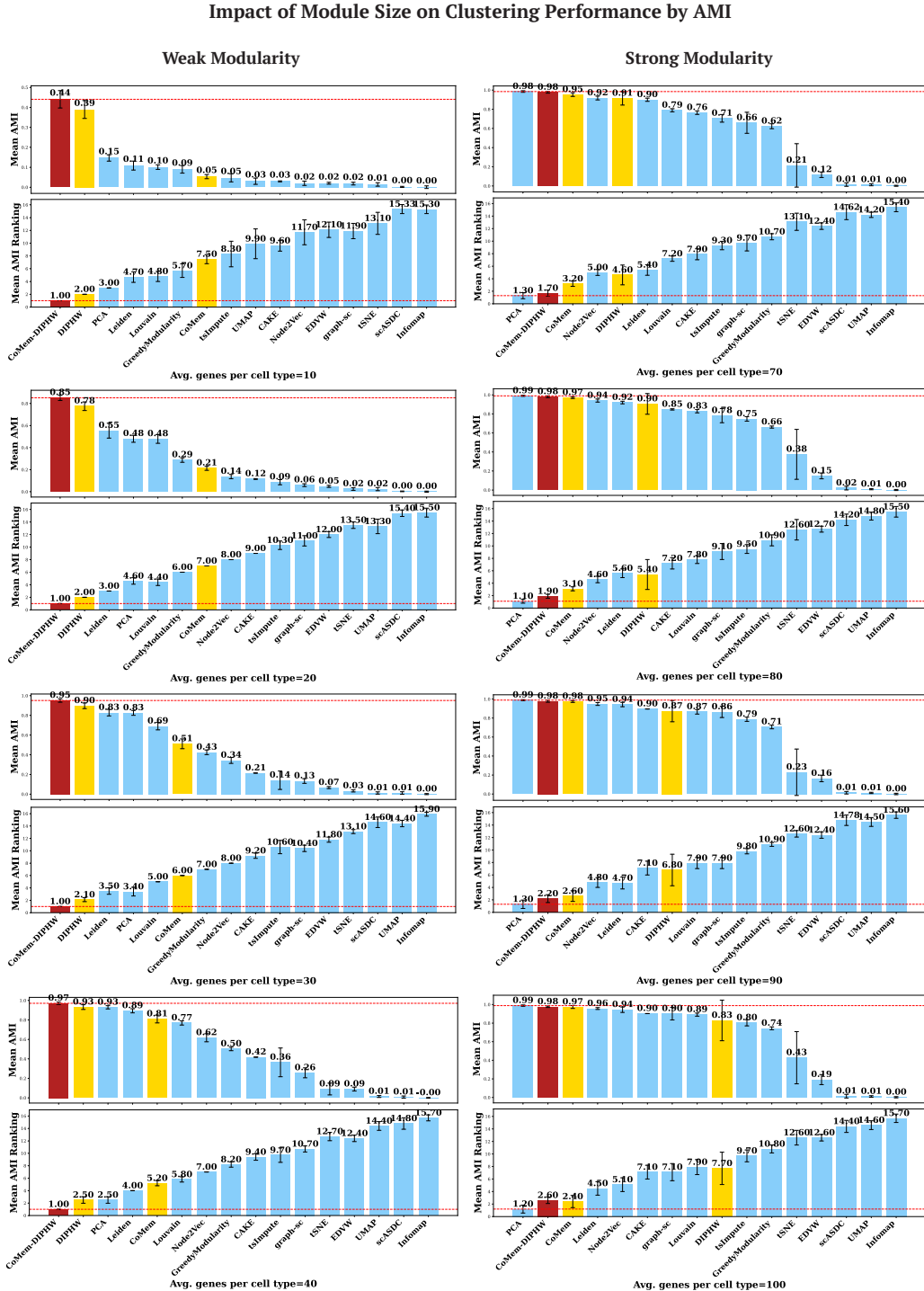


FIG. S7: Clustering Performance Comparison by AMI Across Varying Module Sizes. Simulated scRNA-seq data were used for this evaluation. The AMI results support the same conclusion: when modularity is weak (i.e., when the average number of co-expressed genes per module is small), the advantage of our proposed methods (highlighted in red and yellow) is more pronounced. Each experiment was repeated 10 times per parameter setting, with error bars representing the 95% confidence interval. Red dashed lines indicate the highest AMI values or best AMI rankings. K-means was used to cluster the output of all embedding-based methods that do not directly assign cluster membership.

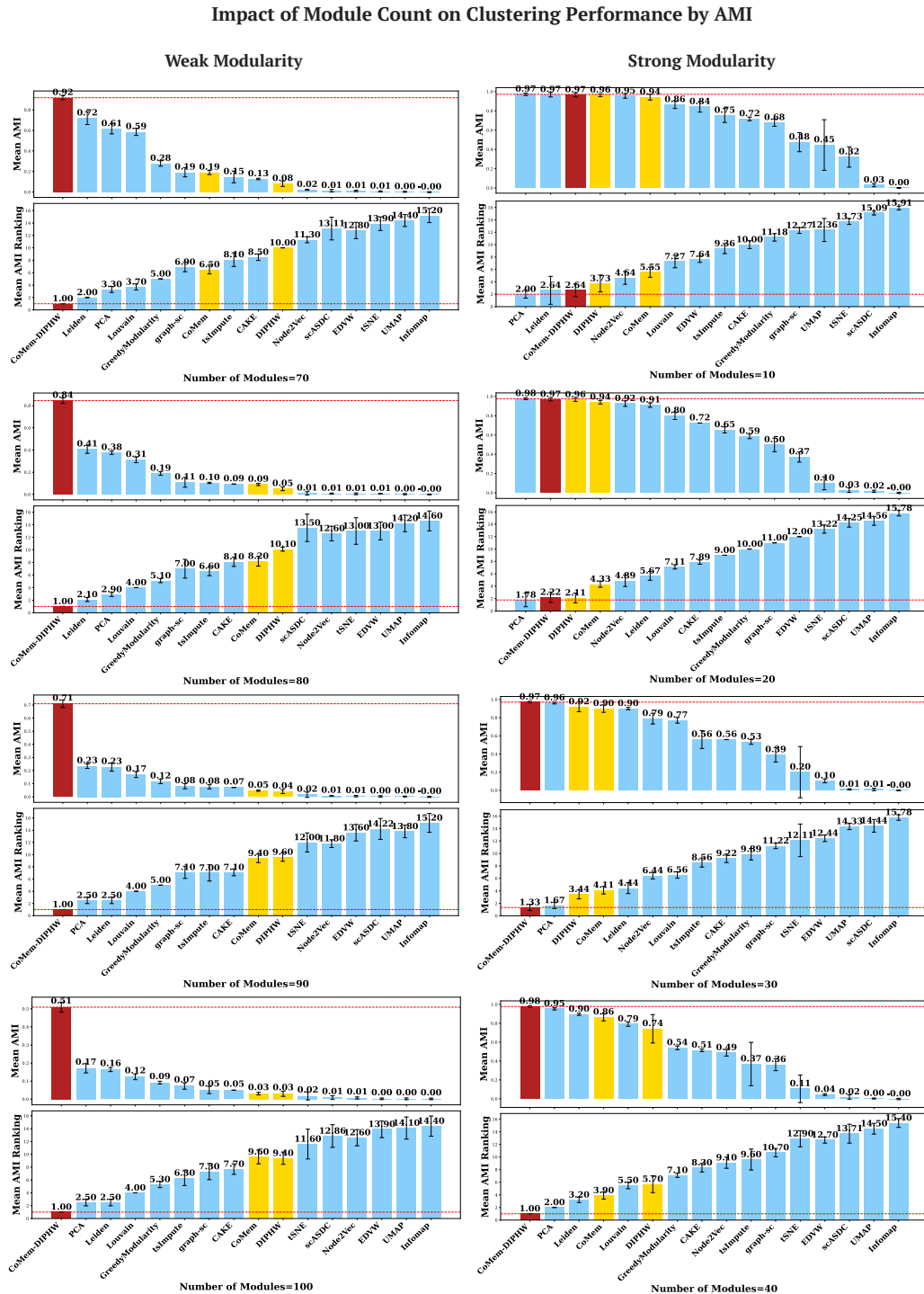


FIG. S8: Clustering Performance Comparison by AMI Across Varying Module Counts. Simulated scRNA-seq data were used for this evaluation. The results by AMI support the same conclusion: when modularity is weak (i.e., when the number of modules is greater), the advantage of our proposed methods (highlighted in red and yellow) is more pronounced. Each experiment was repeated 10 times per parameter setting, with error bars representing the 95% confidence interval. Red dashed lines indicate the highest AMI values or best AMI rankings. K-means was used to cluster the output of all embedding-based methods that do not directly assign cluster membership.

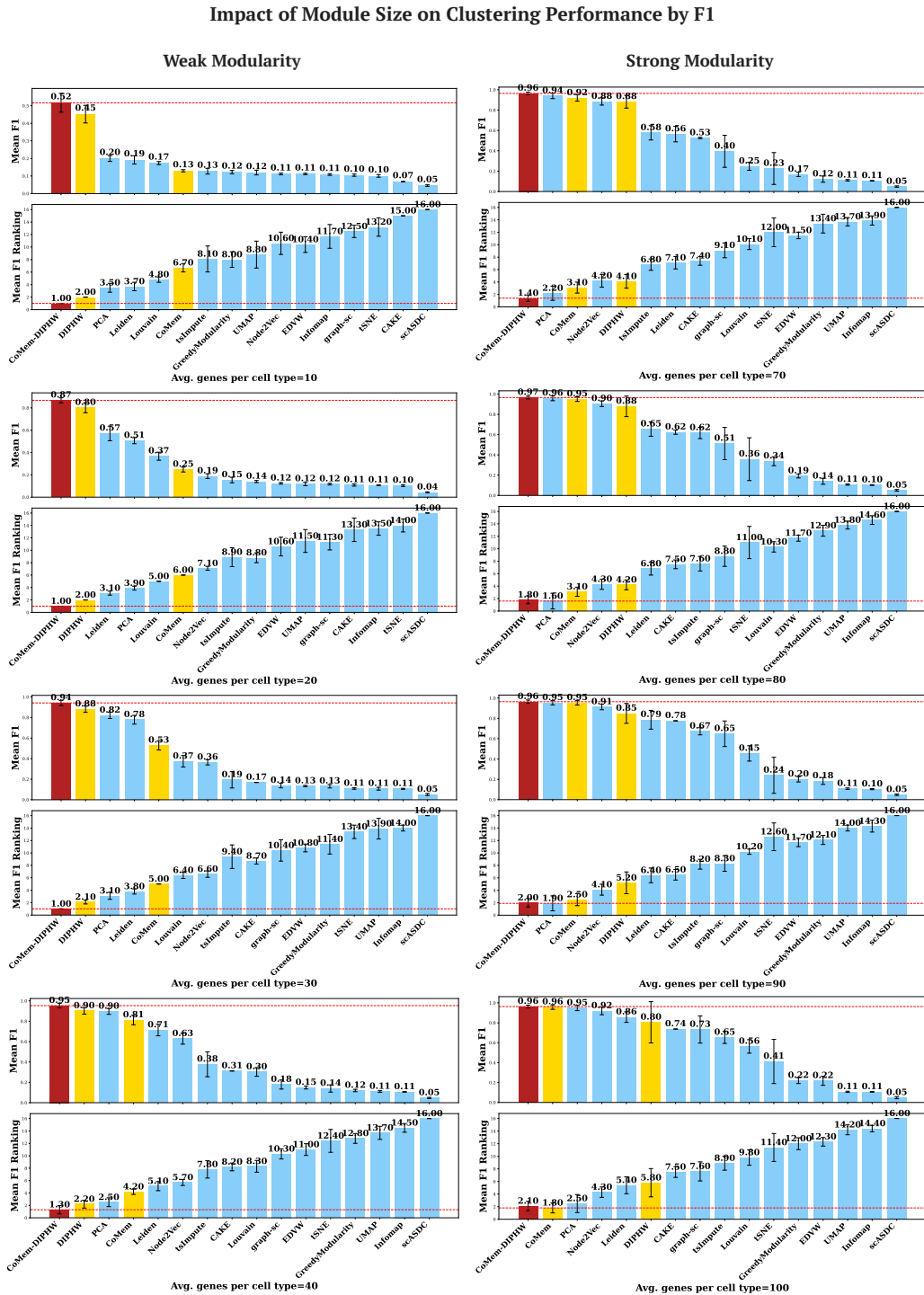


FIG. S9: Clustering Performance Comparison by F1 Across Varying Module Sizes. Simulated scRNA-seq data were used for this evaluation. The F1 results support the same conclusion: when modularity is weak (i.e., when the average number of co-expressed genes per module is small), the advantage of our proposed methods (highlighted in red and yellow) is more pronounced. Each experiment was repeated 10 times per parameter setting, with error bars representing the 95% confidence interval. Red dashed lines indicate the highest F1 values or best F1 rankings. K-means was used to cluster the output of all embedding-based methods that do not directly assign cluster membership.

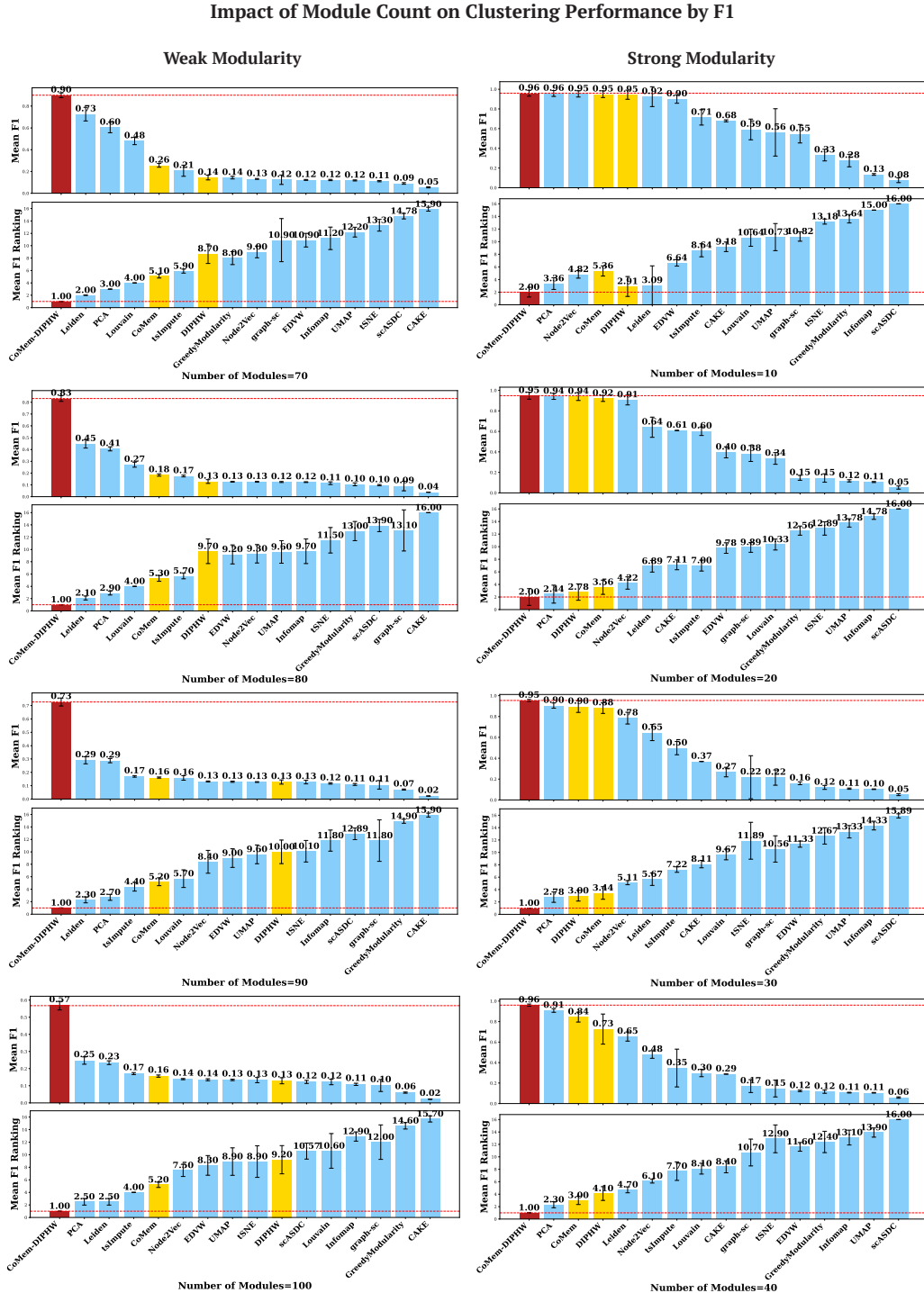


FIG. S10: Clustering Performance Comparison by F1 Across Varying Module Counts. Simulated scRNA-seq data were used for this evaluation. The results by F1 support the same conclusion: when modularity is weak (i.e., when the number of modules is greater), the advantage of our proposed methods (highlighted in red and yellow) is more pronounced. Each experiment was repeated 10 times per parameter setting, with error bars representing the 95% confidence interval. Red dashed lines indicate the highest F1 values or best F1 rankings. K-means was used to cluster the output of all embedding-based methods that do not directly assign cluster membership.

Visual Demonstrations of the Impact of Coexpressed Genes and Embedded Modules on Data Modularity

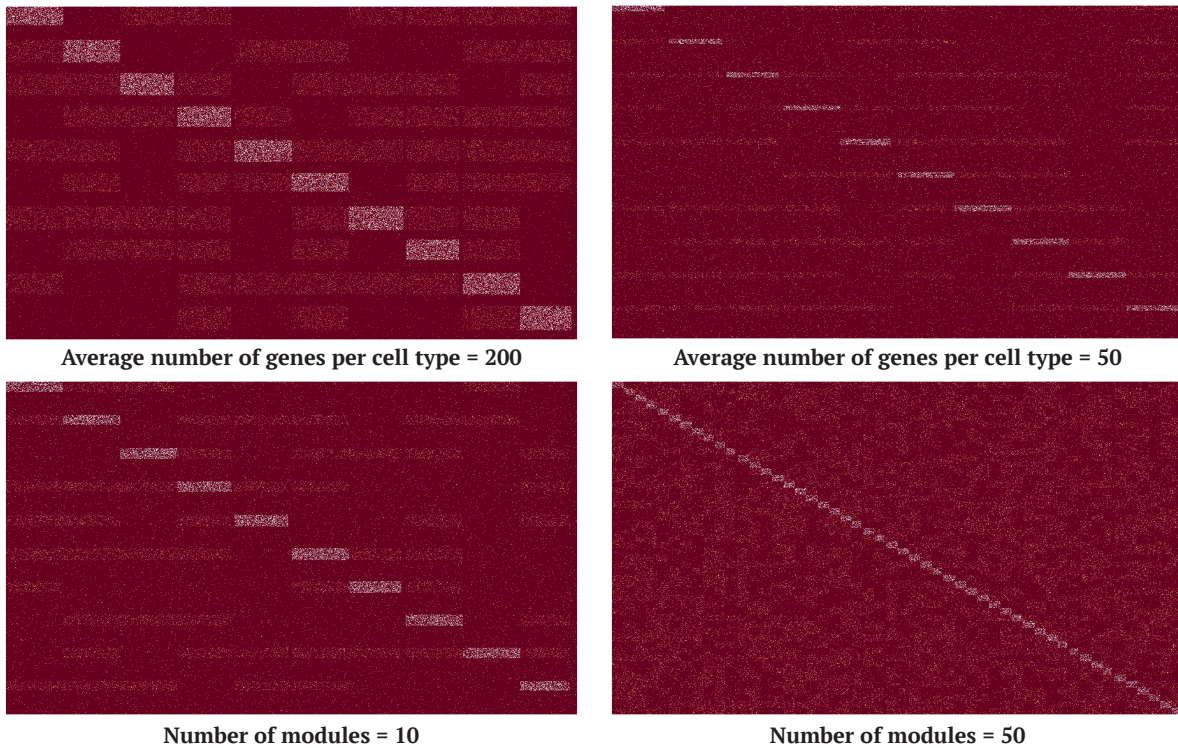


FIG. S11: Visualization of Modularity in Simulated scRNA-seq Data. Modularity increases with a higher average number of co-expressed genes per cell type and fewer modules. The number of modules models the number of cell types in the simulated data.

S6. Results for the Human Brain Dataset

Figures S12, S13, S14, S15, S16, and S17 show the results on the human brain dataset for CoMem-DIPHW, PCA, graph-sc, tsImpute, CAKE, and scASDC, respectively.

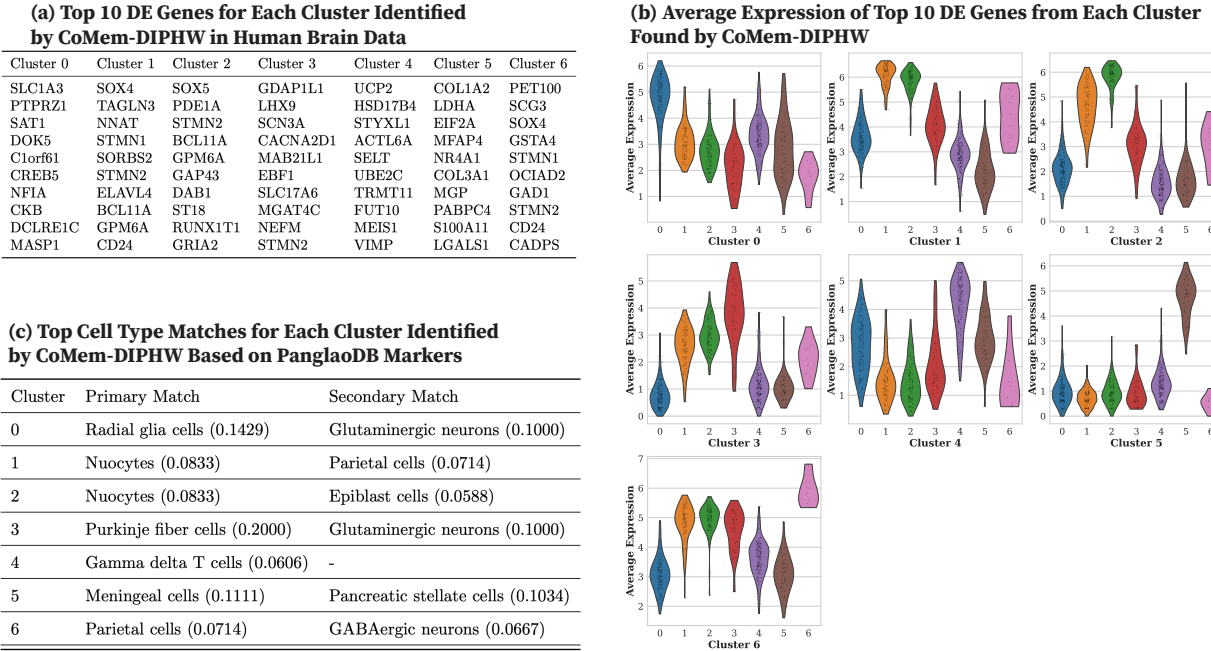


FIG. S12: Clustering Performance of CoMem-DIPH on the Human Brain Dataset and Cell Type Annotation using DEGs and Canonical Markers. (a) Top 10 DEGs identified for each cluster by CoMem-DIPH. (b) Across-cluster average expression of cluster-specific DEGs. Violin plots show the distribution of average expression levels of these DEGs across all clusters. Strong clustering performance is indicated by high expression of cluster-specific DEGs within their respective clusters and low expression in other clusters. (c) Cell type annotation using the PanglaoDB marker database. Cell types are determined by the overlap between each cluster's DEGs and cell type-specific markers in the PanglaoDB database, with match scores computed based on the proportion of matched markers.

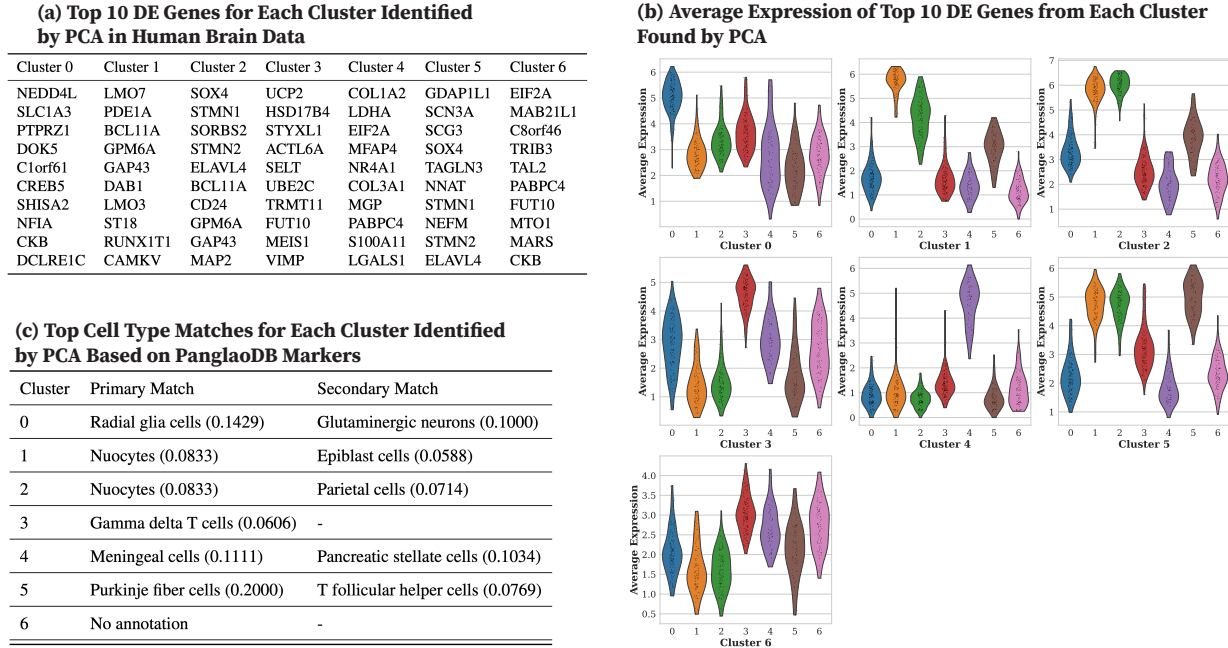
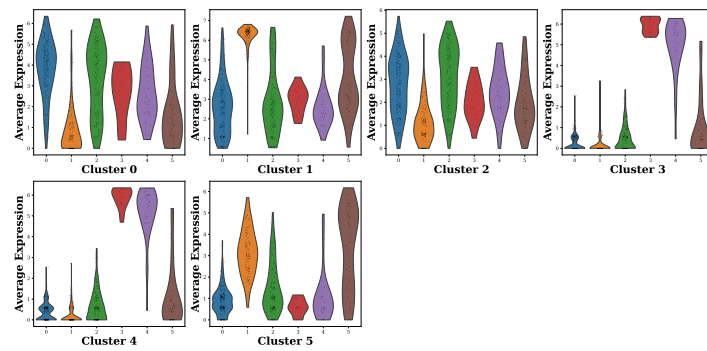


FIG. S13: Clustering Performance of PCA on the Human Brain Dataset and Cell Type Annotation using DEGs and Canonical Markers. (a) Top 10 DEGs identified for each cluster by PCA. (b) Across-cluster average expression of cluster-specific DEGs. Violin plots show the distribution of average expression levels of these DEGs across all clusters. Strong clustering performance is indicated by high expression of cluster-specific DEGs within their respective clusters and low expression in other clusters. (c) Cell type annotation using the PanglaoDB marker database. Cell types are determined by the overlap between each cluster's DEGs and cell type-specific markers in the PanglaoDB database, with match scores computed based on the proportion of matched markers.

(a) Top 10 DE Genes for Each Cluster Identified by graph-sc in Human Brain Data

Cluster 0	Cluster 1	Cluster 2	Cluster 3	Cluster 4	Cluster 5
PAX6	NEUROD6	VIMP	COL1A2	DCN	SCN2A
HMGB2	RTN1	FLRT3	DCN	LUM	SCN3A
CDK1	STMN2	CCNB1	LGALS1	COL1A2	RALYL
SLC1A3	NFIB	UBE2C	COL3A1	COL3A1	GRIA2
CREB5	MYT1L	TXNRD1	LUM	S100A11	ANK3
KNTC1	BCL11A	MAPK10	POSTN	MFAP4	THSD7A
TOP2A	BCL11B	FSIP2	S100A11	LGALS1	CDH13
UBE2C	NFIA	TOP2A	MGP	POSTN	HMP19
CCNB1	SOX4	OSGEP	MFAP4	SELM	ANK2
DOK5	RUNX1T1	FUT10	COL21A1	MGP	SYN3

(b) Average Expression of Top 10 DE Genes from Each Cluster Found by graph-sc



(c) Top Cell Type Matches for Each Cluster Identified by graph-sc Based on PanglaoDB Markers

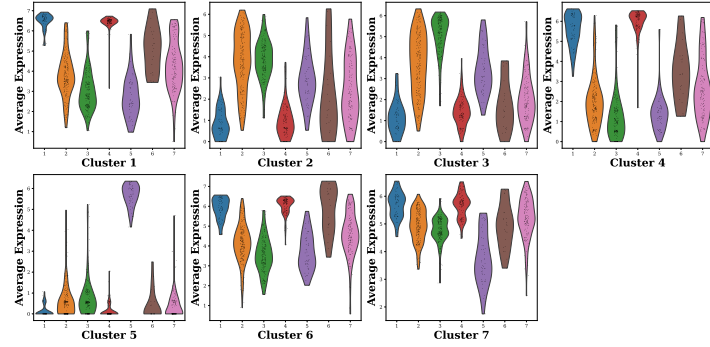
Cluster	Match Type	Annotation	Score
0	Primary	Radial glia cells	0.1429
	Secondary	Retinal progenitor cells	0.0769
1	Primary	Nuocytes	0.0833
	Secondary	Epiblast cells	0.0588
2	Primary	No annotation	—
3	Primary	Meningeal cells	0.1111
	Secondary	Pancreatic stellate cells	0.1034
4	Primary	Meningeal cells	0.1111
	Secondary	Pancreatic stellate cells	0.1034
5	Primary	No annotation	—

FIG. S14: Clustering Performance of graph-sc on the Human Brain Dataset and Cell Type Annotation using DEGs and Canonical Markers. (a) Top 10 DEGs identified for each cluster by graph-sc. (b) Across-cluster average expression of cluster-specific DEGs. Violin plots show the distribution of average expression levels of these DEGs across all clusters. Strong clustering performance is indicated by high expression of cluster-specific DEGs within their respective clusters and low expression in other clusters. (c) Cell type annotation using the PanglaoDB marker database. Cell types are determined by the overlap between each cluster's DEGs and cell type-specific markers in the PanglaoDB database, with match scores computed based on the proportion of matched markers. Two of the graph-sc clusters had less than 5 cells, one was excluded from the expression plots in (b), and both failed to map to known cell types in (c).

(a) Top 10 DE Genes for Each Cluster Identified by TsImpute in Human Brain Data

Cluster 1	Cluster 2	Cluster 3	Cluster 4	Cluster 5	Cluster 6	Cluster 7
NFIB	HMGEB2	UBE2C	NEUROD6	COL3A1	SOX4	CKB
SOX4	PAX6	CDK1	RTN1	COL1A2	BCL11A	SOX4
STMN1	SLC1A3	CCNB1	GAP43	DCN	MAP2	STMN1
STMN2	CREB5	TOP2A	BCL11A	LUM	KIDINS220	SPAG9
NEUROD6	KNTC1	C1orf31	BCL11B	SI00A11	NFIB	MAP2
GPM6A	IFI44L	UCP2	STMN2	LGALS1	AKAP9	C1orf61
NFIA	TOP2A	HMGB2	MYT1L	MFAP4	C1orf61	UBB
MAP2	CDK1	KNTC1	NFIB	POSTN	ANK3	SCN2A
RTN1	DOK5	TXNRD1	SLC24A2	SELM	ANK2	AKAP9
MYT1L	SAT1	SELT	SLA	MGP	RUNX1T1	NNAT

(b) Average Expression of Top 10 DE Genes from Each Cluster Found by TsImpute



(c) Top Cell Type Matches for Each Cluster Identified by TsImpute Based on PanglaoDB Markers

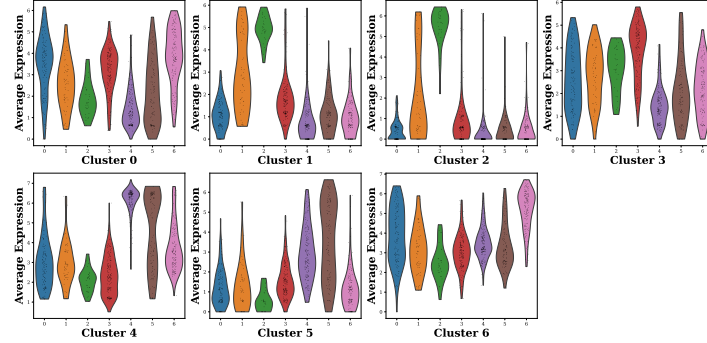
Cluster	Match Type	Annotation	Score
1	Primary	No annotation	—
2	Primary	Radial glia cells	0.1429
	Secondary	Retinal progenitor cells	0.0769
3	Primary	Gamma delta T cells	0.0606
4	Primary	Nuocytes	0.0833
	Secondary	Epiblast cells	0.0588
5	Primary	Meningeal cells	0.1111
	Secondary	Pancreatic stellate cells	0.1034
6	Primary	Epiblast cells	0.0588
7	Primary	Meningeal cells	0.0556

FIG. S15: Clustering Performance of tsImpute on the Human Brain Dataset and Cell Type Annotation using DEGs and Canonical Markers. (a) Top 10 DEGs identified for each cluster by tsImpute. (b) Across-cluster average expression of cluster-specific DEGs. Violin plots show the distribution of average expression levels of these DEGs across all clusters. Strong clustering performance is indicated by high expression of cluster-specific DEGs within their respective clusters and low expression in other clusters. (c) Cell type annotation using the PanglaoDB marker database. Cell types are determined by the overlap between each cluster's DEGs and cell type-specific markers in the PanglaoDB database, with match scores computed based on the proportion of matched markers.

(a) Top 10 DE Genes for Each Cluster Identified by CAKE in Human Brain Data

Cluster 0	Cluster 1	Cluster 2	Cluster 3	Cluster 4	Cluster 5	Cluster 6
HMGB2	SELM	LUM	C11orf31	NEUROD6	FGF12	PAX6
CKB	HERPUD1	COL3A1	VIMP	STMN2	LMO3	Clorf61
CREB5	DCN	S100A11	UBE2C	MYTIL	ST18	PHLDA1
PAX6	LUM	DCN	MEIS1	RTN1	LMO7	CREB5
SLC1A3	VIMP	COL1A2	CCNB1	SOX4	MEF2C	SLC1A3
CCNB1	S100A11	MFAP4	RCHY1	NFIB	GRIA2	UBB
RNF157	IL11RA	POSTN	CDK1	GAP43	GDAP1	DOK5
UBE2C	COL1A2	LGALS1	MBD1	NFIA	GRIK2	CKB
DOK5	COL3A1	SELM	SELT	STMN1	SCG3	NFIA
IFI44L	PTPRM	COL21A1	NME6	BCL11B	ELMOD1	MEIS2

(b) Average Expression of Top 10 DE Genes from Each Cluster Found by CAKE



(c) Top Cell Type Matches for Each Cluster Identified by CAKE Based on PanglaoDB Markers

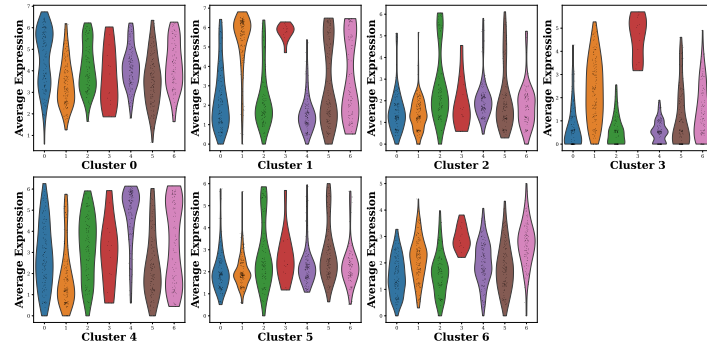
Cluster	Match Type	Annotation	Score
0	Primary	Radial glia cells	0.1429
	Secondary	Retinal progenitor cells	0.0769
1	Primary	Meningeal cells	0.1111
	Secondary	Pancreatic stellate cells	0.0690
2	Primary	Meningeal cells	0.1111
	Secondary	Pancreatic stellate cells	0.0690
3	Primary	No annotation	—
4	Primary	Nuocytes	0.0833
5	Primary	No annotation	—
6	Primary	Radial glia cells	0.1429
	Secondary	Glutaminergic neurons	0.1000

FIG. S16: Clustering Performance of CAKE on the Human Brain Dataset and Cell Type Annotation using DEGs and Canonical Markers. (a) Top 10 DEGs identified for each cluster by CAKE. (b) Across-cluster average expression of cluster-specific DEGs. Violin plots show the distribution of average expression levels of these DEGs across all clusters. Strong clustering performance is indicated by high expression of cluster-specific DEGs within their respective clusters and low expression in other clusters. (c) Cell type annotation using the PanglaoDB marker database. Cell types are determined by the overlap between each cluster's DEGs and cell type-specific markers in the PanglaoDB database, with match scores computed based on the proportion of matched markers.

(a) Top 10 DE Genes for Each Cluster Identified by scASDC in Human Brain Data

Cluster 0	Cluster 1	Cluster 2	Cluster 3	Cluster 4	Cluster 5	Cluster 6
Clorf61	GAP43	LUM	CAMKV	UBE2C	PABPC4	EIF2B4
CKB	MYT1L	COL3A1	SYN3	CDK1	UBB	BBS2
PAX6	RTN1	DCN	NOLA4	CNCNB1	AKAP9	SLC1A3
HMGB2	GRIA2	LGALS1	FGF12	TOP2A	PLXNA2	BSCL2
CREB5	STMN2	MFAP4	CAMTA2	HMBG2	MFAP4	PPFIA2
SLC1A3	NRXN1	CACYBP	SNAP91	KNTC1	COL3A1	ZSCAN26
SPAG9	NEUROD6	KBTBD2	HMP19	UCP2	HERPUD1	CTTNBP2
PHLDA1	GPM6A	S100A11	SCN2A	C11orf31	LUM	MIOS
UBB	KIDINS220	MAGED2	PHACTR3	TXNRD1	DCN	TTLL7
MEIS2	RUNX1T1	FLRT3	CALB2	ACTL6A	S100A11	ALPK1

(b) Average Expression of Top 10 DE Genes from Each Cluster Found by scASDC



(c) Top Cell Type Matches for Each Cluster Identified by scASDC Based on PanglaoDB Markers

Cluster	Match Type	Annotation	Score
0	Primary	Radial glia cells	0.1429
	Secondary	Glutaminergic neurons	0.1000
1	Primary	No annotation	—
2	Primary	Meningeal cells	0.1111
3	Primary	Retinal progenitor cells	0.0769
4	Primary	Gamma delta T cells	0.0606
5	Primary	Meningeal cells	0.1111
6	Primary	Radial glia cells	0.0714

FIG. S17: Clustering Performance of scASDC on the Human Brain Dataset and Cell Type Annotation using DEGs and Canonical Markers. (a) Top 10 DEGs identified for each cluster by scASDC. (b) Across-cluster average expression of cluster-specific DEGs. Violin plots show the distribution of average expression levels of these DEGs across all clusters. Strong clustering performance is indicated by high expression of cluster-specific DEGs within their respective clusters and low expression in other clusters. (c) Cell type annotation using the PanglaoDB marker database. Cell types are determined by the overlap between each cluster's DEGs and cell type-specific markers in the PanglaoDB database, with match scores computed based on the proportion of matched markers.

S7. Results for the Mouse Pancreas and the Mouse Brain Datasets

Figures S18, S19, S20, S21, S22, and S23 show the results on the mouse pancreas dataset for CoMem-DIPH, PCA, graph-sc, tsImpute, CAKE, and scASDC, respectively.

Figures S24, S25, S26, S27, S28, and S29 show the results on the mouse brain dataset for CoMem-DIPH, PCA, graph-sc, tsImpute, CAKE, and scASDC, respectively.

(a) Top 10 DE Genes for Each Cluster Identified by CoMem-DIPH in Mouse Pancreas Data

Cluster 0	Cluster 1	Cluster 2	Cluster 3	Cluster 4	Cluster 5	Cluster 6
Hspa1b	Sparc	B2m	Ttr	Pdyn	Pecam1	Krt8
Hspa1a	Serph1	Cd74	Gpx3	Hmox1	Egfl7	Krt18
Dnajb1	Cald1	Tmsb4x	Vgf	Vgf	Col4a2	Krt19
Hspb1	Msn	Coro1a	Irx1	Ubr4	Cdh5	Ahnak
Krt8	Col4a1	Ctss	Rbp4	Zranb2	Flt1	Anxa2
Krt18	Col4a2	H2-Eb1	Mafb	Psap	Sparc	Prdx1
Fth1	Vim	Cytip	Spp1	Nr4a2	B2m	Anxa3
Fosb	Ier3	H2-Aa	Id3	Ftl1	Plvap	Ezr
Ddit4	Gm13889	Sh3bgrl3	Serpingle	Ctsb	Ctla2a	S100a6
Gem	Anxa2	Srgn	Id1	Adgrl1	Col4a1	Clu
Cluster 7	Cluster 8	Cluster 9	Cluster 10	Cluster 11	Cluster 12	
Rbp4	Ttr	Spp1	Hmox1	Hspa1b	Rbp4	
Cd24a	Psap	Ttr	Ctsb	Hspa1a	Gpx3	
Hhex	Pdyn	Cldn4	Krt18	Pdyn	Tspan8	
Clu	Zranb2	Adgrl1	Psap	Dnajb1	Serpingle	
Arg1	Satb1	Gpx3	Krt8	Zranb2	Clu	
Tspan8	Slc35b4	Hmox1	Ftl1	Ubr4	Arg1	
Gpx3	Tnfrsf9	Slc35b4	Cldn4	Psap	Trp53i11	
Mest	Vgf	Satb1	Ctrb1	Rspo4	Cldn4	
Igfbp7	Sbk1	Lrig2	Rspo4	Th	Krt18	
Cpa2	Them4	Trim9	Derl3	Adgrl1	Pigr	

(c) Top Cell Type Matches for Each Cluster Identified by CoMem-DIPH in Based on PanglaoDB Markers

Cluster	Match Type	Annotation	Score
0	Primary	Merkel cells	0.1333
	Secondary	Hepatoblasts	0.1176
1	Primary	Myofibroblasts	0.1111
	Secondary	Glomus cells	0.1071
2	Primary	No annotation	-
	Secondary	Alpha cells	0.0652
3	Primary	Ductal cells	0.0500
	Secondary	Red pulp macrophages	0.0833
4	Primary	Dopaminergic neurons	0.0500
	Secondary	Pancreatic stellate cells	0.0690
5	Primary	Stromal cells	0.0606
	Secondary	Merkel cells	0.1333
6	Primary	Hepatoblasts	0.1176
	Secondary	Nuocytes	0.0833
7	Primary	Delta cells	0.0625
	Secondary	No annotation	-
8	Primary	Red pulp macrophages	0.0833
	Secondary	Juxtaglomerular cells	0.1429
9	Primary	Adrenergic neurons	0.1250
	Secondary	Ductal cells	0.1000
10	Primary	Nuocytes	0.0833
	Secondary	Heptoblasts	0.1176
11	Primary	Merkel cells	0.1333
	Secondary	Juxtaglomerular cells	0.1429
12	Primary	Adrenergic neurons	0.1250
	Secondary	Heptoblasts	0.1176

(b) Average Expression of Top 10 DE Genes from Each Cluster Found by CoMem-DIPH

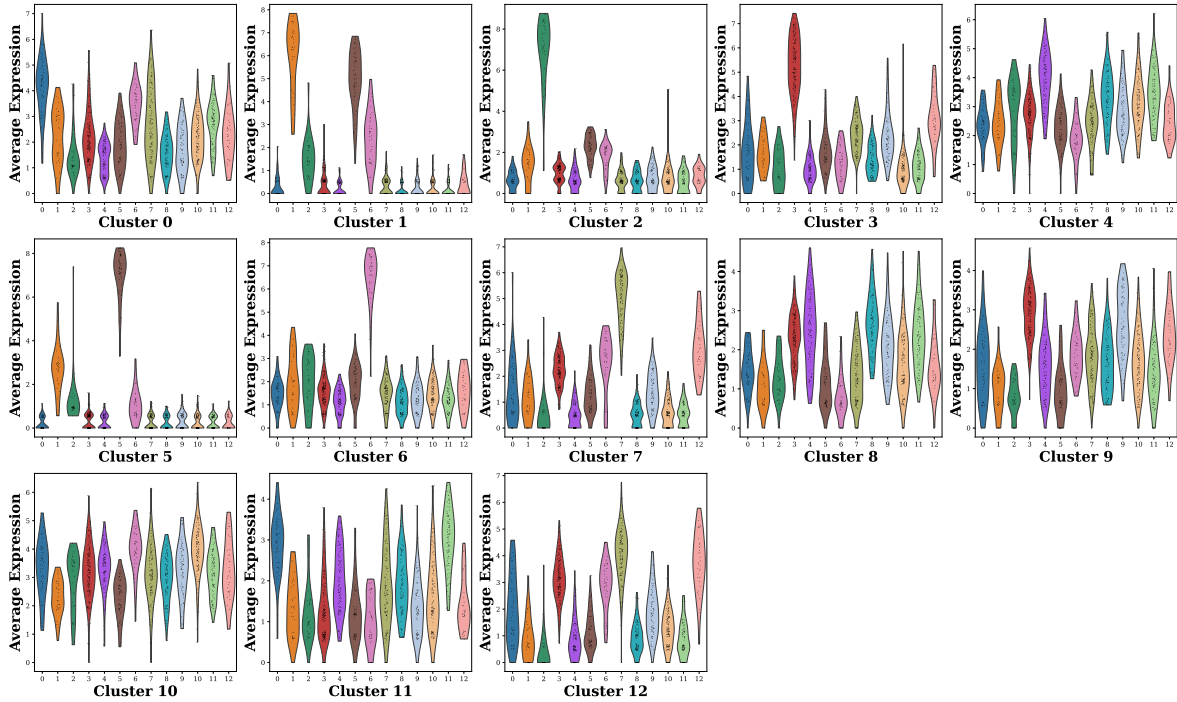


FIG. S18: Clustering Performance of CoMem-DIPH on the Mouse Pancreas Dataset and Cell Type Annotation using DEGs and Canonical Markers. (a) Top 10 DEGs identified for each cluster by CoMem-DIPH. (b) Across-cluster average expression of cluster-specific DEGs. Violin plots show the distribution of average expression levels of these DEGs across all clusters. Strong clustering performance is indicated by high expression of cluster-specific DEGs within their respective clusters and low expression in other clusters. (c) Cell type annotation using the PanglaoDB marker database. Cell types are determined by the overlap between each cluster's DEGs and cell type-specific markers in the PanglaoDB database, with match scores computed based on the proportion of matched markers.

(a) Top 10 DE Genes for Each Cluster Identified by PCA in Mouse Pancreas Data

Cluster 0	Cluster 1	Cluster 2	Cluster 3	Cluster 4	Cluster 5	Cluster 6
Hmox1	Sparc	Ttr	Krt8	Rbp4	Hmox1	Pecam1
Corola	Serpinh1	Gpx3	Clu	Cd24a	Zranb2	Egfl7
Cytip	Cald1	Vgf	Krt18	Hhex	Vgf	Cdh5
Cd74	Msn	Mafb	Krt19	Clu	Pdyn	Col4a2
Ptprc	Vim	Rbp4	S100a6	Arg1	Ftl1	Flt1
Ctrb1	Col4a1	Irx1	Anxa2	Tspan8	Actn1	Sparc
Rac2	Col4a2	Id1	Anxa3	Gpx3	Rspo4	Plvap
Cela1	Smnt	Spp1	Prdx1	Mest	Ctsb	B2m
Stk17b	Csrp1	Tmsb4x	Ahnak	Igfbp7	Nr4a2	Ctla2a
Cd52	Anxa2	Id3	Nfib	Cpa2	Il6st	Msn
Cluster 7	Cluster 8	Cluster 9	Cluster 10	Cluster 11	Cluster 12	
H2-Eb1	Ttr	Cldn4	Hmox1	Hspa1b	Gpx3	
Pla2g7	Pdyn	Adgrl1	Pdyn	Hspa1a	Spp1	
Psap	Vgf	Psap	Zranb2	Dnajb1	Tspan8	
Ctss	Amy1	Krt8	Gclc	Krt8	Ttr	
Fth1	Zranb2	Slc35b4	Ftl1	Rspo4	Rbp4	
H2-Aa	Satb1	Krt18	Psap	Krt18	Hspb1	
Ftl1	Psap	Th	Ctsb	Psap	Hspa1b	
Cd74	Ubr4	Sptbn4	Pde4b	Nr4a1	Krt18	
H2-Ab1	Slc39a14	Lyvel	Slc35b4	Ddit4	Serpingle	
Apoe	Il6st	Msln	Rspo4	Derl3	Clu	

(c) Top Cell Type Matches for Each Cluster Identified by PCA Based on PanglaoDB Markers

Cluster	Match Type	Annotation	Score
0	Primary	Red pulp macrophages	0.0833
	Secondary	Langerhans cells	0.0667
1	Primary	Myofibroblasts	0.1111
	Secondary	Glomus cells	0.1071
2	Primary	Alpha cells	0.0652
	Secondary	Merkel cells	0.1333
3	Primary	Dopaminergic neurons	0.0500
	Secondary	Hepatoblasts	0.1176
4	Primary	Nuocytes	0.0833
	Secondary	Delta cells	0.0625
5	Primary	Red pulp macrophages	0.0833
	Secondary	No annotation	-
6	Primary	No annotation	-
	Secondary	No annotation	-
7	Primary	No annotation	-
	Secondary	No annotation	-
8	Primary	No annotation	-
	Secondary	Merkel cells	0.1333
9	Primary	Juxtaglomerular cells	0.1429
	Secondary	Red pulp macrophages	0.0833
10	Primary	Merkel cells	0.1333
	Secondary	Hepatoblasts	0.1176
11	Primary	Ductal cells	0.0750
	Secondary	Merkel cells	0.0667

(b) Average Expression of Top 10 DE Genes from Each Cluster Found by PCA

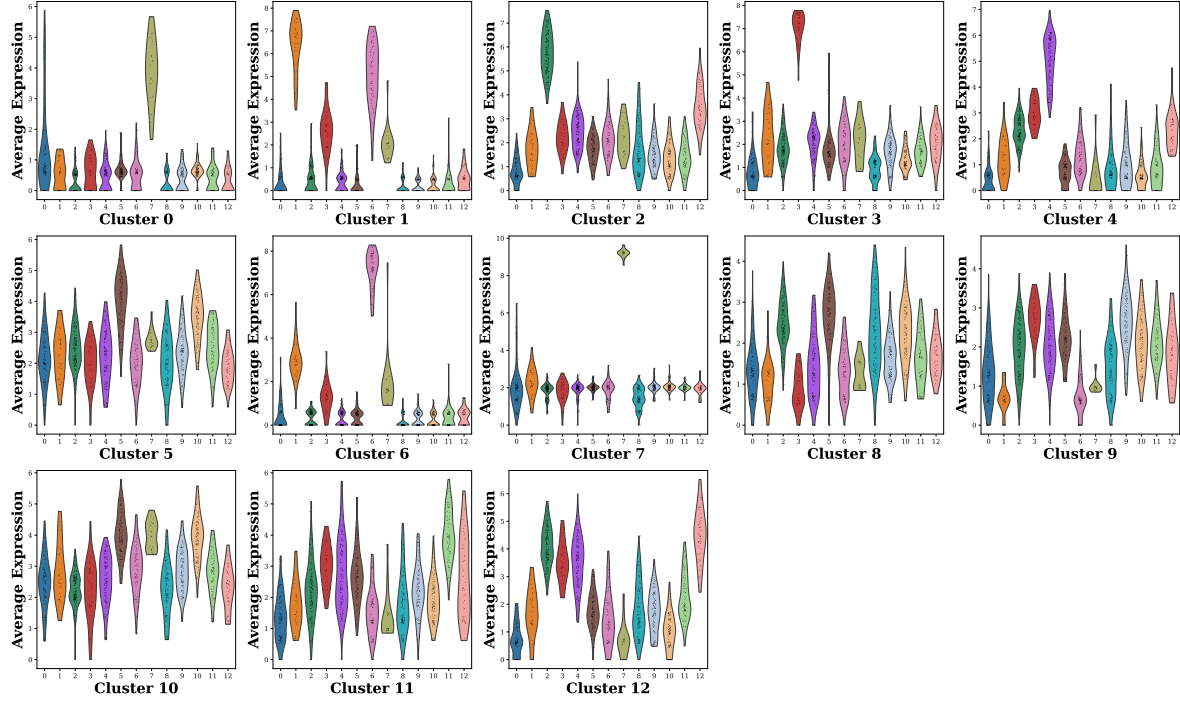
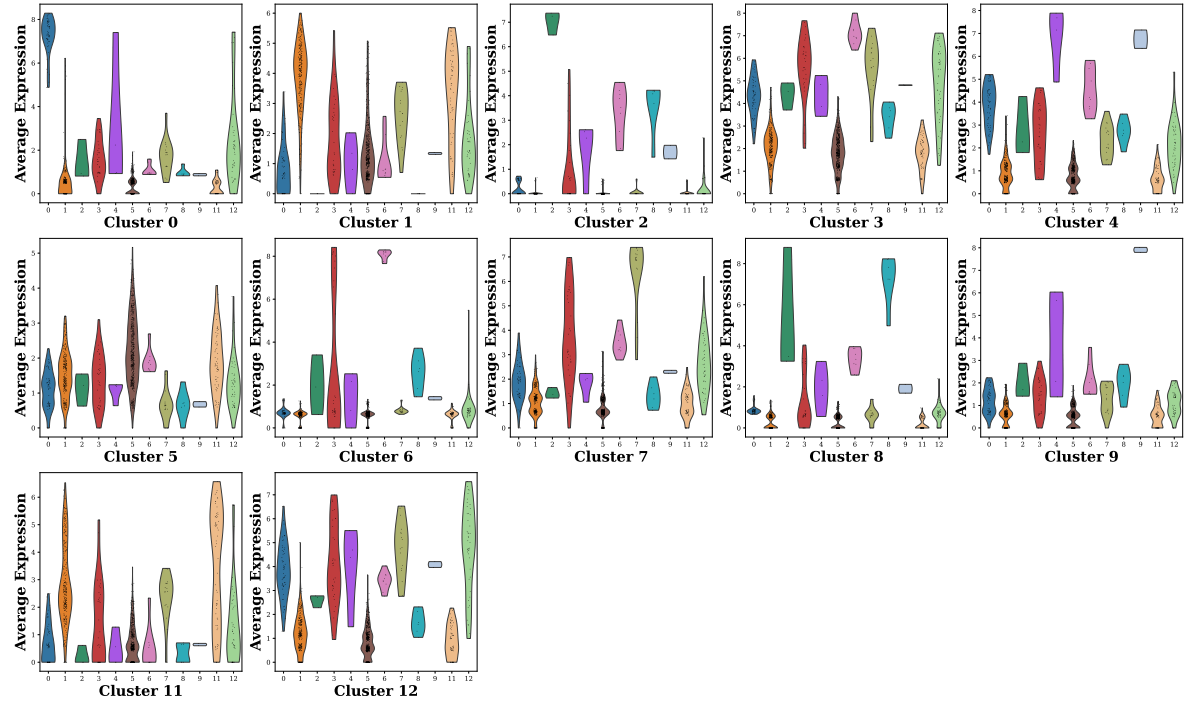


FIG. S19: Clustering Performance of PCA on the Mouse Pancreas Dataset and Cell Type Annotation using DEGs and Canonical Markers. (a) Top 10 DEGs identified for each cluster by PCA. (b) Across-cluster average expression of cluster-specific DEGs. Violin plots show the distribution of average expression levels of these DEGs across all clusters. Strong clustering performance is indicated by high expression of cluster-specific DEGs within their respective clusters and low expression in other clusters. (c) Cell type annotation using the PanglaoDB marker database. Cell types are determined by the overlap between each cluster's DEGs and cell type-specific markers in the PanglaoDB database, with match scores computed based on the proportion of matched markers.

(a) Top 10 DE Genes for Each Cluster Identified by graph-sc in Mouse Pancreas Data

Cluster 0	Cluster 1	Cluster 2	Cluster 3	Cluster 4	Cluster 5
Pecam1	Rbp4	Cd52	Prdx1	Smox	Hmox1
Egfl7	Gpx3	Ferm3	Flna	Ramp3	Pdyn
Flt1	Serpingle1	Rac2	Anxa2	Zfp36l1	Psap
Cdh5	Clu	Coro1a	Msn	Srgn	Rspo4
Sparc	Arg1	Arhgdib	Fth1	Pde4b	Vgf
Col4a2	Spp1	Dock2	Tuba1c	Tmsb4x	Zranb2
B2m	Ttr	Il2rg	Tmsb4x	B2m	Ubr4
Plvap	Tspan8	Itgb2	Cd44	Traf1	Slc35b4
Ctla2a	Irx1	Myo1g	B2m	Lsp1	Satb1
Sox4	Basp1	Ptprc	Cd14	Rgs1	Ctsb
Cluster 6	Cluster 7	Cluster 8	Cluster 9	Cluster 11	Cluster 12
Tgfb1	S100a6	Ighm	Cytip	Rbp4	Anxa2
Fcer1g	Anxa2	Coro1a	Marcks1	Hhex	Csrp1
Lyz2	Csrp1	Cd74	Cd80	Cd24a	Tuba1c
H2-Eb1	Myof	B2m	Tbc1d4	Clu	Actn1
Pla2g7	Cd14	Pou2af1	Lsp1	Gpx3	Tmsb4x
Mpeg1	Cyba	Iglc3	Tmsb4x	Arg1	Msn
H2-Ab1	Krt19	Cd79a	Tmem123	Mest	Flna
Fth1	Onecut2	Igk	Gm13546	Gap43	Rhoc
Laptm5	Fth1	Rac2	Ccl22	Peg10	Ahnak
Ctss	Tspan8	Cd52	Ccr7	Tspan8	Cald1

(b) Average Expression of Top 10 DE Genes from Each Cluster Found by graph-sc



(c) Top Cell Type Matches for Each Cluster Identified by graph-sc Based on PanglaoDB Markers

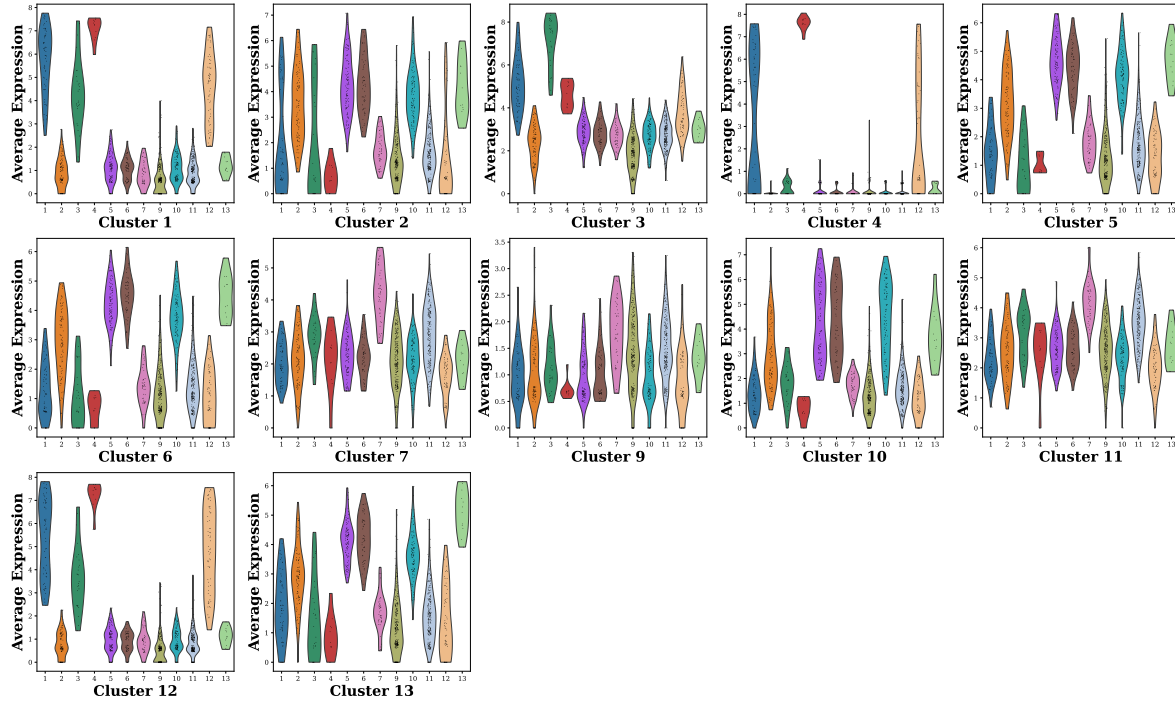
Cluster	Match Type	Annotation	Score
0	Primary	No annotation	-
1	Primary	Nuocytes	0.0833
	Secondary	Ductal cells	0.0750
2	Primary	Langerhans cells	0.0667
	Secondary	Tuft cells	0.0526
3	Primary	No annotation	-
	Primary	No annotation	-
5	Primary	Red pulp macrophages	0.0833
	Primary	No annotation	-
6	Primary	No annotation	-
	Primary	Microfold cells	0.0588
7	Primary	Ductal cells	0.0500
	Primary	B cells naive	0.0893
8	Primary	Plasma cells	0.0746
	Secondary	Myeloid-derived suppressor cells	0.0833
9	Primary	Langerhans cells	0.0667
	Secondary	Delta cells	0.0625
11	Primary	Nuocytes	0.0833
	Secondary	Myofibroblasts	0.1111
12	Primary	Mesangial cells	0.0526

FIG. S20: Clustering Performance of graph-sc on the Mouse Pancreas Dataset and Cell Type Annotation using DEGs and Canonical Markers. (a) Top 10 DEGs identified for each cluster by graph-sc. (b) Across-cluster average expression of cluster-specific DEGs. Violin plots show the distribution of average expression levels of these DEGs across all clusters. Strong clustering performance is indicated by high expression of cluster-specific DEGs within their respective clusters and low expression in other clusters. (c) Cell type annotation using the PanglaoDB marker database. Cell types are determined by the overlap between each cluster's DEGs and cell type-specific markers in the PanglaoDB database, with match scores computed based on the proportion of matched markers.

(a) Top 10 DE Genes for Each Cluster Identified by TsImpute in Mouse Pancreas Data

Cluster 1	Cluster 2	Cluster 3	Cluster 4	Cluster 5	Cluster 6
Anxa2	Rbp4	Prdx1	Pecam1	Gpx3	Gpx3
Tmsb4x	Gpx3	Cyba	Mmrn2	Rbp4	Rbp4
B2m	Cldn4	Tmsb4x	Egfl7	Serpingle1	Spp1
Msn	Clu	Fth1	Esam	Spp1	Clu
Sox4	Krt18	Ftl1	Adgrl4	Tspan8	Serpingle1
Ier3	Arg1	B2m	Cdh5	Arg1	Arg1
Sparc	Krt8	Flna	Dll4	Vgf	Ttr
Flna	Spp1	Lgals3	Flt1	Igfbp7	Dnajb1
Ifitm3	Hhex	Cd44	Plvap	Ttr	Irx1
Col4a1	Cd24a	Smox	S1pr1	Fgl2	Peg10
Cluster 7	Cluster 9	Cluster 10	Cluster 11	Cluster 12	Cluster 13
Vgf	Psap	Gpx3	Hmxo1	Msn	Spp1
Hmxo1	Pdyn	Rbp4	Rspo4	B2m	Gpx3
Nr4a2	Ctrb1	Ttr	Psap	Col4a2	Tspan8
Zranb2	Msln	Mafb	Ftl1	Sparc	Rbp4
Pdyn	Amy1	Serpingle1	Pdyn	Col4a1	Clu
Ctsb	Derl3	Krt8	Adgrl1	Anxa2	Ttr
Ftl1	Th	Vgf	Zranb2	Tmsb4x	Fosb
Gsto1	Ubr4	Irx1	Ctsb	Ier3	Serpingle1
Slc35b4	Hspa1b	Basp1	Slc35b4	Pmepa1	Fabp5
Rspo4	Cd79a	Krt18	Npat	Ednrb	Actn1

(b) Average Expression of Top 10 DE Genes from Each Cluster Found by TsImpute



(c) Top Cell Type Matches for Each Cluster Identified by TsImpute Based on PanglaoDB Markers

Cluster	Match Type	Annotation	Score
1	Primary	Pancreatic stellate cells	0.0690
2	Primary	Hepatoblasts	0.1765
	Secondary	Merkel cells	0.1333
3	Primary	No annotation	-
4	Primary	Stromal cells	0.0606
5	Primary	Nuocytes	0.0833
	Secondary	Ductal cells	0.0750
6	Primary	Nuocytes	0.0833
	Secondary	Ductal cells	0.0500
7	Primary	Red pulp macrophages	0.0833
	Secondary	Dopaminergic neurons	0.0500
9	Primary	Juxtaglomerular cells	0.1429
	Secondary	Adrenergic neurons	0.1250
10	Primary	Merkel cells	0.0667
	Secondary	Alpha cells	0.0652
11	Primary	Red pulp macrophages	0.0833
12	Primary	Pancreatic stellate cells	0.0690
13	Primary	Ductal cells	0.0750

FIG. S21: Clustering Performance of tsImpute on the Mouse Pancreas Dataset and Cell Type Annotation using DEGs and Canonical Markers. (a) Top 10 DEGs identified for each cluster by tsImpute. (b) Across-cluster average expression of cluster-specific DEGs. Violin plots show the distribution of average expression levels of these DEGs across all clusters. Strong clustering performance is indicated by high expression of cluster-specific DEGs within their respective clusters and low expression in other clusters. (c) Cell type annotation using the PanglaoDB marker database. Cell types are determined by the overlap between each cluster's DEGs and cell type-specific markers in the PanglaoDB database, with match scores computed based on the proportion of matched markers.

(a) Top 10 DE Genes for Each Cluster Identified by CAKE in Mouse Pancreas Data

Cluster 0	Cluster 1	Cluster 2	Cluster 3	Cluster 4	Cluster 5	Cluster 6
Hmox1	Rbp4	Pdyn	Pecam1	Krt19	B2m	Gpx3
Ezr	Gpx3	Hspa1b	Egfl7	Clu	Cd74	Ttr
Pdyn	Hhex	Rsp04	Cdh5	Krt8	Tmsb4x	Mafb
Psap	Arg1	Zranb2	Col4a2	Anxa2	Cytip	Spp1
Ddit4	Cd24a	Hspa1a	Sparc	Myof	Coro1a	Irx1
Tnfrsf9	Clu	Nr4a2	Flt1	Krt18	Srgn	Id1
Stk4	Tspan8	Vgf	B2m	S100a6	Cyba	Vgf
Th	Mest	Slc35b4	Plvap	Ahnak	Ctss	Rbp4
Il6st	Serp1	Adgrl1	Ctla2a	Muc1	Laptm5	Id3
Gst01	Cpa2	Hmox1	Msn	Anxa3	H2-Eb1	Basp1
Cluster 7	Cluster 8	Cluster 9	Cluster 10	Cluster 11	Cluster 12	
Rbp4	Psap	Anxa2	Gpx3	Gm13889	Gpx3	
Hhex	Krt18	Cald1	Ttr	Ednrb	Rbp4	
Cd24a	Rsp04	Fth1	Rbp4	Igfbp5	Serp1	
Arg1	Msln	Flna	Irx1	Smtn	Cldn4	
Clu	Nr4a1	Sparc	Mafb	Sparc	Tspan8	
Tspan8	Cela2a	Ier3	Spp1	Msn	Cldn3	
Igfbp7	Ctrb1	Msn	Vgf	S1pr3	Krt18	
Gpx3	Hspa1b	Csrp1	Id3	Rgs5	Ttr	
Mest	Ttr	Cd44	Basp1	Ndufa4l2	Krt8	
Gap43	Gstm2	Igfbp7	Serp1	Col4a1	Tmsb4x	

(c) Top Cell Type Matches for Each Cluster Identified by CAKE Based on PanglaoDB Markers

Cluster	Match Type	Annotation	Score
0	Primary	Juxtaglomerular cells	0.1429
	Secondary	Adrenergic neurons	0.1250
1	Primary	Nuocytes	0.0833
	Secondary	Ductal cells	0.0750
2	Primary	Dopaminergic neurons	0.0500
	Secondary	No annotation	-
3	Primary	Merkel cells	0.1333
	Secondary	Hepatoblasts	0.1176
5	Primary	No annotation	-
6	Primary	Alpha cells	0.0652
7	Primary	Nuocytes	0.0833
	Secondary	Delta cells	0.0625
8	Primary	Merkel cells	0.0667
	Secondary	Hepatoblasts	0.0588
9	Primary	Myofibroblasts	0.1111
10	Primary	Alpha cells	0.0652
11	Primary	Pancreatic stellate cells	0.1379
	Secondary	Glomus cells	0.0714
12	Primary	Merkel cells	0.1333
	Secondary	Hepatoblasts	0.1176

(b) Average Expression of Top 10 DE Genes from Each Cluster Found by CAKE

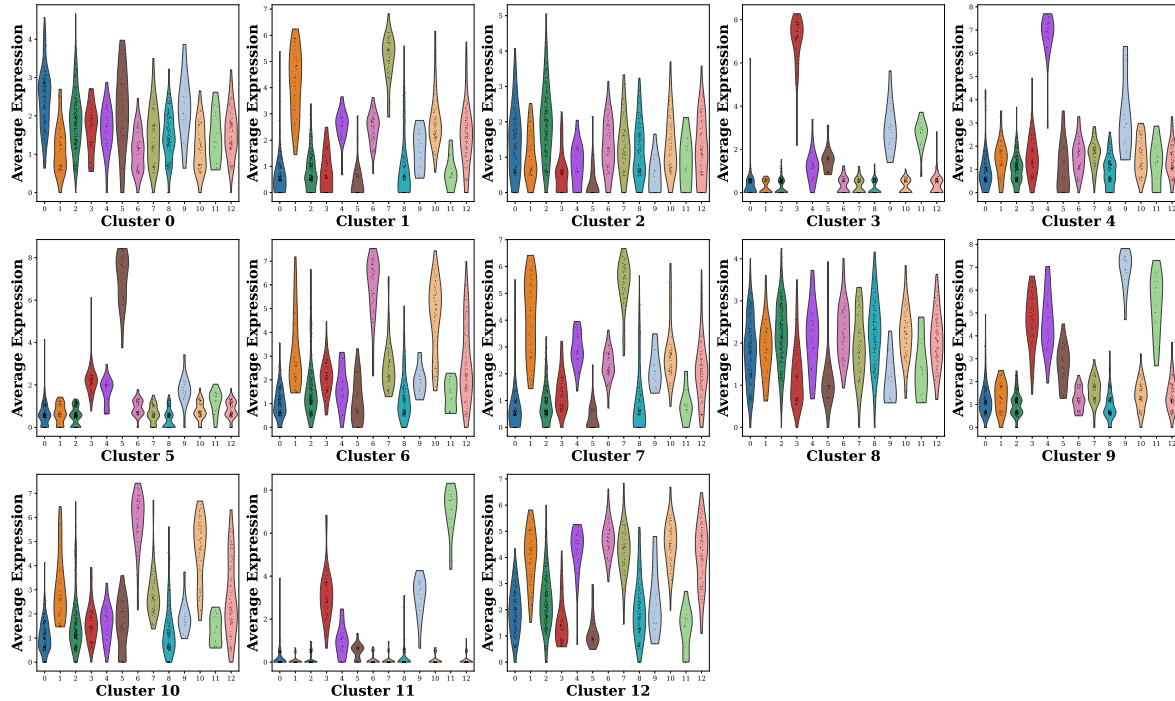


FIG. S22: Clustering Performance of CAKE on the Mouse Pancreas Dataset and Cell Type Annotation using DEGs and Canonical Markers. (a) Top 10 DEGs identified for each cluster by CAKE. (b) Across-cluster average expression of cluster-specific DEGs. Violin plots show the distribution of average expression levels of these DEGs across all clusters. Strong clustering performance is indicated by high expression of cluster-specific DEGs within their respective clusters and low expression in other clusters. (c) Cell type annotation using the PanglaoDB marker database. Cell types are determined by the overlap between each cluster's DEGs and cell type-specific markers in the PanglaoDB database, with match scores computed based on the proportion of matched markers.

(a) Top 10 DE Genes for Each Cluster Identified by scASDC in Mouse Pancreas Data

Cluster 0	Cluster 1	Cluster 2	Cluster 3	Cluster 4	Cluster 5	Cluster 6
Pdyn	Mpeg1	Sparc	Rbp4	Ttr	Anxa2	Adgrl1
Hmox1	Ctss	Sox4	Cd24a	Vgf	Flna	Psap
Rspo4	Fth1	B2m	Hhex	Gpx3	Ier3	Pdyn
Psap	Psap	Col4a2	Arg1	Irx1	Serpinh1	Trim9
Zranb2	Fcer1g	Pecam1	Clu	Tmsb4x	Csrp1	Ctrb1
Satb1	Cd74	Egfl7	Igfbp7	Spp1	Col4a1	Zranb2
Actn1	H2-Eb1	Msn	Gpx3	Rbp4	Zfp36l1	Lrig2
Slc35b4	Laptm5	Flt1	Mest	Id3	Msn	Fam171a1
Krt8	Ftl1	Cdh5	Gap43	Fev	Sparc	Phlda1
Ftl1	H2-Aa	Rhoc	Tspan8	Nr4a2	Fth1	Krt18
Cluster 7	Cluster 8	Cluster 9	Cluster 10	Cluster 11	Cluster 12	
Hspa1b	Vgf	Gpx3	Hmox1	Ttr	B2m	
Hspa1a	Ttr	Rbp4	Vgf	Spp1	Tmsb4x	
Dnajb1	Krt8	Ttr	Prdx1	Abhd18	Coro1a	
Hmox1	Fgl2	Serpingle1	Adgrl1	Mafb	Fth1	
Psap	Zranb2	Irx1	Fgl2	Fgl2	Cd74	
Rspo4	Ctsb	Clu	Tmem123	Gpx3	Cytip	
Pdyn	Gpx3	Spp1	Slc35b4	Serpingle1	Tmem123	
Ddit4	Cd68	Mafb	Ctsb	Irx1	Ctss	
Msln	Cldn4	Krt8	Psap	Actn1	H2-Eb1	
Ubr4	Ftl1	Krt18	Zranb2	Vgf	H2-Aa	

(c) Top Cell Type Matches for Each Cluster Identified by scASDC Based on PanglaoDB Markers

Cluster	Match Type	Annotation	Score
0	Primary	Red pulp macrophages	0.0833
1	Primary	No annotation	-
2	Primary	No annotation	-
3	Primary	Nuocytes	0.0833
	Secondary	Delta cells	0.0625
4	Primary	Serotonergic neurons	0.1250
	Secondary	Alpha cells	0.0652
5	Primary	Pancreatic stellate cells	0.0690
6	Primary	Merkel cells	0.0667
	Secondary	Hepatoblasts	0.0588
7	Primary	Red pulp macrophages	0.0833
8	Primary	Merkel cells	0.0667
	Secondary	Hepatoblasts	0.0588
9	Primary	Merkel cells	0.1333
	Secondary	Hepatoblasts	0.1176
10	Primary	Red pulp macrophages	0.0833
11	Primary	Alpha cells	0.0652
	Secondary	Ductal cells	0.0500
12	Primary	No annotation	-

(b) Average Expression of Top 10 DE Genes from Each Cluster Found by scASDC

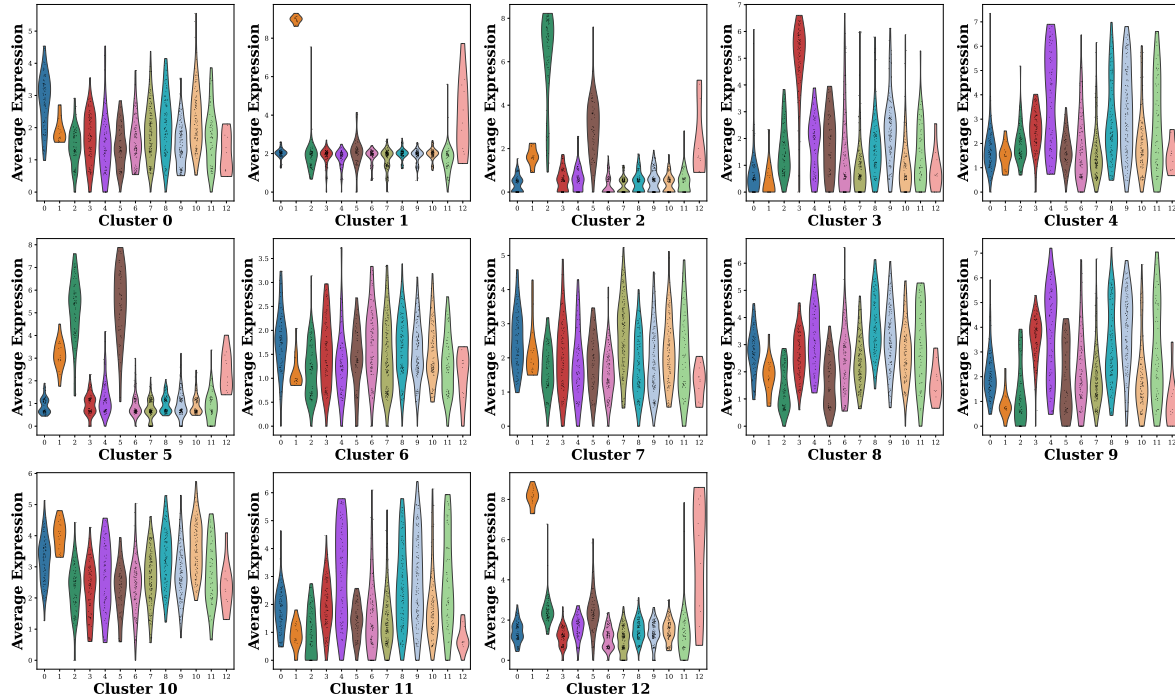


FIG. S23: Clustering Performance of scASDC on the Mouse Pancreas Dataset and Cell Type Annotation using DEGs and Canonical Markers. (a) Top 10 DEGs identified for each cluster by scASDC. (b) Across-cluster average expression of cluster-specific DEGs. Violin plots show the distribution of average expression levels of these DEGs across all clusters. Strong clustering performance is indicated by high expression of cluster-specific DEGs within their respective clusters and low expression in other clusters. (c) Cell type annotation using the PanglaoDB marker database. Cell types are determined by the overlap between each cluster's DEGs and cell type-specific markers in the PanglaoDB database, with match scores computed based on the proportion of matched markers.

(a) Top 10 DE Genes for Each Cluster Identified by CoMem-DIPH in Mouse Brain Data

Cluster 0	Cluster 1	Cluster 2	Cluster 3	Cluster 4
Pcp4	Mag	Sparc	Gad1	Csf1r
Slc1a2	Gjc3	Epas1	Gad2	Ctss
Lamp5	Ptgds	Esam	Vstm2a	Tyrobp
Ier5	Nfasc	Itm2a	Slc6a1	C1qa
Myl4	Fa2h	Igfbp7	Dlx6os1	C1qb
Vstm2a	Hapl2	Hes1	Dner	Rnase4
Clu	S100b	Myl2a	Cnr1	Fcrls
Ablim1	Serpib1a	Ly6c1	Igf1	Laptm5
Tnnc1	S100a6	Id3	Arl4c	Fcgr3
Rorb	S100a1	Cldn5	Pnoc	Sepp1
Cluster 5	Cluster 6	Cluster 7	Cluster 8	
Clu	Wfs1	Tmem212	Nnat	
Slc1a3	Rasd1	Ccde153	Dcn	
Gja1	Tpm1	Cd24a	Resp18	
Ppap2b	Nr4a2	Rarres2	Nr4a2	
Slc4a4	Palmd	Dynlrb2	Cnr1	
Gpr37l1	Flna	Mia	Wfs1	
Atp1a2	Kctd12	Fam183b	Kctd12	
Pptrz1	Ncan	1110017D15Rik	Itga8	
Ntsr2	Dner	1700094D03Rik	Efnb2	
Aldoc	Itga8	Riiad1	Rgs2	

(c) Top Cell Type Matches for Each Cluster Identified by CoMem-DIPH in Based on PanglaoDB Markers

Cluster	Match Type	Annotation	Score
0	Primary	Glutaminergic neurons	0.1000
1	Primary	Nuocytes	0.0833
	Secondary	Enteric glia cells	0.0588
2	Primary	Retinal progenitor cells	0.0769
	Secondary	Pancreatic progenitor cells	0.0667
3	Primary	GABAergic neurons	0.2000
4	Primary	Kupffer cells	0.0652
	Secondary	Microglia	0.0633
5	Primary	Bergmann glia	0.1220
	Secondary	Astrocytes	0.0952
6	Primary	Peritubular myoid cells	0.0800
	Secondary	Mesangial cells	0.0702
7	Primary	Ciliated cells	0.1111
	Secondary	Ependymal cells	0.1017
8	Primary	Osteocytes	0.2000
	Secondary	Meningeal cells	0.1111

(b) Average Expression of Top 10 DE Genes from Each Cluster Found by CoMem-DIPH

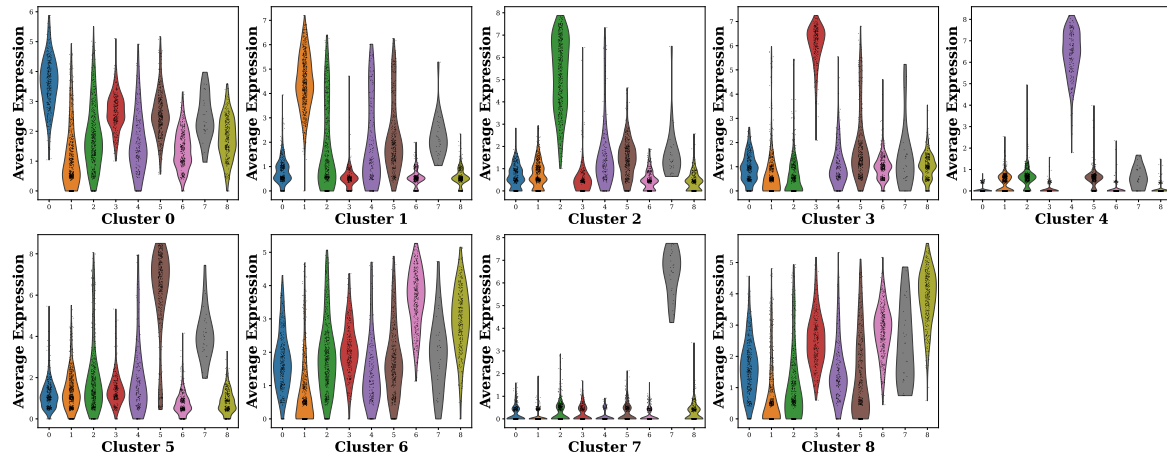


FIG. S24: Clustering Performance of CoMem-DIPH on the Mouse Brain Dataset and Cell Type Annotation using DEGs and Canonical Markers. (a) Top 10 DEGs identified for each cluster by CoMem-DIPH. (b) Across-cluster average expression of cluster-specific DEGs. Violin plots show the distribution of average expression levels of these DEGs across all clusters. Strong clustering performance is indicated by high expression of cluster-specific DEGs within their respective clusters and low expression in other clusters. (c) Cell type annotation using the PanglaoDB marker database.

(a) Top 10 DE Genes for Each Cluster Identified by PCA in Mouse Brain Data

Cluster 0	Cluster 1	Cluster 2	Cluster 3	Cluster 4
Pcp4	Slc1a3	Itm2a	Mag	Wfs1
Slc1a2	Clu	Sparc	Gjc3	Nnat
Lamp5	Gja1	Ly6c1	Ptgds	Nr4a2
Ier5	Ppap2b	Cldn5	Nfasc	Dcn
Myl4	Slc1a2	Ptprb	Fa2h	Kctd12
Vstm2a	Aqp4	Slco1a4	Hapln2	Rasd1
Clu	Gpr37l1	Pltp	Serpib1a	Cnr1
Rorb	Pla2g7	Esam	S100b	Tpm1
Tnncl	Atp1a2	Flt1	Klk6	Itga8
Ablim1	Mt2	Abcb1a	S100a1	Palmd
Cluster 5 Cluster 6 Cluster 7 Cluster 8				
Gad1	Pf4	Hexb	Myl9	
Gad2	Mrc1	Ctss	Mgp	
Slc6a1	Tyrobp	P2ry12	Crip1	
Vstm2a	Lyz2	Cx3cr1	Acta2	
Dner	C1qa	Csf1r	Tagln	
Dlx6os1	Csf1r	Gpr34	Tpm1	
Igf1	Cbr2	Laptm5	Tpm2	
Arl4c	Stab1	Tyrobp	S100a11	
Resp18	Ms4a7	Rnase4	Myh11	
Cnr1	Sepp1	C1qb	Mustn1	

(c) Top Cell Type Matches for Each Cluster Identified by PCA Based on PanglaoDB Markers

Cluster	Match Type	Annotation	Score
0	Primary	Glutaminergic neurons	0.1000
1	Primary	Bergmann glia	0.1220
	Secondary	Glutaminergic neurons	0.1000
2	Primary	No annotation	—
3	Primary	Nuocytes	0.0833
	Secondary	Oligodendrocytes	0.0690
4	Primary	Meningeal cells	0.1111
	Secondary	Peritubular myoid cells	0.0800
5	Primary	GABAergic neurons	0.2000
6	Primary	No annotation	—
7	Primary	Microglia	0.0759
8	Primary	Myofibroblasts	0.3333
	Secondary	Vascular smooth muscle cells	0.3333

(b) Average Expression of Top 10 DE Genes from Each Cluster Found by PCA

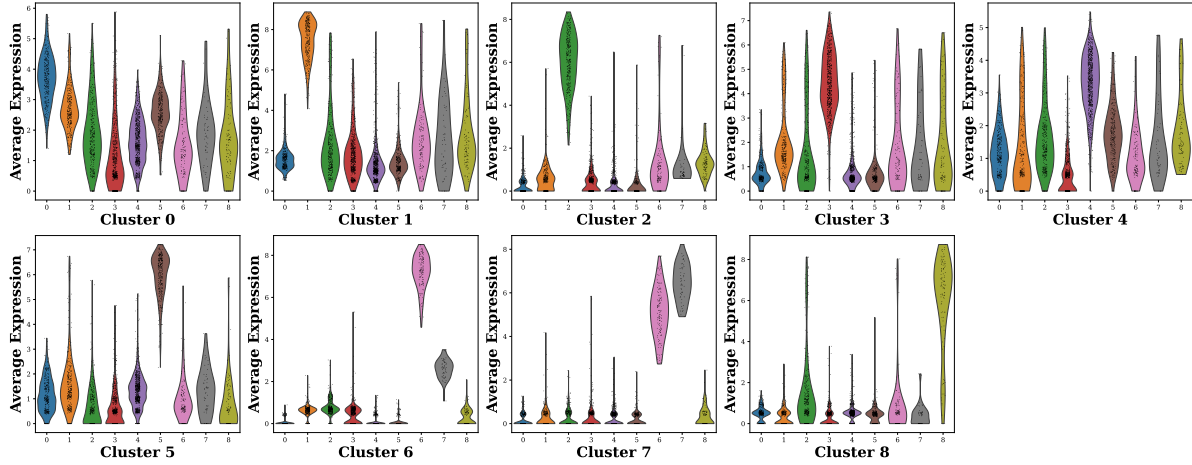


FIG. S25: Clustering Performance of PCA on the Mouse Brain Dataset and Cell Type Annotation using DEGs and Canonical Markers. (a) Top 10 DE Genes for Each Cluster Identified by PCA in Mouse Brain Data. (b) Across-cluster average expression of cluster-specific DEGs. Violin plots show the distribution of average expression levels of these DEGs across all clusters. (c) Cell type annotation using the PanglaoDB marker database.

(a) Top 10 DE Genes for Each Cluster Identified by graph-sc in Mouse Brain Data

Cluster 0	Cluster 1	Cluster 2	Cluster 3	Cluster 4
Wfs1	Itm2a	Clu	Pf4	Mag
Nnat	Sparc	Gja1	Mrc1	Nfasc
Nr4a2	Ly6c1	Pla2g7	Lyz2	Tmem141
Tpm1	Ptprb	Gpr37l1	Csf1r	Ptgds
Rgs2	Cldn5	Slc1a3	Tyrobp	Gjc3
Ncan	Pltp	Mt1	Cbr2	Gpr17
Resp18	Slco1a4	Aqp4	C1qa	Abhd3
Dcn	Esam	Apoe	Stab1	Rnf122
Cnr1	Slc2a1	Mt2	Ccl7	Ppap2b
Ier5	Abcb1a	Ppap2b	F13a1	Fa2h
Cluster 5	Cluster 6	Cluster 7	Cluster 8	
Itm2a	Mag	Slc6a1	Ccl24	
Cldn5	Gjc3	Gad1	Ms4a7	
Ly6c1	Hapln2	Gad2	Mrc1	
Sparc	Serpinb1a	Clu	Lyz2	
Ptprb	Fa2h	Dner	Fcgr3	
Flt1	Ptgds	Vstm2a	Dab2	
Slco1a4	Klk6	Dlx6os1	Ctsc	
Egfl7	S100b	Cnr1	Tyrobp	
Esam	S100a6	Arl4c	Sepp1	
Slco1c1	S100a1	Igf1	Pf4	

(c) Top Cell Type Matches for Each Cluster Identified by graph-sc Based on PanglaoDB Markers

Cluster	Match Type	Annotation	Score
0	Primary	Meningeal cells	0.1111
	Secondary	Dopaminergic neurons	0.0500
1	Primary	No annotation	—
	Secondary	Bergmann glia	0.0976
2	Primary	Astrocytes	0.0952
	Secondary	No annotation	—
3	Primary	Nuocytes	0.0833
	Secondary	Meningeal cells	0.0556
4	Primary	No annotation	—
	Secondary	Nuocytes	0.0833
5	Primary	Oligodendrocytes	0.0690
	Secondary	No annotation	—
6	Primary	GABAergic neurons	0.2000
	Secondary	No annotation	—
7	Primary	No annotation	—
	Secondary	No annotation	—
8	Primary	No annotation	—
	Secondary	No annotation	—

(b) Average Expression of Top 10 DE Genes from Each Cluster Found by graph-sc

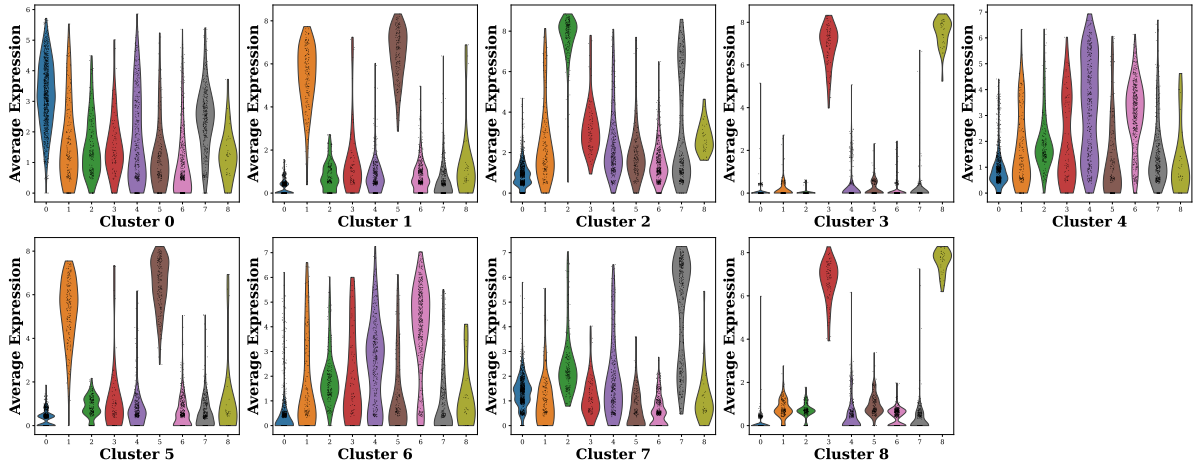


FIG. S26: Clustering Performance of graph-sc on the Mouse Brain Dataset and Cell Type Annotation using DEGs and Canonical Markers. (a) Top 10 DEGs identified for each cluster by graph-sc. (b) Across-cluster average expression of cluster-specific DEGs. Violin plots show the distribution of average expression levels of these DEGs across all clusters. (c) Cell type annotation using the PanglaoDB marker database.

(a) Top 10 DE Genes for Each Cluster Identified by TsImpute in Mouse Brain Data

Cluster 1	Cluster 2	Cluster 3	Cluster 4	Cluster 5
Tmem141	Mag	Pla2g7	Sparc	Gad1
Mag	Gjc3	Dusp1	Sepp1	Gad2
Ptgds	Nfasc	Zfp36l1	Slco1c1	Igf1
Nfasc	Fa2h	Apoe	Hes1	Vstm2a
Prom1	Ptgds	Vamp8	Zfp36l1	Slc6a1
Gjc3	Haplh2	Abca1	Cyr61	Arl4c
Rnf122	Tmem141	Tmem176b	Id3	Dlx6os1
Fa2h	Prdx6	Cyr61	Atp1a2	Resp18
9630013A20Rik	Abhd3	Btg2	Epas1	Dner
Mfsd2a	S100b	Anxa5	Serpinh1	Maf
Cluster 6	Cluster 7	Cluster 8	Cluster 9	
Vstm2a	Apoe	Mag	Wfs1	
Dner	Sepp1	Gjc3	Nnat	
Resp18	Pla2g7	Ptgds	Nr4a2	
Cnr1	Mt1	Haplh2	Cnr1	
Gad2	Sat1	Fa2h	Resp18	
Arl4c	Tmem176b	Nfasc	Rgs2	
Gad1	Sdc4	Serpimb1a	Tpm1	
Dlx6os1	Ednrb	S100b	Ncan	
Col19a1	Zfp36l1	S100a1	Rasd1	
Igf1	Atp1a2	S100a6	Dcn	

(c) Top Cell Type Matches for Each Cluster Identified by TsImpute Based on PanglaoDB Markers

Cluster	Match Type	Annotation	Score
1	Primary	Nuocytes	0.0833
	Secondary	Crypt cells	0.0625
2	Primary	Nuocytes	0.0833
	Secondary	Enteric glia cells	0.0588
3	Primary	Spermatozoa	0.1111
4	Primary	Retinal progenitor cells	0.0769
	Secondary	Pancreatic progenitor cells	0.0667
5	Primary	GABAergic neurons	0.2000
6	Primary	GABAergic neurons	0.1333
7	Primary	No annotation	—
8	Primary	Nuocytes	0.0833
	Secondary	Enteric glia cells	0.0588
9	Primary	Meningeal cells	0.1111
	Secondary	Peritubular myoid cells	0.0800

(b) Average Expression of Top 10 DE Genes from Each Cluster Found by TsImpute

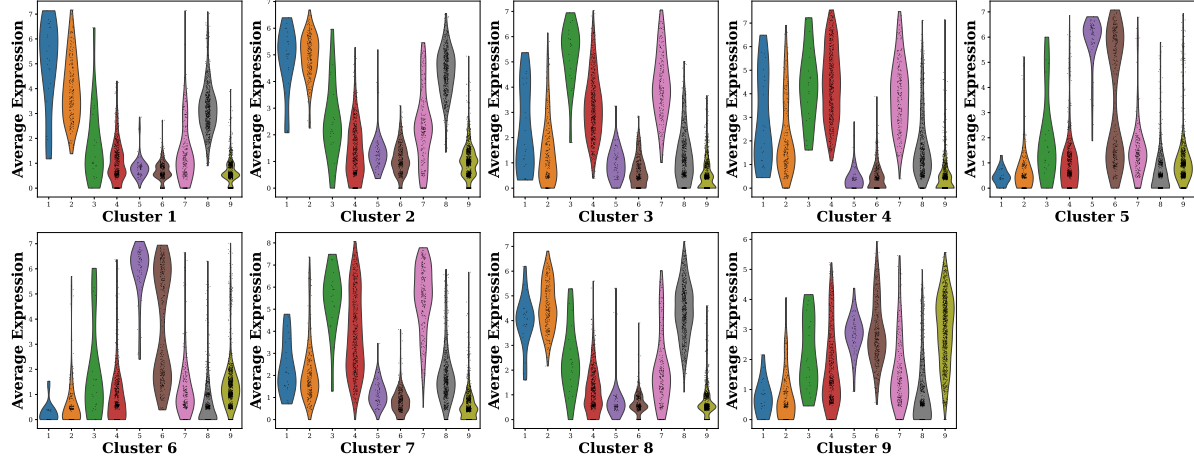


FIG. S27: Clustering Performance of tsImpute on the Mouse Brain Dataset and Cell Type Annotation using DEGs and Canonical Markers. (a) Top 10 DEGs identified for each cluster by tsImpute. (b) Across-cluster average expression of cluster-specific DEGs. Violin plots show the distribution of average expression levels of these DEGs across all clusters. (c) Cell type annotation using the PanglaoDB marker database.

(a) Top 10 DE Genes for Each Cluster Identified by CAKE in Mouse Brain Data

Cluster 0	Cluster 1	Cluster 2	Cluster 3	Cluster 4
Mia	Gad1	Pf4	Hexb	Hexb
Dynlrb2	Gad2	Mrc1	Ctss	Cx3cr1
Calml4	Slc6a1	Csf1r	P2ry12	Ctss
1110017D15Rik	Vstm2a	Tyrobp	Csf1r	Csf1r
1700094D03Rik	Dner	Ms4a7	Laptm5	P2ry12
Rspn1	Dlx6os1	Lyz2	C1qa	Gpr34
Clu	Igf1	Cbr2	Tyrobp	C1qb
Fam183b	Arl4c	Sepp1	Cx3cr1	Laptm5
Tmem212	Cnr1	Stab1	Ccl3	Siglech
Ccdc153	Resp18	Fcgr3	Cd53	Fcrls
Cluster 5	Cluster 6	Cluster 7	Cluster 8	
Apoe	Lamp5	Clu	Palmd	
Gja1	Pcp4	Slc1a2	Wfs1	
Pla2g7	Tpm1	Ntsr2	Itm2a	
Mt1	Ier5	Prdx6	Slc16a1	
Slc1a3	Myo1b	Aqp4	Ly6c1	
Ppap2b	Tnncl	Aldoc	Nfasc	
Atp1a2	Mylk	Mt1	Ptprb	
Gpr37l1	Mustn1	Pla2g7	Cldn5	
Mt2	Igfbp5	Slc1a3	Gjc3	
Slc4a4	Myl4	Gja1	Mag	

(c) Top Cell Type Matches for Each Cluster Identified by CAKE Based on PanglaoDB Markers

Cluster	Match Type	Annotation	Score
0	Primary	Ciliated cells	0.1111
	Secondary	Ependymal cells	0.1017
1	Primary	GABAergic neurons	0.2000
2	Primary	Microglia	0.0506
3	Primary	Microglia	0.0759
4	Primary	Microglia	0.1013
5	Primary	Bergmann glia	0.0976
	Secondary	Astrocytes	0.0952
6	Primary	No annotation	—
7	Primary	Bergmann glia	0.1220
	Secondary	Astrocytes	0.1111
8	Primary	No annotation	—

(b) Average Expression of Top 10 DE Genes from Each Cluster Found by CAKE

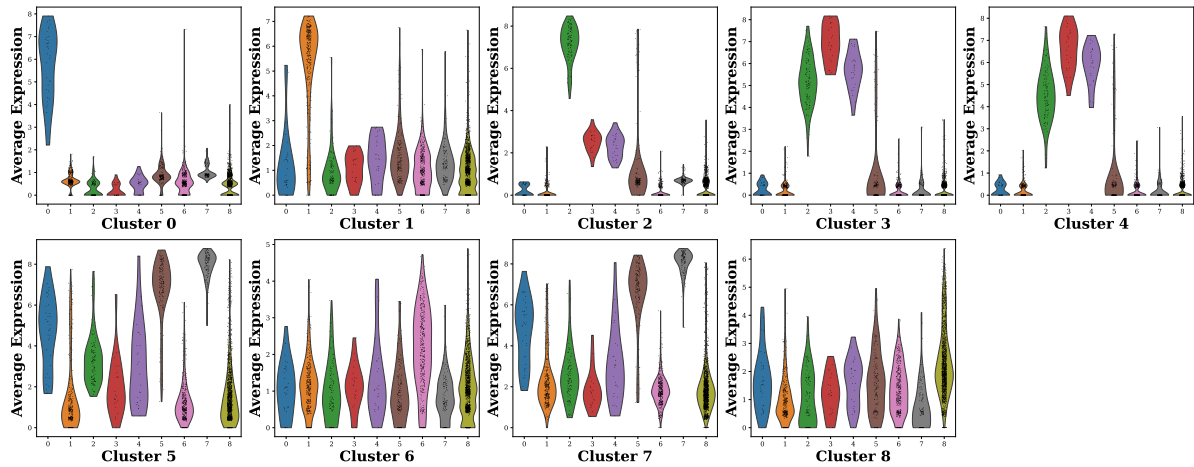


FIG. S28: Clustering Performance of CAKE on the Mouse Brain Dataset and Cell Type Annotation using DEGs and Canonical Markers. (a) Top 10 DEGs identified for each cluster by CAKE. (b) Across-cluster average expression of cluster-specific DEGs. Violin plots show the distribution of average expression levels of these DEGs across all clusters. (c) Cell type annotation using the PanglaoDB marker database.

(a) Top 10 DE Genes for Each Cluster Identified by scASDC in Mouse Brain Data

Cluster 0	Cluster 1	Cluster 2	Cluster 3	Cluster 4
Tpm1	Wfs1	Ctss	Tm4sf1	Mag
Myl9	Nnat	Csf1r	Epas1	Gjc3
Acta2	Nr4a2	Rnase4	Ptprb	Ptgds
Flna	Tpm1	Tyrobp	Ly6c1	Nfasc
Crip1	Ncan	Laptm5	Sparc	Fa2h
Tagln	Rgs2	C1qa	Itm2a	Hapl2
Cald1	Resp18	C1qb	Esam	Serpina1a
Tpm2	Dcn	Cx3cr1	Ackr3	S100b
Mgp	Cnr1	Fcrls	Myl9	S100a1
Myh11	Ier5	Fcgr3	Gpr116	S100a6
Cluster 5	Cluster 6	Cluster 7	Cluster 8	
Slc1a3	Itm2a	Pf4	Gad2	
Gja1	Sparc	Mrc1	Gad1	
Ppap2b	Ly6c1	Ctsc	Vstm2a	
Clu	Cldn5	Tyrobp	Slc6a1	
Slc1a2	Ptprb	Csf1r	Dner	
Gpr37l1	Pltp	C1qb	Arl4c	
Apoe	Slco1a4	C1qa	Dlx6os1	
Atp1a2	Slco1c1	Lyz2	Igf1	
Slc4a4	Flt1	Sepp1	Resp18	
Mt2	Abcb1a	Fcgr3	Cnr1	

(c) Top Cell Type Matches for Each Cluster Identified by scASDC Based on PanglaoDB Markers

Cluster	Match Type	Annotation	Score
0	Primary	Myofibroblasts	0.4444
	Secondary	Vascular smooth muscle cells	0.3333
1	Primary	Meningeal cells	0.1111
	Secondary	Dopaminergic neurons	0.0500
2	Primary	Microglia	0.0759
	Secondary	Kupffer cells	0.0652
3	Primary	Myofibroblasts	0.1111
	Secondary	Pancreatic progenitor cells	0.0667
4	Primary	Nuocytes	0.0833
	Secondary	Enteric glia cells	0.0588
5	Primary	Bergmann glia	0.1220
	Secondary	Glutaminergic neurons	0.1000
6	Primary	No annotation	—
7	Primary	Kupffer cells	0.0652
	Secondary	Microglia	0.0506
8	Primary	GABAergic neurons	0.2000

(b) Average Expression of Top 10 DE Genes from Each Cluster Found by scASDC

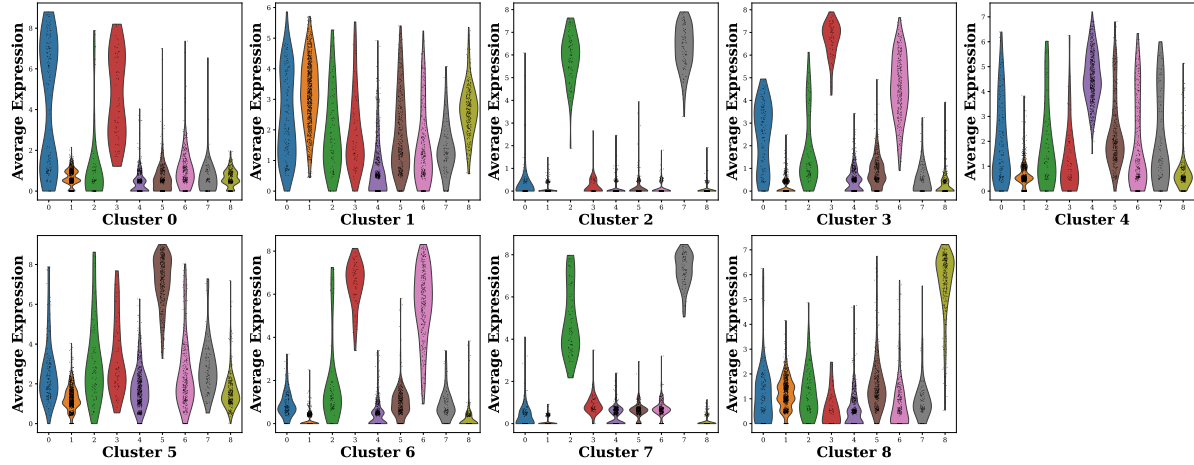


FIG. S29: Clustering Performance of scASDC on the Mouse Brain Dataset and Cell Type Annotation using DEGs and Canonical Markers. (a) Top 10 DEGs identified for each cluster by scASDC. (b) Across-cluster average expression of cluster-specific DEGs. Violin plots show the distribution of average expression levels of these DEGs across all clusters. (c) Cell type annotation using the PanglaoDB marker database.

S8. Hyperparameters

Table S4 lists the hyperparameters used in each experiment.

Figure/Table/Section	Description and Value
Experiments on simulated scRNA-seq data across modularity levels (Fig. 4 for average genes per cell type plots)	<p>Number of cells = 3000 Number of genes = 1000 Number of embedded modules = 30 Average number of cells per module = 38 Target density of the gene expression matrix = 0.03 Density within modules = 0.3 Density between modules = 0.1 Probability of inter-module connections = 0.6 Average background expression = 10 Average within-module expression = 20 Average inter-module expression = 10 Workers = 30 Walk length = 30 Embedding dimensions = 30 Preference exponent = 50 Average number of genes per module $\in \{10, 20, 30, 40, 70, 80, 90, 100\}$</p>
Experiments on simulated scRNA-seq data across modularity levels (Fig. 4 for number of modules plots)	<p>Number of embedded modules $\in \{10, 20, 30, 40, 70, 80, 90, 100\}$ Average number of genes per module = 50 Average number of cells per module = (# genes / # modules) + 3 Other parameters are the same as Fig. 4 for average genes per cell type plots.</p>
Experiments on the impact of module sizes on ARI clustering performance (Fig. 5)	Same as in Fig. 4 for average genes per cell type plots.
Experiments on the impact of module counts on ARI clustering performance (Fig. 6)	Same as in Fig. 4 for number of modules.
Comparison of ARI and NMI across clustering methods for the ScMixology benchmark datasets (Table IV)	<p>Number of highly expressed genes used = 500 Preference exponent = 10 Workers = 50 Walk length = 10 Embedding dimensions = 10</p>
Experiments on human pancreas (Section III F)	<p>Number of highly expressed genes used = 1000 Number of clusters = 9 Preference exponent = 10 Workers = 100 Walk length = 50 Embedding dimensions = 10</p>
Experiments on mouse pancreas (Section S7)	<p>Number of clusters = 13 Other parameters are the same as for human pancreas analysis (Section III F).</p>
Experiments on human brain (Section S6)	<p>Number of clusters = 7 Other parameters are the same as for human pancreas analysis (Section III F).</p>
Experiments on mouse brain (Section S7)	<p>Number of clusters = 9 Other parameters are the same as for human pancreas analysis (Section III F).</p>

TABLE S4: Hyperparameters Used in Each Experiment.